Journal of Energy Trends

ATATURK UNIVERSITY PUBLICATIONS

Atatürk Üniversitesi
1957
Atatürk University

Journal of Energy Trends

Journal of Energy Trends

REVIEWER BOARD

Journal of Energy Trends

AIMS AND SCOPE

The journal focuses on critical aspects of energy, including energy sources, flow dynamics, internal combustion engines, battery technology, production systems, and consumption patterns. By disseminating this vital knowledge, we aim to foster collaboration between researchers, educators, and policymakers. The Journal of Energy Trends serves as a valuable resource for researchers actively engaged in or seeking to explore the vast field of mechanical engineering.

Disclaimer

Statements or opinions expressed in the manuscripts published in the journal reflect the views of the author(s) and not the opinions of the editors, editorial board, and/or publisher; the editors, editorial board, and publisher disclaim any responsibility or liability for such materials. When using previously published content, including figures, tables, or any other material in both print and electronic formats, authors must obtain permission from the copyright holder. Legal, financial and criminal liabilities in this regard belong to the author(s).

Open Access Statement

Journal of Energy Trends is an open access publication. Starting on 2024, all content published in the journal is licensed under the Creative Commons Attribution-NonCommercial (CC BY-NC) 4.0 International License which allows third parties to use the content for non-commercial purposes as long as they give credit to the original work. This license allows for the content to be shared and adapted for non-commercial purposes, promoting the dissemination and use of the research published in the journal. All published content is available online, free of charge at https://dergipark.org.tr/en/pub/jet

Journal of Energy Trends

CONTENTS

Numerical Investigation of The Flow in Fractal Type Bifurcation and Trifurcation Systems with Different Features

Farklı Özelliklere Sahip Fraktal Tip Çatallanma ve Üçlükasyon Sistemlerinde Akışın Sayısal İncelenmesi

Ahmet KAHYA iD
İsak KOTCİOĞLU iD

Atatürk University, Faculty of Engineering, Mechanical Engineering Erzurum, Türkiye.

ABSTRACT

In this study, CFD and mathematical analyses were performed on straight pipe, double branched and triple branched pipe models. In the straight pipe model, it was observed that the velocity was maximum at the center and decreased towards the wall. While the velocity distribution was homogeneous at the inlet section, the velocity profile changed as the flow developed. In the double branched and triple branched pipe models, it was determined that the velocity decreased in the separation regions and vortex formations caused a decrease in velocity and an increase in pressure. The fact that the side branches were of the same diameter and in the same plane kept the differences in the velocity distribution to a minimum. The results showed that fractal flow systems with small aspect ratios provided less pressure loss.

Keywords: Trifurcation, bifurcation, flow analysis, pressure difference

ÖZ

Bu çalışmada, düz boru, çift çatallı ve üç çatallı boru modelleri üzerinde CFD ve matematiksel analizler gerçekleştirilmiştir. Düz boru modelinde, hızın merkezde maksimum olduğu ve cidara doğru azaldığı gözlemlenmiştir. Giriş kesitinde hız dağılımı homojenken, akış geliştikçe hız profili değişiklik göstermektedir. Çift çatallı ve üç dallı boru modellerinde ise ayrılma bölgelerinde hızın azaldığı, vorteks oluşumlarının hız düşüşüne ve basınç artışına neden olduğu belirlenmiştir. Yan dalların eş çapta ve aynı düzlemde olması, hız dağılımındaki farkları minimal tutmuştur. Sonuçlar, küçük en-boy oranına sahip fraktal akış sistemlerinin daha az basınç kaybı sağladığını göstermiştir.

Anahtar Kelimeler: Trifurkasyon, bifurkasyon, akış analizi, basınç farkı

Introduction

In various engineering applications, fractal-like geometric structures, new ideas, namely flow systems and approaches representing similar small-scale structures, have theoretically shaped the basic ideas of the research field in general over the past quarter century. This idea was inspired by living and non-living objects and is important for the future of applied engineering. In sequential and multi-flow systems with such similar structures, it is important to distribute the single-phase fluid evenly throughout the channel (Bejan, 1997). These channels can have symmetrical (regular) and asymmetrical (irregular) structures. As in circulatory systems, the branches or bifurcations in multi-flow systems can have narrowing and widening structures.

The mathematical behaviors and models of such physical mechanisms are similar to each other (Senn & Poulikakos, 2004). Fundamental laws such as Poiseuille and continuity equations in terms of fluid mechanics, Ohm's law for electrical circuits, Fourier equation in heat transfer calculations, Murray's law for bifurcation or fractal structures in biological systems are mathematically similar to each other.

In order to obtain the best heat transfer performance of fractal-like channel networks, optimization of many geometric factors is required. Examples of these geometric factors are; number of levels (L), number of branches-number of bifurcations (n), bifurcation angle (θ), length scale ratio (γ), width scale ratio (β), and terminal (end boundary) channel width (w_m). To find the optimum point by establishing a relationship between these factors and to ensure that the system to be created is more efficient (Alharbi et al. 2003).

1. Theoretical Foundations

Bifurcation or branching is a phenomenon frequently seen in multi-flow systems. At these points, we can encounter expanding or contracting structures, they can be symmetrical or asymmetrical. Comparison of such structures with Newtonian and non-Newtonian fluids with different flow conditions is of great importance for various application areas. For example, they can be seen in many physical mechanisms, from biological systems such as blood vessels or lung airways to city water networks. They are also important in many areas, from cooling systems of electronic circuits to the development of new generation heat exchangers. Analogies of such systems can lead to important advances in different areas (Kotcioğlu, 2017).

1.1. Constructal Theory
Constructal theory is an approach that explains how complex structures consisting of many interconnected simple elements are formed in nature. This theory suggests that systems in nature adapt to perform their functions with the least energy expenditure. Using reverse engineering methods, the properties of these optimized structures in nature are examined and practical applications of this information are developed. Constructal theory can be observed in many areas from biological organisms to streams, from heat transfer to electric current. This theory helps us understand the complexity of nature and find more efficient and sustainable solutions in technology (Wang et al. 2010a).

2. Fractal, Bifurcation and Branch Geometry

2.1. Fractal (leaf) Structure
They are geometric shapes that are mathematically defined and have self-similarity. These shapes repeat the same structure at any scale. They have repeating building blocks that form a certain pattern, and these building blocks create a smaller copy of the same pattern at each scale. Fractals are used in modeling complex structures frequently observed in nature. Structures such as leaves, butterfly wings, circulatory systems, tree branches are examples of these structures (Colak et al. 2018).

2.2. Bifurcation Structure
Another structure similar to fractal structures is bifurcation (double branch) structures. Bifurcation is the occurrence of two or more different states or behaviors in a system after a certain point. Generally, in mathematical and physical systems, the values of variables change suddenly after a certain critical point, leading to new and different behaviors (Blonski et al. 2020). They can be designed according to applications in various engineering fields in a regular structure and in the form of elastic veins. These designed structures are models that have become increasingly important in terms of engineering applications. Symmetrical and asymmetrical structures are shown in Figure 1.
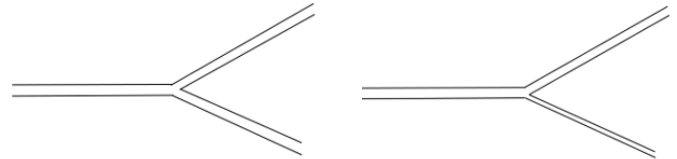
Figure 1.
Symmetrical (bifurcation), Non-symmetrical (bifurcation) structures

2.3. Branch Structure
A complex structure similar to fractal structures; these structures are models that contain fractal and bifurcation structures together (Muwanga et al. 2008). They are structures that include structures such as leaf, butterfly wing, dill, etc. as well as vein, network systems, tree branches, etc. Different branch structures are shown in Figure 2. They are also created in a certain hierarchical order.

3. Mathematical Model

The Navier-Stokes equations for a cylindrical pipe (vessel) are given below. The flow velocity vector is defined as vectorial ($\vec{U}$) by the following 1 equation.

$$\vec{U} = u(ue_r + ve_\phi + we_z) \tag{1}$$
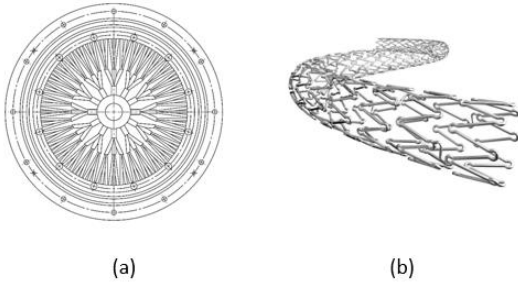
Figure 2.
 a) Disc-shaped flow tube, b) Vascular stent (Çolak, 2017)

From the equation, for one-dimensional axial flow in cylindrical pipes, $u = u(r)$ is a function of u. The other fluid velocities in both directions are $v = w = o$ and $\to \partial/\partial z = 0$. Here, the continuity equation for three-dimensional and one-dimensional flow in cylindrical coordinates is given by the following equation in vectorial and differential form (Equation 2).

$$\vec{\nabla}.\vec{V} = \frac{1}{r}\left[r\frac{\partial u}{\partial r} + r\frac{\partial v}{\partial \phi} + \frac{\partial w}{\partial z}\right] \quad (2)$$

The same equation is given below for one-dimensional ($v = w = o$) flow (Equation 3).

$$\vec{\nabla}.\vec{V} = \frac{1}{r}\left[r\frac{\partial u}{\partial r}\right] = 0 \to u \neq f_n(x) \to u = u(r) \quad (3)$$

The momentum equation is expressed in vector form in the following equation (Equation 4).

$$\rho\left[\frac{\partial\vec{V}}{\partial t} + \vec{U}.\vec{\nabla}\vec{U}\right] = -\vec{\nabla}P + \rho\vec{g} + \mu\vec{\nabla}^2\vec{U} = \frac{1}{r}(r\frac{\partial^2 u}{\partial r^2})\,\vec{e}_r \quad (4)$$

In this equation, $\vec{\nabla}P$ is the pressure gradient. In equation (5), the dimensionless number Reynolds number, which determines the flow regime of the fluid passing through the channel, is given by the following equation.

$$Re = \frac{\rho.D_h.U}{\mu} \quad (5)$$

In this equation, D_h is the hydraulic diameter, ρ is the density, U is the velocity, μ is the dynamic viscosity. The wall shear stress in a straight cylindrical pipe (vessel) in steady laminar flow is defined by the following equation (Equation 6).

$$\tau_\omega = \frac{32\mu\dot{Q}}{\pi r^3} \quad (6)$$

$\dot{Q}$ given in the equation is the volumetric flow rate. The equation of the velocity distribution in a cylindrical pipe in steady flow is defined by the following 7 equation.

$$u = U_{max}\left(1 - \frac{r^2}{R^2}\right) \quad (7)$$

The velocity distribution in pulsatile flow is expressed by the following 8 equation.

$$u = U_{max}(1 + sin(2\pi.t)) \quad (8)$$

According to Poiseuille's law, the volumetric flow rate of a fluid passing through a cylindrical pipe in steady flow is given by the following 9 equation.

$$\dot{Q} = \Delta P.\pi.\frac{r_i^4}{8\mu} \quad (9)$$

In this equation, ΔP is the pressure difference between the inlet and outlet. The wall shear stress is defined according to the volumetric flow rate and pressure difference as given below, respectively (Equation 10).

$$\tau = \frac{4\mu\dot{Q}}{\pi r_i^3} \quad (10)$$

3.1 Murray's Law
Murray's law is a principle proposed to optimize efficiency by minimizing the required blood (fluid) flow and energy in a vessel (branch-pipe) (Lee, J. Y. & Lee, S. J. 2010). In its simplest form, the equation for a parent vessel with a radius r_0 and two daughter branches with radii r_1 and r_2 is given by the Equation (11).

$$r_0^\lambda = r_1^\lambda + r_2^\lambda \quad (11)$$

In this equation, r0 is the radius of the main branch, while r1 and r2 are the radii of the side branches. λ represents the branching exponent. According to Murray's law, when λ=3 it indicates that the flow energy is minimized. For this reason, λ=3 is typically used in the formula. Accordingly, Equation (12) becomes:

$$r_0^3 = r_1^3 + r_2^3 \quad (12)$$

is arranged as follows.

4.Fluid (Water) Properties

The properties of the fluid used in the analysis are given in Table 1.

Table 1.
 Density and viscosity of fluids

Newtonian	μ (kgm^{-1}s^{-1})	P (kgm^{-3})
Newtonian (Water)	0.008	997

5. RESULTS AND DISCUSSION

In this study, various solid models, including straight pipe (Figure 3), bifurcation pipe (Figure 10), and trifurcation pipe (Figure 17), were designed using the SolidWorks software in accordance with the specifications provided in the tables (2-4). Velocity and pressure analyses were then performed on these models using ANSYS software. Subsequently, the analysis results were supported and evaluated using MATLAB (Figure 24-25) software.

5.1. Straight Pipe Ansys Analysis
The properties of straight pipes analyzed with Ansys were drawn with the SolidWorks program according to the data in Table 2.

Table 2.
Characteristics of the pipe

Pipe	Diameter(mm)	Length(mm)
1	6	70
2	8	80
3	10	90
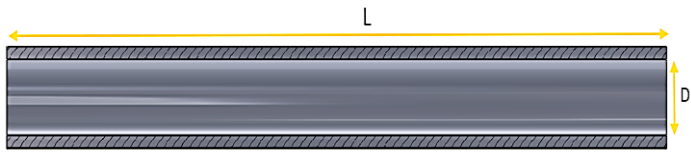
Figure 3.
Straight pipe cross-sectional area
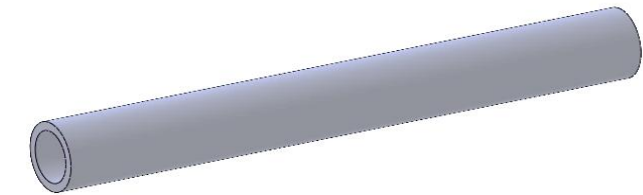
Figure 4.
Straight pipe (D=6mm, L=70mm)
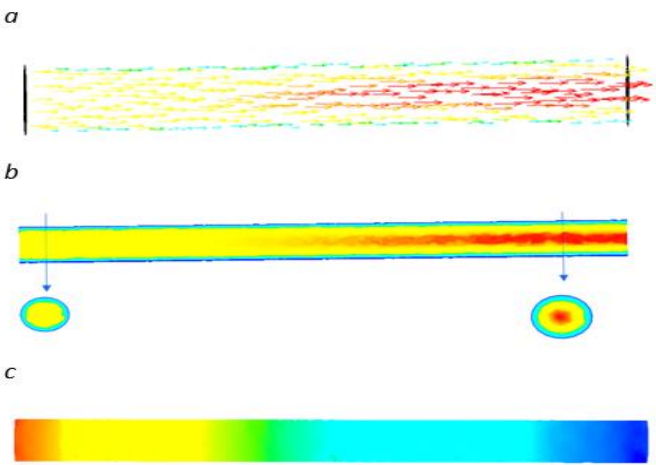
Figure 5.
a) Ansys vector velocity analysis for straight pipe (D=6mm, L=70mm), b) Ansys velocity analysis for straight pipe, c) Ansys pressure analysis for straight pipe (D=6mm, L=70mm)
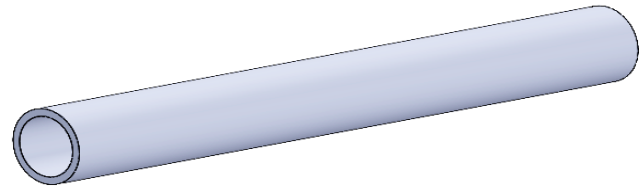
Figure 6.
Straight pipe (D=8mm, L=80mm)
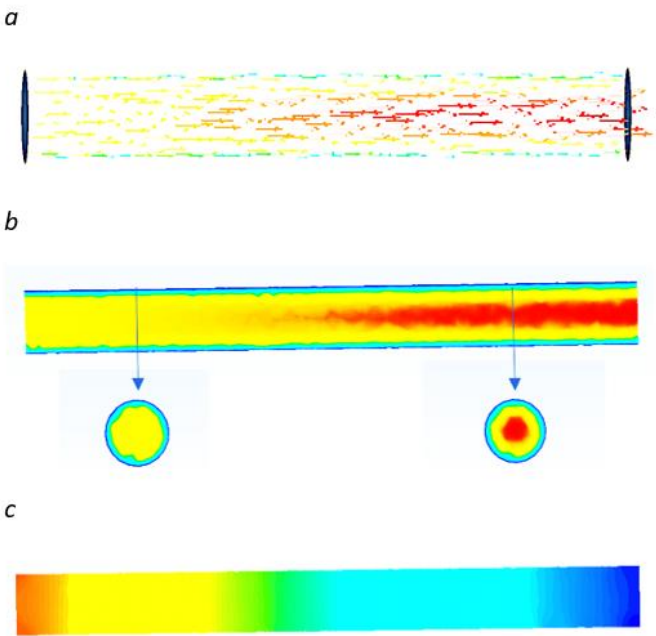
Figure 7.
a) Ansys vector velocity analysis for straight pipe (D=8mm, L=80mm), b) Ansys velocity analysis for straight pipe (D=8mm, L=80mm), c) Ansys pressure analysis for straight pipe (D=8mm, L=80mm)
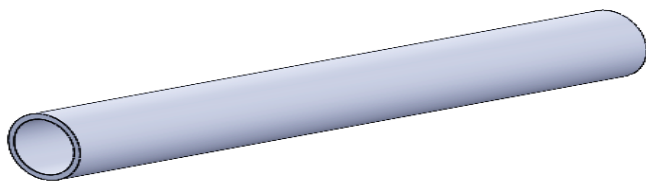
Figure 8.
Straight pipe (D=10mm, L=90mm)
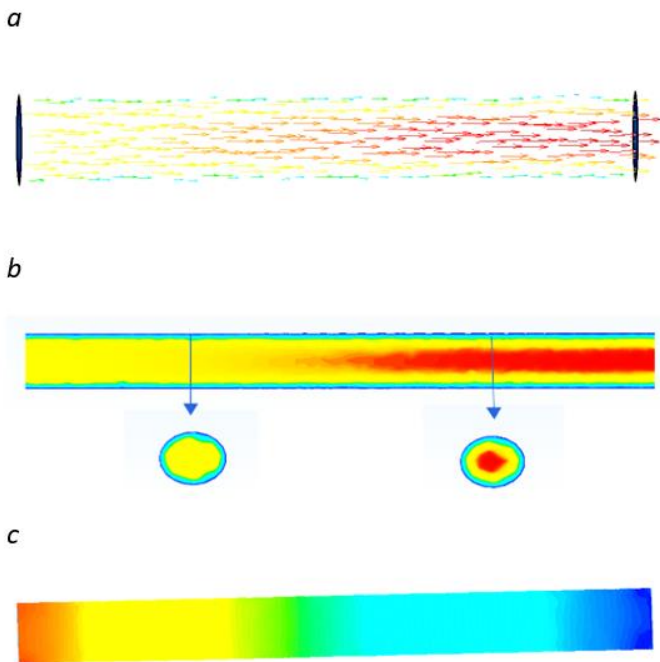
Figure 9.
a) Ansys vector velocity analysis for straight pipe (D=10mm, L=90mm), b) Ansys velocity analysis for straight pipe (D=10mm, L=90mm), c) Ansys pressure analysis for straight pipe (D=10mm, L=90mm)

The flow of water at a velocity of 0.3 m/s through a straight pipe with a diameter of 6 mm and a length of 70 mm was analyzed using ANSYS. The physical dimensions of the pipe are shown in Figure 4. According to the velocity analysis results, the velocity distribution of the water inside the pipe is represented by a color scale. As shown in Figure 5-a with vector lines and Figure 5-b, the highest velocity was observed at the center of the pipe, while it decreased toward the edges. This indicates a velocity profile consistent with laminar flow characteristics. In the vector velocity analysis, local velocity variations along the pipe were observed, where higher velocity regions are represented by red and yellow colors, while lower velocity regions are represented by blue colors. The pressure analysis revealed a pressure drop from the inlet to the outlet of the pipe. As illustrated in Figure 5-c, the color scale indicates a transition from high pressure to low pressure, which is a result of frictional losses along the pipe during the flow. The flow of water at a velocity of 0.3 m/s through a straight pipe with a diameter of 8 mm and a length of

80 mm was also analyzed. The physical dimensions of this pipe are shown in Figure 6. According to the velocity analysis results, the velocity distribution of the water inside the pipe is represented by a color scale. As shown in Figures 7-a and Figure 7-b, the highest velocity was observed at the center of the pipe, while it decreased toward the edges. This is consistent with the characteristics of laminar flow. In the vector velocity analysis, local velocity variations along the pipe were observed, where higher velocity regions are represented by red and yellow colors, while lower velocity regions are represented by blue colors. The pressure analysis revealed a pressure drop from the inlet to the outlet of the pipe. As illustrated in Figure 7-c, the color scale indicates a transition from high pressure to low pressure, which is a result of frictional losses along the pipe during the flow. The flow of water at a velocity of 0.3 m/s through a straight pipe with a diameter of 10 mm and a length of 90 mm was also analyzed. The physical structure of the pipe is visually presented in Figure 8. According to the flow analysis, the velocity distribution of the water inside the pipe is notably higher at the center and lower toward the edges. As shown in Figure 9-a, the vector velocity analysis details the velocity variations along the pipe, with high-velocity regions represented by red and yellow tones at the center and low-velocity regions represented by blue tones toward the edges. This demonstrates the laminar nature of the flow. The velocity analysis results presented in Figure 9-b provide a broader perspective on the overall velocity profile of the water inside the pipe. It was observed that the water moves faster at the center of the pipe, while the velocity decreases at the edges due to friction. Pressure analysis results showed a pressure drop from the inlet to the outlet of the pipe. As depicted in Figure 9-c, the color scale clearly shows a transition from high pressure (red) to low pressure (blue). This pressure drop is evaluated as a natural result of frictional effects along the pipe. In the comparison of the pipes in terms of their diameters and lengths, it was observed that as the diameter increased, the velocity profile became more homogeneous, and pressure loss decreased. In the pipe with a 6 mm diameter, due to the narrow cross-section, the velocity was concentrated at the center and decreased significantly towards the edges. This pipe experienced the highest-pressure loss. In the pipe with an 8 mm diameter, the velocity profile was more balanced, with a smoother transition in velocity reduction at the edges. In the pipe with a 10 mm diameter, the velocity distribution was the most homogeneous, with a very slight decrease in velocity from the center towards the edges. Moreover, this pipe exhibited the lowest pressure loss among the three. In terms of length, as the pipe length increased, frictional pressure losses also increased. In the 70 mm long pipe, the pressure loss was limited due to the short distance; however, the narrow diameter made friction losses more pronounced. In the 80 mm long pipe, frictional

effects became more apparent, but the velocity distribution remained relatively balanced. In the 90 mm long pipe, the highest frictional losses occurred; however, the wider diameter mitigated the impact of these losses on the flow, resulting in a more balanced velocity profile.

Overall, pipes with larger diameters and shorter lengths offered lower pressure losses and more homogeneous velocity profiles, providing more efficient flow characteristics. As the diameter increased, the velocity distribution became more uniform, while increased length led to higher frictional losses. Considering these two factors together is essential for optimizing flow performance.

5.2. Ansys Analysis for Bifurcation Pipe

The properties of bifurcation pipes analyzed with Ansys were drawn with the SolidWorks program according to the data in Table 3.

Table 3.

Characteristics of the pipe

Pipe	1.Diameter (mm)	2.Diameter (mm)	Main Pipe length (mm)	Side Pipe length (mm)	Angle
1	6	4	70	50	50
2	8	6	80	60	60
3	10	8	90	70	70
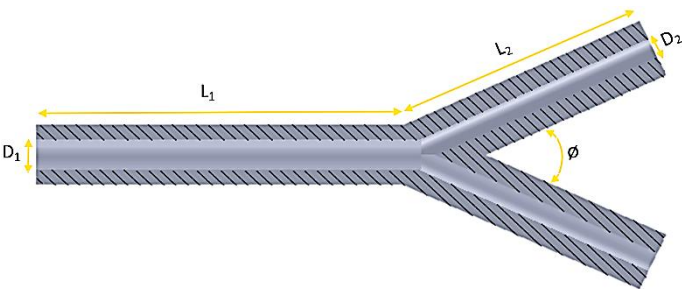
Figure 10.
Bifurcation pipe cross-sectional area
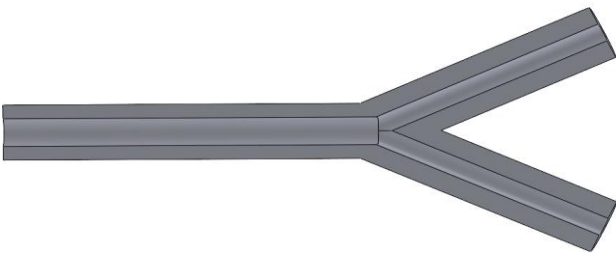
Figure 11.
Bifurcation pipe (D_1=6mm, D_2=4mm, L_1=70mm, L_2=50, Ø=50°)
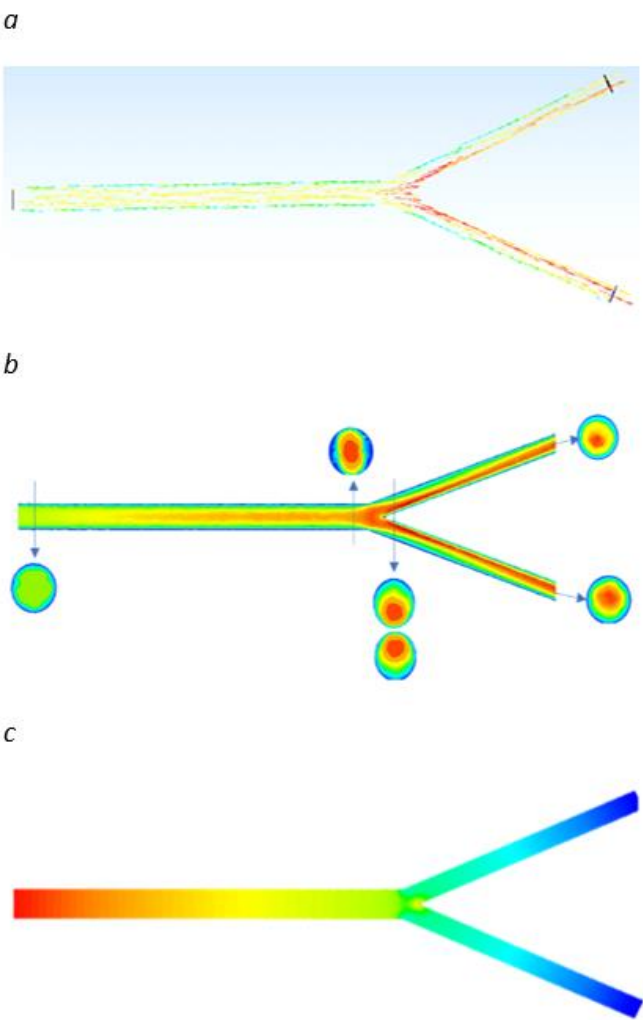
Figure 12.
a) Ansys vector velocity analysis for bifurcation pipe, b) Ansys velocity analysis for bifurcation pipe (D_1=6mm, D_2=4mm, L_1=70mm, L_2=50, ø=50°), c) Ansys pressure analysis for bifurcation pipe (D_1=6mm, D_2=4mm, L_1=70mm, L_2=50, ø=50°)
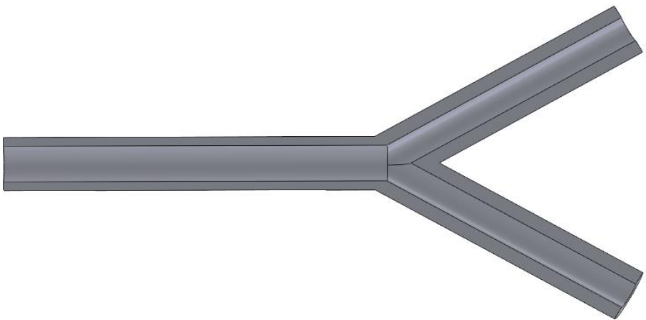
Figure 13.
Bifurcation pipe (D_1=8mm, D_2=6mm, L_1=80mm, L_2=60, Ø=60°)

a

b

c
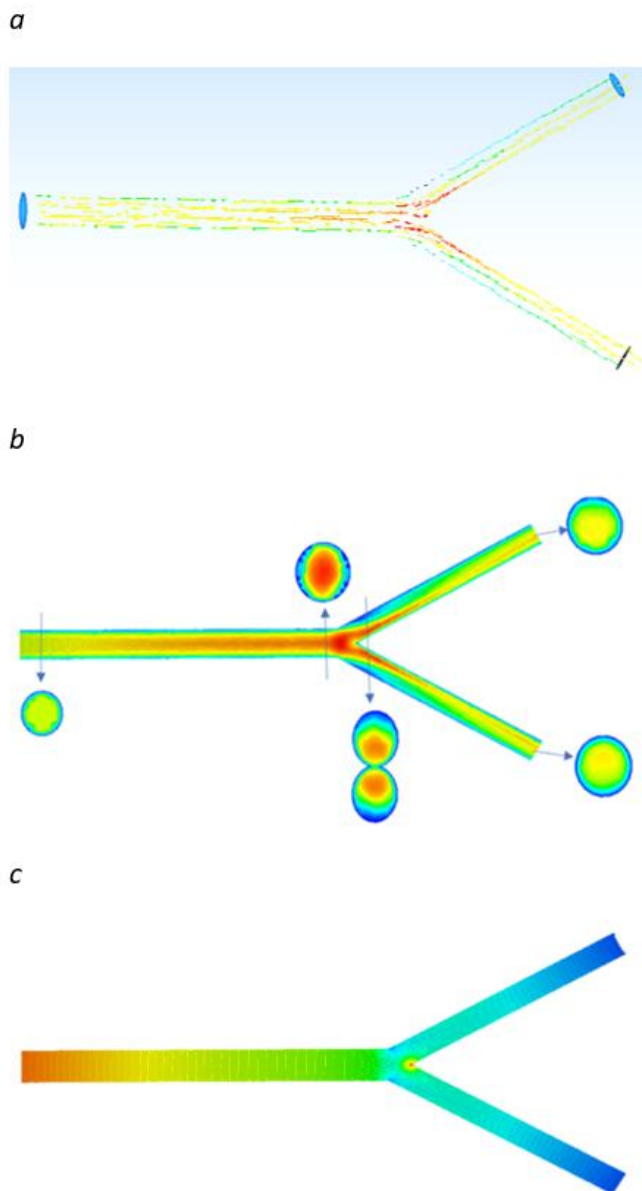
Figure 14.
a) Ansys vector velocity analysis for bifurcation pipe, b) Ansys velocity analysis for bifurcation pipe (D1=8mm, D2=6mm, L1=80mm, L2=60, ø=60°), c) Ansys pressure analysis for bifurcation pipe (D1=8mm, D2=6mm, L1=80mm, L2=60, ø=60°)
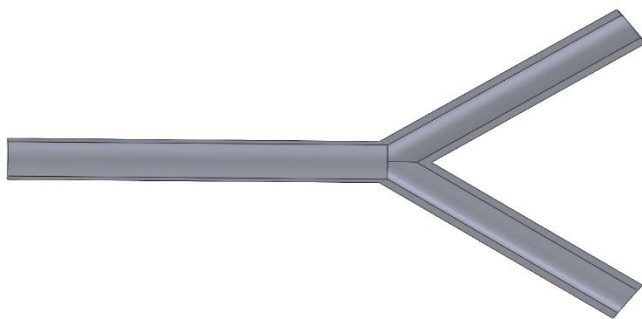
Figure 15.
Bifurcation pipe (D1=10mm, D2=8mm, L1=90mm, L2=70, ø=70°)

a

b

c
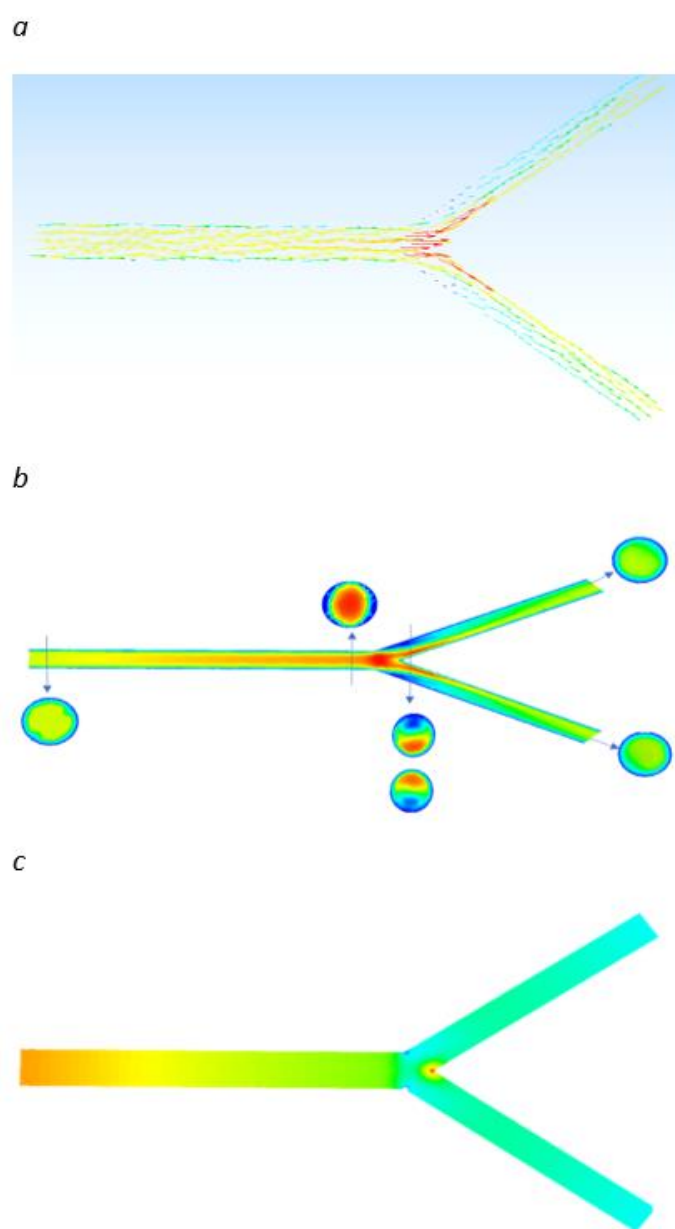
Figure 16.
a) Ansys vector velocity analysis for bifurcation pipe, b) Ansys velocity analysis for bifurcation pipe, c) Ansys pressure analysis for bifurcation pipe

The flow of water at a velocity of 0.3 m/s through a pipe with an inlet diameter of D_1=6 mm, outlet diameters of D_2=4 mm, inlet length of L_1=70 mm, outlet lengths of L_2=50 mm, and bifurcation angle of ø=50° was analyzed using Ansys. The physical dimensions of the pipe are shown in Figure 11. The velocity analysis results Figures 12-a and Figure 12-b illustrate the velocity distribution of the water inside the pipe using a color scale. A significant decrease in velocity was observed at the bifurcation point due to the directional change in the flow and the angular structure of the pipe. The velocity profile indicates that the highest velocities occur in the inlet region and decrease along the branches. Additionally, the 50° angle increased the

turbulence level during flow direction change and caused local velocity differences around the bifurcation point. These differences are represented by red and yellow colors for high-velocity regions and blue colors for low-velocity regions. The vectorial analysis in Figure 12-a shows the directional components of the flow. According to the analysis results, the 50° angle intensified the flow direction change at the bifurcation point and increased the turbulence in this region. Due to the turbulence, the flow did not distribute uniformly along the branches, and higher velocities were observed in some areas. The pressure analysis is shown in Figure 12-c. The results indicate a pressure drop from the inlet to the outlets of the pipe. This pressure drop is depicted using a color scale transitioning from red to blue, reflecting the flow direction change and friction losses caused by the 50° angle. The magnitude of the angle led to fluctuations in both velocity and pressure, resulting in an uneven pressure distribution at the outlets. The geometric properties of another bifurcation pipe are shown in Figure 13, where the pipe has an inlet diameter of $D_1=8$ mm, outlet diameter of $D_2=6$ mm, inlet length of $L_1=80$ mm, outlet lengths of $L_2=60$ mm, and bifurcation angle of $\phi=60°$. This design allows for a directional flow change and provides the means to analyze velocity and pressure profiles. The vectorial velocity distribution of the flow, illustrated in Figure 14-a, demonstrates the directional and magnitude components of the water velocity inside the pipe using colored vectors. Higher velocities were observed in the inlet region, while reductions in velocity occurred at the bifurcation point due to the directional change. Additionally, the bifurcation angle increased turbulence, causing the flow to distribute unevenly along the branches. The velocity distribution within the pipe, represented by a color scale in Figure 14-b, highlights high-velocity regions in red and yellow tones, while blue and green tones indicate low-velocity regions. The analysis shows that maximum velocity occurs in the inlet region, and a significant decrease is evident at the bifurcation point. The 60° bifurcation angle intensified local velocity differences and turbulence, with a gradual decrease in velocity along the branches. The pressure distribution of the pipe is depicted in Figure 14-c using a color scale transitioning from red to blue. The results reveal high pressure in the inlet region, with a notable decrease at the bifurcation point and along the branches. This outcome is attributed to friction losses and the directional change of the flow. The 60° angle caused pressure fluctuations and resulted in an uneven pressure distribution at the outlets. The geometric properties of a third bifurcation pipe are shown in Figure 15. The pipe has an inlet diameter of $D_1=10$ mm, outlet diameter of $D_2=8$ mm, inlet length of $L_1=90$ mm, outlet lengths of $L_2=70$ mm, and a bifurcation angle of $\phi=70°$. This design facilitates flow direction changes and provides a detailed investigation of velocity and pressure profiles. The

vectorial velocity analysis presented in Figure 16-a shows the directional and magnitude components of the water velocity using colored vectors. High velocities were observed in the inlet region, while reductions in velocity occurred at the bifurcation point due to directional changes. Additionally, the 70° bifurcation angle increased turbulence, leading to uneven flow distribution along the branches. Local velocity differences were also observed due to the turbulence. The velocity distribution represented in Figure 16-b uses a color scale to highlight high-velocity regions in red and yellow tones, while blue and green tones indicate low-velocity regions. The analysis confirms maximum velocity at the inlet, with a significant reduction in velocity at the bifurcation point. The 70° bifurcation angle contributed to turbulence-induced irregularities in the velocity profile, with a gradual reduction in velocity along the branches. The pressure distribution of the pipe is illustrated in Figure 16-c, where a transition from red to blue indicates a pressure drop from the inlet to the outlets. High pressure is evident in the inlet region, with a decrease at the bifurcation point and along the branches. The 70° angle caused fluctuations in pressure due to the flow direction change and friction losses, resulting in an uneven pressure profile at the outlets.

5.3. Ansys Analysis for Trifurcation Pipe

The properties of trifurcation pipes analyzed with Ansys were drawn with the SolidWorks program according to the data in Table 4.

Table 4.
Characteristics of the pipe

Pipe	1.Diameter (mm)	2.Diameter (mm)	Main Pipe length (mm)	Side Pipe length (mm)	Angle
1	6	4	70	50	50
2	8	6	80	60	60
3	10	8	90	70	70
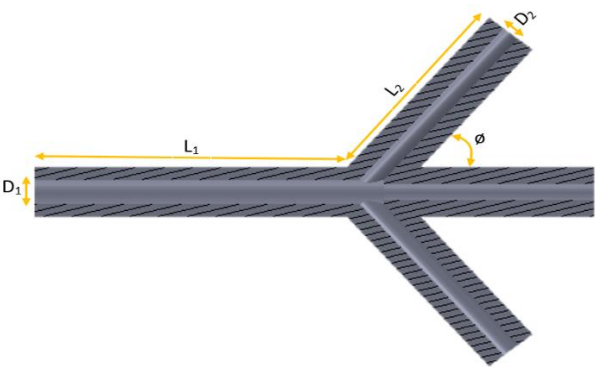
Figure 17.
Trifurcation pipe cross-sectional area

a
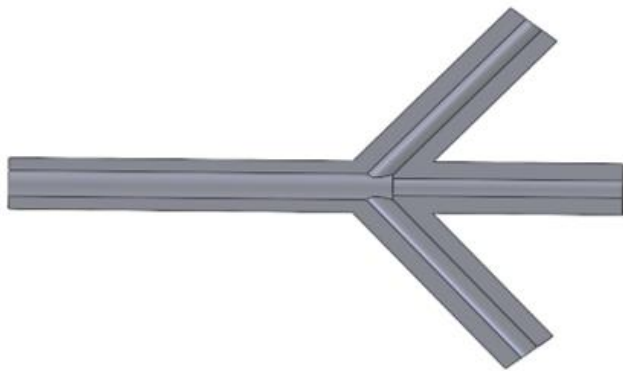
b
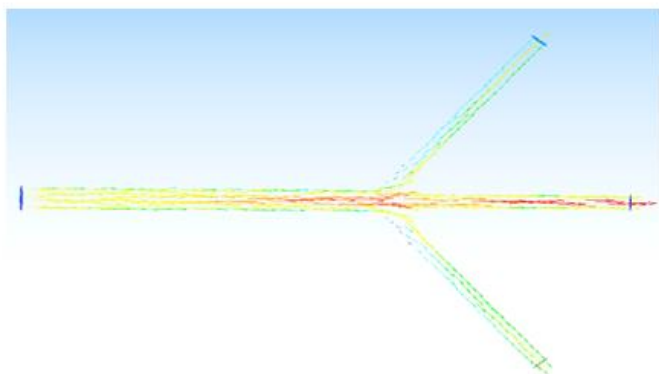
Figure 18.
a) Trifurcation pipe (D1=6mm, D2=4mm, L1=70mm, L2=50, ø=50°), b) Ansys vector velocity analysis for trifurcation pipe

a
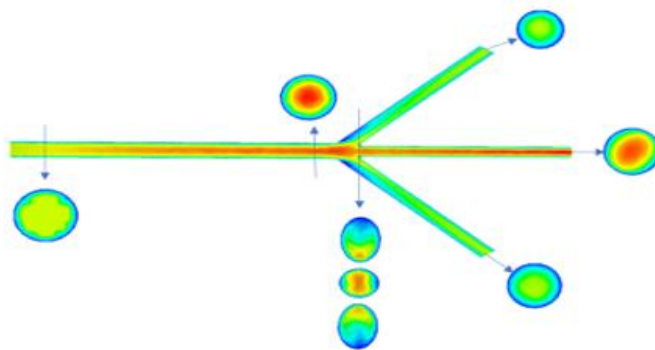
b
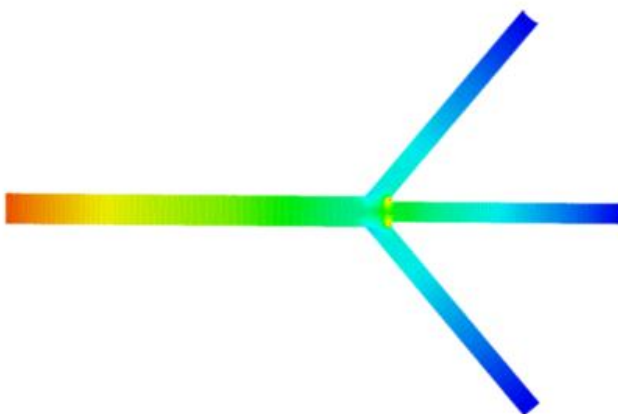
Figure 19.
a) Ansys velocity analysis for trifurcation pipe, b) Ansys pressure analysis for trfurcation pipe
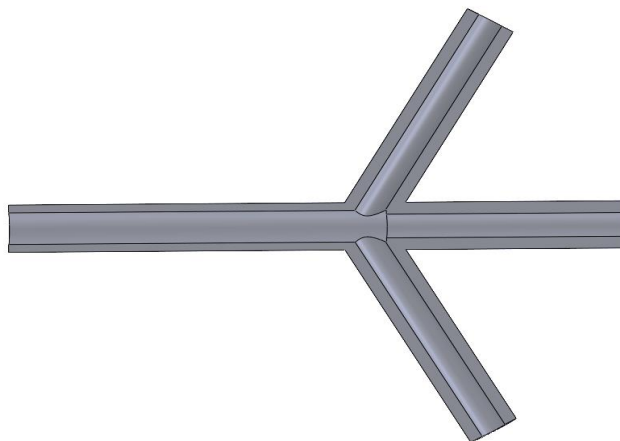
Figure 20.
Trifurcation pipe (D1=8mm, D2=6mm, L1=80mm, L2=60, ø=60°)

a

b

c
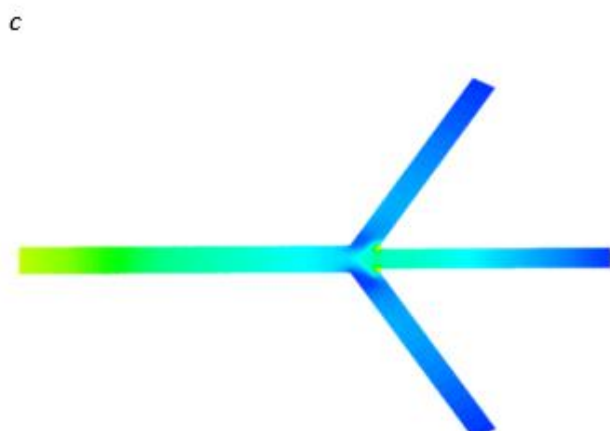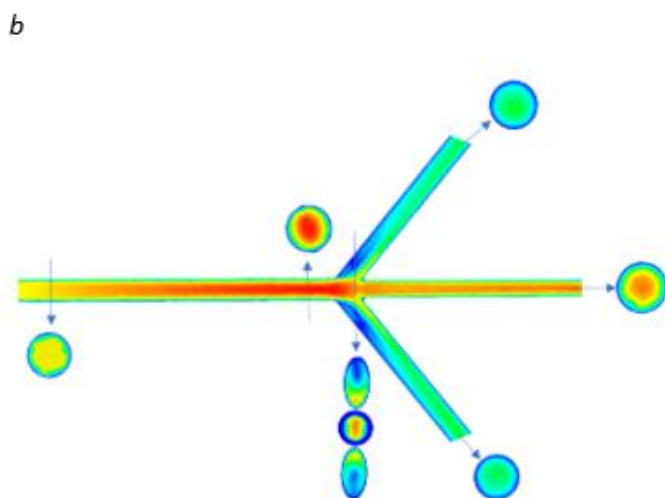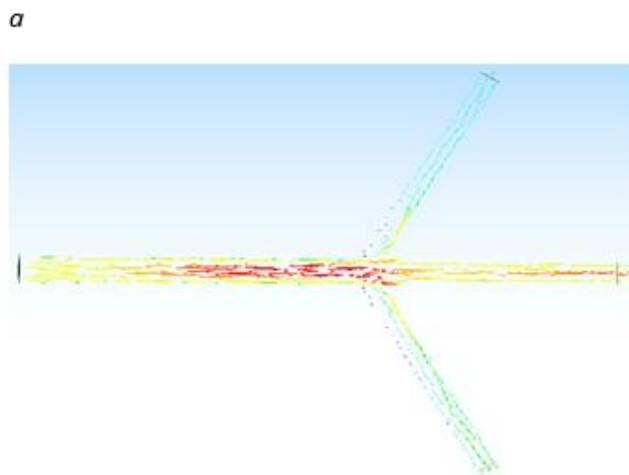
Figure 21.
a) Ansys vector velocity analysis for trifurcation pipe, b) Ansys velocity analysis for trifurcation pipe, c) Ansys pressure analysis for trifurcation pipe
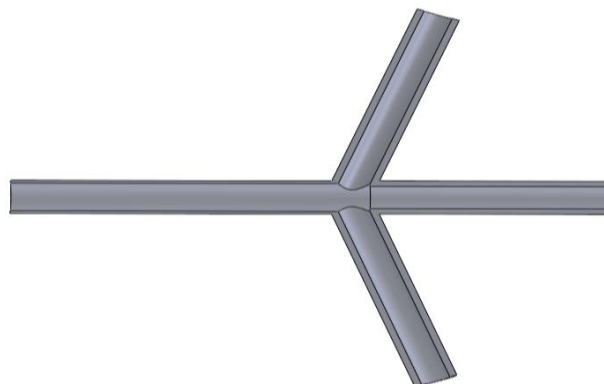
Figure 22.
Trifurcation pipe (D_1=10mm, D_2=8mm, L_1=90mm, L_2=70, $\emptyset$=70°)

a

b

c
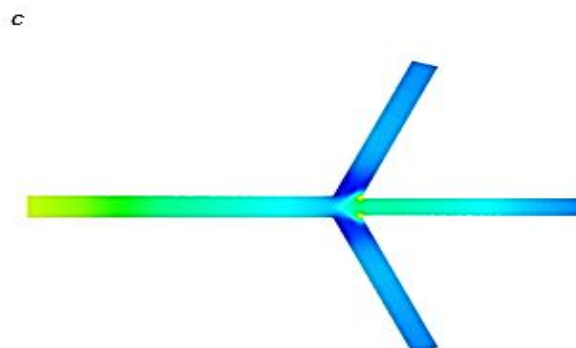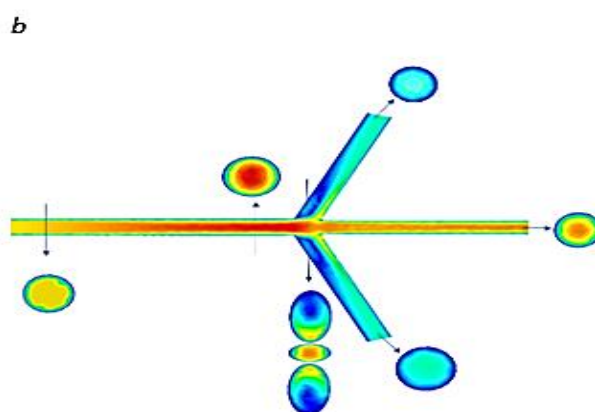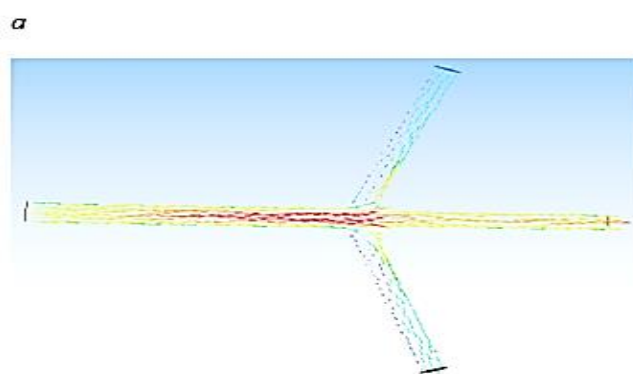
Figure 23.
a) Ansys vector velocity analysis for trifurcation pipe, b) Ansys velocity analysis for trifurcation pipe, c) Ansys pressure analysis for trifurcation pipe

The design and analysis results of the trifurcation pipe have been explained in detail. Figure 17 and Figure 18-a illustrates the geometric properties of the trifurcation pipe. According to this design, the inlet diameter is D_1=6 mm the outlet diameter is D_2=4 mm, the inlet pipe length is L_1=70 mm, the outlet pipe length is L_2=50 mm, and the angle between the pipes is $\emptyset$=50°.These dimensions are fundamental parameters used in fluid dynamics analyses. The velocity vectors within the trifurcation pipe were analyzed using ANSYS software, as shown in Figure 18-b. The distribution of velocity vectors demonstrates how the fluid is directed from the inlet towards the branches. This analysis was conducted to examine the impact of the trifurcation pipe design on flow performance. The direction and intensity of the vectors clearly reveal the effect of the pipe geometry on the flow. The results of the velocity analysis are detailed in Figure 19-a. The color scale represents the velocity values of the fluid. According to the analysis, the velocity is higher at the inlet of the pipe and changes as it progresses towards the branches. This velocity distribution indicates that the fluid is effectively divided into the branches in accordance with the pipe design, confirming the design's ability to guide the fluid. The pressure analysis is presented in Figure 19-b. In this analysis, high-pressure values were observed at the inlet of the trifurcation pipe, while the pressure gradually decreased across the branches. The color distribution clearly demonstrates the pressure drop from the inlet to the outlets. This phenomenon highlights the energy loss and redistribution effect occurring during the division of the fluid into the branches. Figure 20 illustrates the geometric properties of the trifurcation pipe. In this design, the inlet diameter is D_1=8 mm, the outlet diameter is D_2=6 mm, the inlet pipe length is L_1=80 mm, and the outlet pipe length is L_2=60 mm. The angle between the branches is $\emptyset$=60°. These geometric parameters serve as the basis for fluid dynamics analyses conducted in subsequent steps. The velocity vectors inside the trifurcation pipe are analyzed and visualized in Figure 21-a using ANSYS software. The vector plot demonstrates the flow distribution and directional behavior of the fluid as it enters the pipe and branches out. The vectors highlight the influence of the pipe's geometry on the flow, showing how the fluid transitions and adjusts within the bifurcated structure. Figure 21-b presents the results of the velocity distribution analysis. The color scale in the figure represents the fluid velocity, with higher values concentrated at the inlet and a gradual reduction as the flow progresses into the branches. This velocity distribution indicates the efficiency of the pipe design in directing and distributing the fluid evenly across its outlets. The pressure distribution analysis is shown in Figure 21-c. The results reveal high-pressure regions at the pipe's inlet, with a consistent pressure drop as the fluid moves through the pipe and into the branches. The color scale in the

figure clearly visualizes this gradient, emphasizing the energy dissipation and redistribution effects occurring during the flow division process. Figure 22 illustrates the geometric properties of the trifurcation pipe. In this design, the inlet diameter is D_1=10 mm, the outlet diameter is D_2=3 mm, the inlet pipe length is L_1=90 mm and the outlet pipe length are L_2=70 mm. The angle between the pipes is $\emptyset$=70°.These measurements form the basis for the fluid dynamics analysis conducted on the pipe. Figure 23-a shows the velocity vectors within the trifurcation pipe, analyzed using ANSYS software. The velocity vectors visualize how the fluid is directed from the inlet toward the branches. The density and direction of the vectors highlight the flow distribution and behavior within the pipe based on its design. This analysis aims to evaluate the pipe's effectiveness in directing fluid flow. The velocity distribution analysis results are presented in Figure 23-b. The color scale represents the velocity values within the pipe. According to the analysis, the velocity is higher at the inlet and decreases significantly as the fluid progresses toward the branches. This indicates that the fluid is effectively divided among the branches in line with the pipe's geometry, demonstrating the design's efficiency in controlling flow. Figure 23-c presents the pressure analysis results. The analysis shows high pressure at the inlet, with a gradual decrease across the branches. The color scale clearly illustrates the pressure loss and redistribution as the fluid divides into the branches.

6. Solutions with the help of Matlab

```
% Kullanıcıdan Girdi Alma
D = input('Boru çapını girin (m): ');          % Boru çapı (m)
L = input('Boru uzunluğunu girin (m): ');      % Boru uzunluğu (m)
u_avg = input('Ortalama hızı girin (m/s): ');  % Ortalama hız (m/s)
rho = input('Su yoğunluğunu girin (kg/m^3): '); % Su yoğunluğu (kg/m^3)
mu = input('Su dinamik viskozitesini girin (Pa·s): ');% Su viskozitesi

% Hesaplamalar
R = D / 2;                  % Borunun yarıçapı (m)

% 1. Reynolds Sayısı Hesabı
Re = (rho * u_avg * D) / mu;
fprintf('\nReynolds Sayısı: %.2f\n', Re);

% 2. Darcy-Weisbach Basınç Düşüşü
if Re < 2300
    f = 64 / Re;           % Laminer akış için sürtünme katsayısı
else
    f = 0.079 * Re^(-0.25); % Türbülanslı akış için sürtünme katsayısı
end
Delta_p = f * (L / D) * (rho * u_avg^2 / 2);
fprintf('Basınç Kaybı: %.2f Pa\n', Delta_p);

% 3. Hız Profili
u_max = 2 * u_avg;         % Maksimum hız (m/s)
r = linspace(0, R, 100);   % Boru çapı boyunca noktalar (m)
u_r = u_max * (1 - (r.^2 / R^2)); % Hız profili

% 4. Basınç Dağılımı
x = linspace(0, L, 100);      % Boru uzunluğu boyunca noktalar (m)
p0 = input('Giriş basıncını girin (Pa): '); % Giriş basıncı (Pa)
p_x = p0 - Delta_p * (x / L);  % Basınç dağılımı

% Sonuçların Yazdırılması
fprintf('Maksimum Hız: %.2f m/s\n', u_max);
fprintf('Sürtünme Katsayısı: %.4f\n', f);
fprintf('Çıkış Basıncı: %.2f Pa\n', p_x(end));
```

Figure 24.
Matlab codes for straight pipe

```matlab
% Kullanıcıdan Girdi Alma
D_in = input('Giriş borusu çapı (m): ');
D_out = input('Çıkış borusu çapı (m): ');
L_in = input('Giriş borusu uzunluğu (m): ');
L_out = input('Çıkış borusu uzunluğu (m): ');
theta = input('Çıkış açısı (derece): ');
u_in = input('Giriş hızını girin (m/s): ');
rho = input('Su yoğunluğunu girin (kg/m^3): ');
mu = input('Su dinamik viskozitesini girin (Pa·s): ');

% Boru Kesit Alanları
A_in = pi * (D_in / 2)^2;
A_out = pi * (D_out / 2)^2;

% 1. Reynolds Sayısı Hesabı
Re_in = (rho * u_in * D_in) / mu;
fprintf('Reynolds Sayısı (giriş): %.2f\n', Re_in);

% 2. Hız Dağılımı ve Çıkış Hızı Hesabı
u_out = u_in * (A_in / (2 * A_out));
fprintf('Çıkış Hızı: %.2f m/s\n', u_out);

% 3. Basınç Kaybı (Darcy-Weisbach)
if Re_in < 2300
    f_in = 64 / Re_in;
else
    f_in = 0.079 * Re_in^(-0.25);
end
Delta_p_in = f_in * (L_in / D_in) * (rho * u_in^2 / 2);
Delta_p_out = f_in * (L_out / D_out) * (rho * u_out^2 / 2);

fprintf('Giriş Borusu Basınç Kaybı: %.2f Pa\n', Delta_p_in);
fprintf('Çıkış Borusu Basınç Kaybı: %.2f Pa\n', Delta_p_out);

% Basınç Dağılımı
p0 = input('Giriş basıncını girin (Pa): ');
p_out = p0 - (Delta_p_in + Delta_p_out);
fprintf('Çıkış Basıncı: %.2f Pa\n', p_out);
```

Figure 25.
Matlab codes for bifurcation and trifurcation pipe

Conclusion

Straight pipes: As diameter increases (D=6,8,10 mm), velocity becomes more uniform, and turbulence decreases. Smaller diameters cause higher pressure drops due to friction, while larger diameters reduce resistance. Longer pipes (L=70,90 mm) slightly increase pressure drop, but larger diameters minimize this effect.

Bifurcation pipes: Larger diameters (D=6,8,10 mm) and bigger bifurcation angles (θ=50°,70°) lead to smoother and more uniform velocity distributions. Narrow pipes and sharper angles result in abrupt pressure drops, whereas larger diameters and smoother angles reduce pressure losses.

Trifurcation pipes: Increasing diameter (D=6,8,10 mm) spreads velocity uniformly, reducing central concentration and turbulence. Smaller diameters and shorter pipes exhibit the highest-pressure drops. Larger diameters reduce resistance, balancing flow and minimizing losses, even in longer pipes.

As a result, larger diameters (D=10 mm) and smoother transitions (θ=70°) increase flow uniformity, reduce turbulence and minimize pressure drops. Smaller diameters and sharper angles increase resistance and losses.

References

Alharbi, A. Y., Pence, D. V., & Cullion, R. N. (2003). Fluid flow through microscale fractallike branching channel networks. *J. Fluids Eng., 125(6), 1051-1057.*

Bejan, A. (1997). Constructal tree network for fluid flow between a finite-size volume and one source or sink. *Revue generale de thermique, 36(8), 592-604.*

Blonski, S., Zaremba, D., Jachimek, M., Jakiela, S., Wacławczyk, T., & Korczyk, P. (2020). Impact of inertia and channel angles on flow distribution in microfluidic junctions. *Microfluidics and Nanofluidics, 24(2), 1-15.*

Chen, Y., & Cheng, P. (2002). Heat transfer and pressure drop in fractal tree-like microchannel nets. *International Journal of Heat and Mass Transfer, 45(13), 2643-2648.*

Colak, A.B. (2017). Tree shaped by bifurcation channels parallel and counter flow of heat exchanger heat transfer and flow investigation characteristics. [Master Thesis, Atatürk University, Institute of Science and Technology, Turkey]

Colak, A. B., Kotcioglu, I., & Khalaji, M. N. (2018). Tree Shaped in Channels Parallel and Counter Flow Through Heat Exchanger Heat Transfer and Flow Investigation of Characteristic. *Hittite Journal of Science and Engineering, 5, 33-49.*

Kotcioğlu, D. D. İ. (2017). Ağaç şekilli dal kanallı zıt ve paralel akışlı ısı değiştiricisinin ısı transferi ve akış karakteristiklerinin incelenmesi [Doctoral dissertation].

Lee, J. Y., & Lee, S. J. (2010). Murray's law and the bifurcation angle in the arterial microcirculation system and their application to the design of microfluidics. *Microfluidics and nanofluidics, 8(1), 85-95.*

Muwanga, R., Hassan, I., & Ghorab, M. (2008). Numerical investigation of a radial microchannel heat exchanger with varying cross-sectional channels. *Journal of thermophysics and heat transfer, 22(3), 321-332.*

Senn, S., & Poulikakos, D. (2004). Laminar mixing, heat transfer and pressure drop in tree-like microchannel nets and their application for thermal management in polymer electrolyte fuel cells. *Journal of Power Sources, 130(1-2), 178-191.*

Wang, X.-Q., Xu, P., Mujumdar, A. S., & Yap, C. (2010). Flow and thermal characteristics of offset branching network. *International Journal of Thermal Sciences*, 49(2), 272-280.

Effect of Rectangular Flow Elements and Different Fluids Used on Efficiency in High Emissivity Solar Collector

Yüksek Emisiviteli Güneş Kollektörlerinde Dikdörtgen Türbülatörlerin ve Kullanılan Farklı Akışkanların Verimliliğe Etkisi

Fırat TUNA[1] (iD)
Ahmet Numan ÖZAKIN[1] (iD)
Abdüssamed KABAKUŞ[2] (iD)
Gökhan ÖMEROĞLU[1] (iD)

[1]Atatürk University, Faculty of Engineering, Mechanical Engineering Erzurum, Türkiye .

[2]Artvin Çoruh University Artvin Vacational School Artvin, Türkiye

ABSTRACT

This study investigates the effects of turbulators (1, 5 and 9 per tube in a spiral arrangement) and advanced matte black coatings that providing high emissivity (Black 2.0 and Black 3.0) on the thermal performance of flat plate solar water heater (FPSWH) systems. It also evaluates the effect of different heat transfer fluid (HTFs) (ethylene glycol, ammonia and water) at varying flow rates using ANSYS-Fluent software for simulation. An experimental design approach based on Response Surface Methodology (RSM) was used to optimize the system parameters for maximum efficiency. The findings highlight the importance of optimizing absorber plate designs, improving heat transfer mechanisms and integrating advanced materials to enhance FPSWH performance. The adoption of solar water heaters not only reduces dependence on fossil fuels but also aligns with global sustainability goals by reducing environmental impacts and addressing energy security concerns. As solar energy continues to dominate renewable energy applications, hybrid technologies and developments in FPSWH systems are critical to meet the growing global energy demand in a sustainable manner.

Keywords: Solar energy, Optimization, FPSWH, CFD Analysis

ÖZ

Bu çalışmada, türbülatörlerin (spiral şekildeki tüp başına 1, 5 ve 9) ve mat siyah kaplamanın (Black 2.0 ve Black 3.0) düz plakalı güneş enerjili su ısıtıcı sistemlerinin termal performansı üzerindeki etkileri araştırılmıştır. Ayrıca, simülasyon için ANSYS-Fluent yazılımı kullanılarak farklı akış hızlarında farklı ısı transfer sıvılarının (etilen glikol, amonyak ve su) etkisi değerlendirilmiştir. Maksimum verimlilik için sistem parametrelerini optimize etmek amacıyla Yüzey Yanıt Metodolojisi'ne (RSM) dayalı deneysel bir tasarım yaklaşımı kullanılmıştır. Bulgular, soğurucu plaka tasarımlarını optimize etmenin, ısı transfer mekanizmalarını iyileştirmenin ve FPSWH performansını artırmak için gelişmiş malzemeleri entegre etmenin önemini vurgulamaktadır. Güneş enerjili su ısıtıcılarının benimsenmesi yalnızca fosil yakıtlara olan bağımlılığı azaltmakla kalmaz, aynı zamanda çevresel etkileri azaltarak ve enerji güvenliği endişelerini ele alarak küresel sürdürülebilirlik hedefleriyle de uyumludur. Güneş enerjisi yenilenebilir enerji uygulamalarına hâkim olmaya devam ederken, hibrit teknolojiler ve FPSWH sistemlerindeki gelişmeler, büyüyen küresel enerji talebini sürdürülebilir bir şekilde karşılamak için kritik öneme sahiptir.

Anahtar Kelimeler*: Güneş enerjisi, Optimizasyon, FPSWH, CFD Analizi

Introduction

A substantial amount of energy is consumed for water heating in hospitals, residential applications, and various industries. Conventional energy sources, such as coal, natural gas, and oil, are widely used around the world to meet energy demands. However, the usage of these energy sources for water heating is extensive, leading to greenhouse gas emissions that contribute to environmental pollution and climate change. Furthermore, the depletion of fossil fuels has become a growing concern. To reduce the consumption of fossil fuels, various renewable energy sources are considered viable alternatives (Jamar et al. 2016; Özakin & Kaya, 2020).

In developing countries, solar energy is a prominent alternative in numerous industrial and manufacturing sectors to reduce fossil fuel consumption and mitigate environmental impact. Solar water heating (SWH-Solar Water Heater) is an effective method of utilizing solar energy to produce hot water or steam for industrial heating and polygeneration. When selecting solar thermal collectors, factors such as energy requirements, required temperature range, and system economics are significant. Among various solar thermal collectors, flat plate solar water heaters (FPSWH) are widely utilized due to their simple construction, smooth operation, low maintenance needs, and cost-effectiveness (Vengadesan et al. 2020).

However, the thermal efficiency of the FPSWH (Flat Plate Solar Water Heater) system is a critical factor in designing an economically viable SWH system. The more cost-effective the system, the lower its efficiency tends to be, while higher efficiency may lead to a greater total annual cost (TAC). In renewable energy utilization, the energy payback period (EPBP), which measures the time required for a solar system to recover the energy invested in its construction, is an important factor. A thermoeconomic FPSWH system can achieve reduced TAC and improved collector efficiency.

As global energy demand continues to rise due to population growth, industrialization, and improved living standards, solar energy remains the most widely used renewable energy source, being environmentally friendly, economically advantageous, clean, and carbon-free (Bazri et al. 2019). Solar thermal applications are especially common for domestic and industrial water heating purposes due to their simplicity and effectiveness (Li et al. 2017; Abuska, 2018; Bazri et al. 2019).

Solar water heaters (SWH) are commonly employed in both industrial and residential sectors to reduce the consumption of conventional fuels by preheating water. Two popular types of solar water heaters are the Flat Plate Solar Water Heater (FPSWH) and the Evacuated Tube Collector (ETC) solar water heater. The ETC utilizes double glass pipes with an inner heat pipe to absorb solar radiation, and its heat loss is minimized by evacuating the space within the tube (Li et al., 2020). FPSWH is a widely used collector, designed to provide temperatures between 50–100 °C. The thermosiphon FPSWH operates on natural water circulation due to the thermosiphon effect, while the forced circulation FPSWH uses a pump in a closed-loop system. According to Diego-Ayala and Carrillo (2016), the forced circulation system generally performs better in terms of daily energy efficiency due to forced convection.

Various methods have been explored to improve FPSWH efficiency. Enhancements include optimizing the optical properties of absorber materials, adding more glass covers to reduce heat loss, and using polymer absorbers or nanofluids as heat transfer fluids (HTFs). Additionally, new absorber plate designs, mini and micro channels for fluid flow, and energy storage integration have been shown to improve performance (Pandey & Chaurasiya, 2017).

FPSWH systems traditionally suffer from low thermal efficiency due to poor heat transfer between the absorber and HTF. To address this, both active and passive methods are employed. Passive methods focus on enhancing heat transfer in absorber tubes, using devices such as twisted tape (Sandhu et al., 2014), wire coil inserts (García et al. 2013), vortex generators (Silva et al. 2019; Wang et al. 2019), and other flow inserts to create turbulence and improve fluid mixing. Additionally, different nanofluids (e.g., aluminium oxide/water, CuO/water, and SiO_2/water) have been studied to enhance heat transfer and increase the efficiency of water heaters (Boyaghchi & Montazerinejad, 2016; Said et al. 2016; Shojaeizadeh & Veysi, 2016).

Integrating Thermal Energy Storage (TES) with FPSWH allows solar energy to be stored for use during evening hours, significantly boosting overall efficiency (Bazri et al. 2019). The thermal performance of solar water heaters thus involves optimizing absorber designs, heat transfer fluids, thermal energy storage, and improving heat transfer mechanisms.

Another research area is hybrid solar energy systems that combine solar thermal and photovoltaic (PV) technologies. While solar thermal and PV technologies are well-commercialized, the hybrid solar thermal-PV system, which simultaneously provides hot water and electricity, is still under extensive research and development. Although only a few studies have been published on this hybrid system, many researchers are working toward its commercialization (Michael & Iniyan, 2017).

Due to the depletion of conventional energy sources and their adverse environmental impacts, the adoption of renewable energy for water heating has become increasingly critical. Solar

energy emerges as a prominent alternative, particularly in developing countries, where it is widely applied in industrial and residential sectors. Flat plate solar water heaters (FPSWH) are commonly utilized due to their simplicity, cost-effectiveness, and low maintenance requirements. However, improving the efficiency of these systems has driven innovations such as advanced heat transfer fluids (e.g., nanofluids), optimized absorber plate designs, and the integration of thermal energy storage. Furthermore, hybrid technologies that combine solar thermal and photovoltaic systems are gaining attention for their ability to simultaneously produce hot water and electricity. These advancements aim to enhance energy efficiency and reduce reliance on fossil fuels, contributing to sustainable energy solutions.

In this study, the effects of adding different numbers (1-5-9 for a single pipe of the spiral) of elements that create local turbulence in the flow (turbulators) and the matte black coatings Black 2.0 and Black 3.0 on the flat plate solar collector on the system performance has investigated. Additionally, in this research, the effects of different fluids (Ethylene glycol, Ammonia and Water) and their flow rates on system performance were evaluated using ANSYS-Fluent software. In this article, variable parameters were also optimized by making an experimental plan with the Response Surface (RSM) experimental optimization method.

Material and Methods

In this study, which was conducted to heat the domestic water more effectively by using solar energy, simulations were performed with three different numbers of rectangular turbulators, three different absorbency coatings, three different heat transfer fluids and three different flow rates. The geometries in which the analyses were made are shown in Figure 1.

In the experiments designed with the Response Surface experiment optimization method, solutions were made by creating mesh elements for the geometries given in Figure 1. In this step, the analyses were first made by starting with a mesh element number of around 250,000 and were progressed in iterations, resulting in the fluid outlet temperature converging to a certain value. As a result, analyses were made by obtaining approximately 555,000 mesh elements and 0.945 "Orthogonal Quality" before starting the analyses. The mesh network structure used in the relevant analyses is shown in Figure 2.

In the model where the mesh structure is seen in Figure 2, the aluminum pipe is fixed to the copper plate. It is noticeable that the mesh structure on the plate is denser in the parts where the rectangular fins placed in the aluminum pipe to increase the

turbulence of the flow and increase heat transfer. Analyses were performed with pressure based, k-epsilon turbulence model and under steady state conditions.
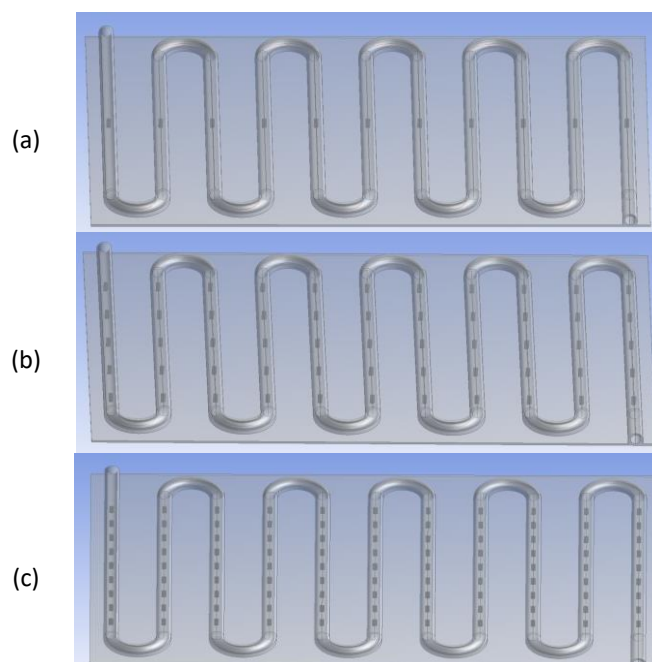
Figure 1.
Cases with 1, 5 and 9 rectangular turbulators on the pipe. a: 1 turbulator, b: 5 turbulators, c: 9 turbulators.
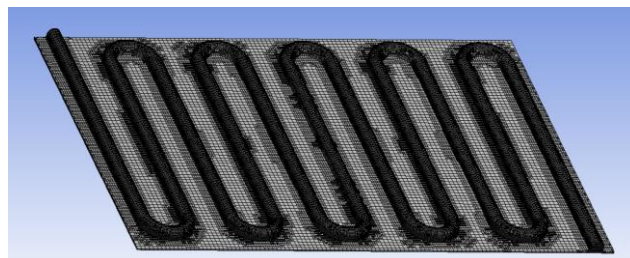
Figure 2.
Cell structure of mesh elements used in the analysis.

The Response Surface Method was used to determine the experimental design and optimum parameter values. This method is a common method used to determine the variable parameters and parameter values affecting the result variable. In the Response Surface Method, after the problem is first determined, the variable parameters and the result variable are determined. After the parameter levels are determined, the appropriate experimental design is selected. After the experiments are carried out according to the experimental design, the accuracy of the design is tested with variance analysis. Finally, the optimum parameters and their values are determined (Öztürk et al. 2023). The selected experimental parameters and values are shown in Table 1.

Table 1.
Design parameters and levels.

Parameters	Levels		
	Low	Middle	High
Number of Turbulators	1	5	9
Flow rate (kgh⁻¹)	50	100	150
Fluid	Water	Ammonia	Ethylene glycol
Collector type	Standard	Black 2.0	Black 3.0

Results And Discussion

In the numerical study, the optimum parameters affecting the thermal efficiency of the flat plate solar collector were determined. In the analysis, the fluid type, collector type, fluid flow rate and turbulator number were determined as variable parameters. The experimental design and analysis were carried out using the Minitab 18 program. The experimental design was determined with the "Central composite" approach using the response surface method. The experimental design and heat values created for the heat energy obtained from the solar collector are given in Table 2.

As a result of the variance analysis performed for the heat energy obtained from the collector. the R^2 value was determined as 99.99% and R^2adj as 99.97%. R^2 expresses the accuracy of the experimental design and the R^2adj value is the corrected squares value obtained by removing the insignificant values. The fact that the R^2 and R^2adj values are close to each other and to 100% indicates that the experimental design and results are significant (Öztürk et al. 2023). When the R^2 values obtained as a result of the analysis are examined. it is seen that the design used is significant. The effect rates of the variable parameters on the amount of heat obtained from the collector are given in Table 3.

When the variance analysis table is examined. it is seen that the parameters with a P-value less than 0.005 are the main effects of flow rate. number of turbulators and fluid. This shows that the parameters in question have a significant effect on the result variable. It is seen that the parameter that affects the result variable the most is the fluid fluid type with 56.48%. The result variable is affected by the collector type with 1.20%.

Figure 3 shows the Pareto chart showing the parameters affecting the heat energy obtained from the collector (the result variable) in the form of a column chart. In the Pareto chart. the columns passing the reference line (2.12 in this study) are effective on the result variable. When the Pareto chart is examined. it can be said that in addition to the main effects of fluid type and collector type. the square effect of the fluid type

and the combined effect of fluid type and collector type are the parameters affecting the result variable.
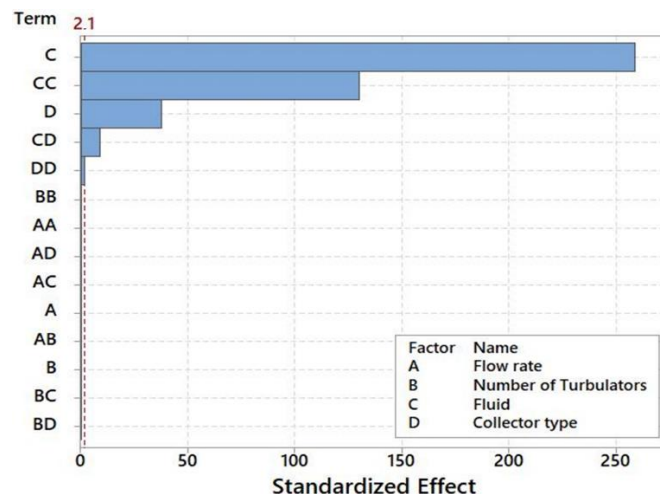
Figure 3.
Pareto chart for heat energy obtained from the collector.

Figure 4 shows the contour graph of the number of turbulators and flow rate for the Black 3.0 collector and Ammonia. It is seen that the maximum amount of heat obtained from the solar collector for the Black 3.0 collector and Ammonia is at a collector with 1-9 turbulators and a flow rate of 100 kgh⁻¹.
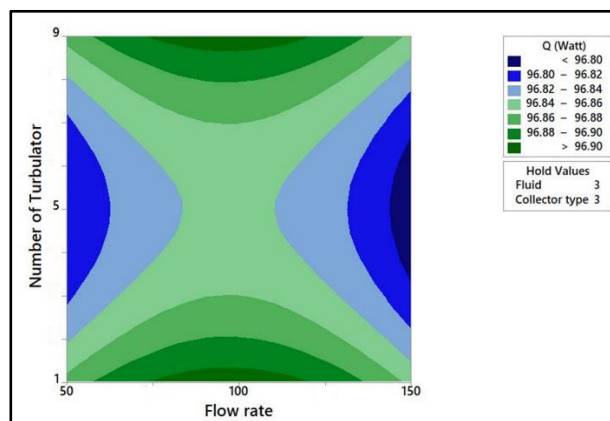
Figure 4.
Number of turbulators vs flow rate graph for Black 3.0 collector and ammonia.

Figure 5 shows the flow-fluid contour graph for the Black 3.0 collector and the 9-turbulator collector. When the graph is examined. it is seen that the highest heat energy is in Ammonia. Also. the amount of heat obtained with the change in flow rate has not changed.

Figure 6 shows the flow-collector type contour graph for Ammonia and 9 turbulators. When the graph is examined, it is seen that the amount of heat obtained from the collector increases as the flow rate increases. It is seen that the maximum amount of heat obtained from the solar collector for the 9

turbulator collector and Ammonia is Black 3.0 collector type and 150 kg/h flow rate.

Table 2.
Experimental plan and Q values.

Flow rate ($l.h^{-1}$)	Number of Turbulators	Fluid	Collector Type	Q(watt)
50	1	Water	Black 3.0	59.31
50	9	Liquid ammonia	Black 3.0	97.01
100	5	Ethylene glycol	Black 2.0	51.05
50	9	Liquid ammonia	Standard	90.14
150	1	Liquid ammonia	Black 3.0	96.94
100	5	Ethylene glycol	Black 2.0	51.05
50	5	Ethylene glycol	Black 2.0	50.85
100	5	Ethylene glycol	Black 2.0	51.05
50	1	Liquid ammonia	Black 3.0	97.01
150	1	Water	Standard	55.08
100	1	Ethylene glycol	Black 2.0	51.05
50	9	Water	Black 3.0	59.32
100	5	Ethylene glycol	Black 2.0	51.05
150	9	Liquid ammonia	Standard	90.20
50	1	Liquid ammonia	Standard	90.14
100	5	Ethylene glycol	Black 3.0	53.19
150	9	Water	Black 3.0	59.26
150	5	Ethylene glycol	Black 2.0	51.02
100	5	Ethylene glycol	Standard	49.44
100	5	Ethylene glycol	Black 2.0	51.05
50	9	Water	Standard	55.13
100	5	Liquid ammonia	Black 2.0	93.04
150	9	Water	Standard	55.08
150	1	Liquid ammonia	Standard	90.20
50	1	Water	Standard	55.13
100	5	Ethylene glycol	Black 2.0	51.05
100	5	Water	Black 2.0	56.94
100	9	Ethylene glycol	Black 2.0	51.05
150	1	Water	Black 3.0	59.26
100	5	Ethylene glycol	Black 2.0	51.05
150	9	Liquid ammonia	Black 3.0	96.94
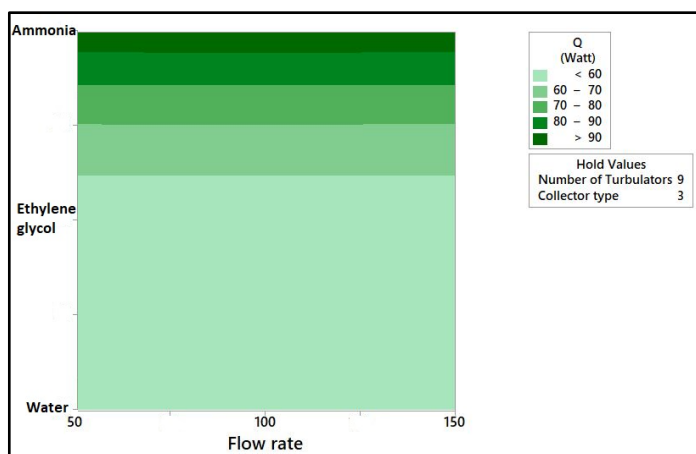
Figure 5.
Flow rate-fluid graph for standard collector and 9 turbulators.
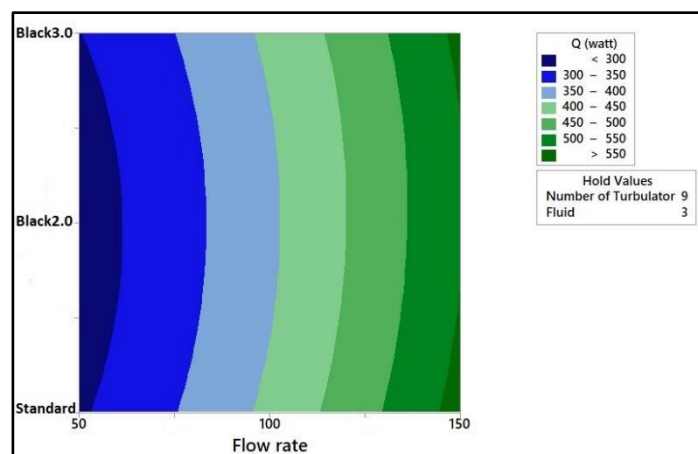
Figure 6.
Flow rate - collector type chart for ammonia and 9 turbulators.

Table 3.
Variance analysis for heat energy obtained from the collector.

Source	DF	Seq SS	Contribution	Adj SS	Adj MS	F-Value	P-Value
Model	14	10524.4	99.99%	10524.4	751.74	8507.43	0.000
Linear	4	6071.6	57.68%	6071.6	1517.91	17178.10	0.000
Flow rate	1	0.0	0.00%	0.0	0.00	0.00	0.960
Number of Turbulators	1	0.0	0.00%	0.0	0.00	0.00	1.000
Fluid	1	5945.2	56.48%	5945.2	5945.16	67281.00	0.000
Collector Type	1	126.5	1.20%	126.5	126.48	1431.42	0.000
Square	4	4445.9	42.24%	4445.9	1111.47	12578.42	0.000
Flow rate*Flow rate	1	2416.9	22.96%	0.0	0.01	0.07	0.791
Number of Turbulators*Number of Turbulators	1	373.9	3.55%	0.0	0.01	0.13	0.719
Fluid*Fluid	1	1654.8	15.72%	1495.8	1495.76	16927.36	0.000
Collector Type*Collector Type	1	0.3	0.00%	0.3	0.29	3.32	0.087
2-Way Interaction	6	6.9	0.07%	6.9	1.15	13.00	0.000
Flow rate*Number of Turbulators	1	0.0	0.00%	0.0	0.00	0.00	1.000
Flow rate*Fluid	1	0.0	0.00%	0.0	0.00	0.04	0.848
Flow rate*Collector Type	1	0.0	0.00%	0.0	0.00	0.05	0.827
Number of Turbulators*Fluid	1	0.0	0.00%	0.0	0.00	0.00	1.000
Number of Turbulators*Collector Type	1	0.0	0.00%	0.0	0.00	0.00	1.000
Fluid*Collector Type	1	6.9	0.07%	6.9	6.88	77.90	0.000
Error	16	1.4	0.01%	1.4	0.09		
Lack-of-Fit	10	1.4	0.01%	1.4	0.14		
Pure Error	6	0.0	0.00%	0.0	0.00		
Total	30	10525.8	100.00%				
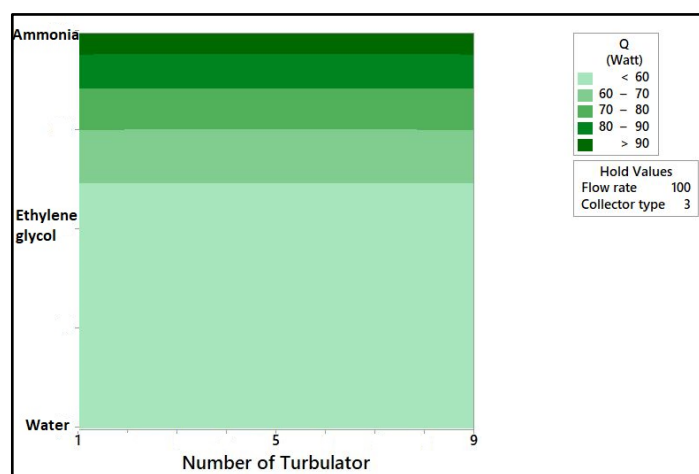
Figure 7.
Fluid type-turbulator number graph for 100 kg/h flow rate and Black 3.0 collector.

Figure 7 shows the contour graph of the number of fluid-turbulators for a flow rate of 100 kg/h and Black 3.0 collector. Changing the number of turbulators did not change the amount of heat obtained from the collector. It is seen that the maximum amount of heat obtained from the solar collector for a flow rate of 100 kg/h and Black 3.0 collector is in the collector with ammonia.

Figure 8 shows the collector type-turbulator contour graph for 100 kg/h flow rate and ammonia. It is seen that the maximum amount of heat obtained from the solar collector for 100 kg/h flow rate and ammonia is with the Black3.0 collector.

Figure 9 shows the collector type-fluid contour graph for 100 kg/h flow rate and 9 turbulators. It is seen that the maximum heat amount obtained from the solar collector for 150 kg/h flow rate and ammonia is with Ammonia and Black3.0-Standard collector.

Figure 10 shows the optimum parameter values. The sharper the curves change in this graph. the more effective it is on the result variable. When the graph is examined, it is seen that the parameters that affect the result variable the most are the fluid type and the collector type. Flow rate and Number of turbulators did not make a big difference on the amount of heat obtained from the collector. y (96.9112) represents the maximum heat

energy obtained from the collector. Red lines show the optimum parameter values. As a result. the optimum parameter values for maximum collector efficiency were determined as 100 kg/h flow rate. 9 turbulator numbers. ammonia fluid type and Black 3.0.
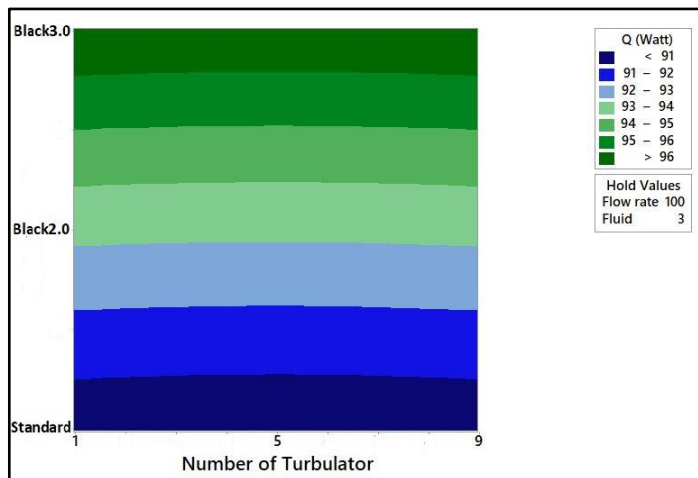
Figure 8.
Collector type-turbulator number graph for 100 kg/h flow rate and ammonia.
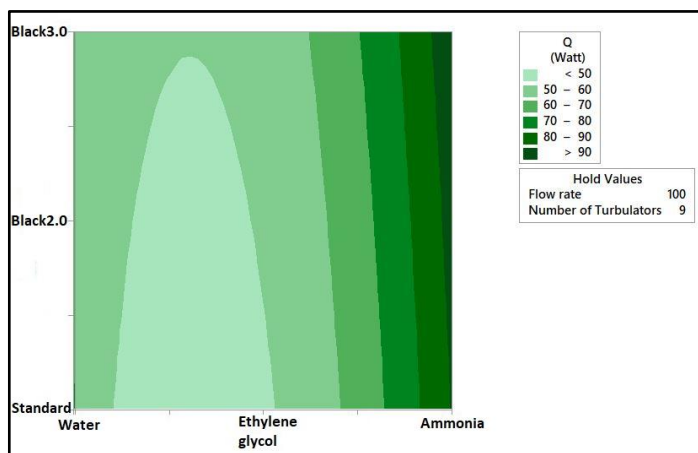
Figure 9.
Collector type-fluid chart for 100 kg/h flow rate and 9 turbulators.
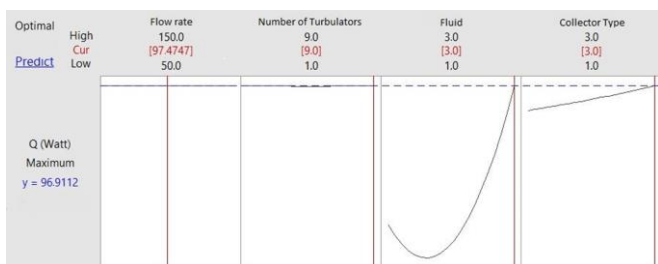
Figure 10.
Optimum parameter values for maximum heat energy obtained from the collector.

References

Abuşka, M. (2018). Energy and exergy analysis of solar air heater having new design absorber plate with conical surface. *Applied Thermal Engineering, 131, 115-124.*

Bazri, S., Badruddin, I. A., Naghavi, M. S., Seng, O. K., & Wongwises, S. (2019). An analytical and comparative study of the charging and discharging processes in a latent heat thermal storage tank for solar water heater system. *Solar Energy, 185, 424-438.*

Boyaghchi, F. A., & Montazerinejad, H. (2016). Multi-objective optimisation of a novel combined cooling, heating and power system integrated with flat plate solar collectors using water/CuO nanofluid. *International Journal of Exergy, 21(2), 202-238.*

Da Silva, F. A., Dezan, D. J., Pantaleao, A. V., & Salviano, L. O. (2019). Longitudinal vortex generator applied to heat transfer enhancement of a flat plate solar water heater. *Applied Thermal Engineering, 158, 113790.*

Diego-Ayala, U., & Carrillo, J. G. (2016). Evaluation of temperature and efficiency in relation to mass flow on a solar flat plate collector in Mexico. *Renewable Energy, 96, 756-764.*

García, A., Martin, R. H., & Pérez-García, J. (2013). Experimental study of heat transfer enhancement in a flat-plate solar water collector with wire-coil inserts. *Applied Thermal Engineering, 61(2), 461-468.*

Jamar, A. M. Z. A. A., Majid, Z. A. A., Azmi, W. H., Norhafana, M., & Razak, A. A. (2016). A review of water heating system for solar energy applications. *International Communications in Heat and Mass Transfer, 76, 178-187.*

Li, Q., Moya, W., Esfahani, I. J., Rashidi, J., & Yoo, C. (2017). Integration of reverse osmosis desalination with hybrid renewable energy sources and battery storage using electricity supply and demand-driven power pinch analysis. *Process Safety and Environmental Protection, 111, 795-809.*

Michael, J. J., & Selvarasan, I. (2017). Economic analysis and environmental impact of flat plate roof mounted solar energy systems. *Solar energy, 142, 159-170.*

Özakın, A. N., & Kaya, F. (2020). Experimental thermodynamic analysis of air-based PVT system using fins in different materials: Optimization of control parameters by Taguchi method and ANOVA. *Solar Energy, 197, 199-211.*

Öztürk, A., Sönmez, F., & Kabakuş, A. (2024). Determination of optimum parameters using different nano fluids in heat pipe heat exchangers with response surface method. *Chemical Engineering Communications*, 211(5), 725-735.

Pandey, K. M., & Chaurasiya, R. (2017). A review on analysis and development of solar flat plate collector. *Renewable and Sustainable Energy Reviews*, 67, 641-650.

Said, Z., Saidur, R., & Rahim, N. A. (2016). Energy and exergy analysis of a flat plate solar collector using different sizes of aluminium oxide based nanofluid. *Journal of cleaner production, 133, 518-530.*

Sandhu, G., Siddiqui, K., & Garcia, A. (2014). Experimental study on the combined effects of inclination angle and insert devices on the performance of a flat-plate solar collector. *International Journal of Heat and Mass Transfer*, 71, 251-263.

Shojaeizadeh, E., & Veysi, F. (2016). Development of a correlation for parameter controlling using exergy efficiency optimization of an Al2O3/water nanofluid based flat-plate solar collector. *Applied Thermal Engineering, 98, 1116-1129.*

Vengadesan, E., & Senthil, R. (2020). A review on recent development of thermal performance enhancement methods of flat plate solar water heater. *Solar Energy, 206, 935-961.*

Wang, Y., Liu, P., Shan, F., Liu, Z., & Liu, W. (2019). Effect of longitudinal vortex generator on the heat transfer enhancement of a circular tube. *Applied Thermal Engineering, 148, 1018-1028.*

The Emittance and Absorptance of External Surfaces Values Effect for Payload Panels on Geostationary Orbit Satellite: Thermal Analysis Studies

Yeredurağan Yörünge Uydusu Üzerindeki Görev Yükü Panelleri için Dış Yüzeylerin Yayılımı ve Emilimi Değerlerinin Etkisi: Isıl Analiz Çalışmaları

Murat BULUT (iD)
Nedim SÖZBİR (iD)

Düzce University, Faculty of Engineering, Mechanical Engineering, Düzce, Türkiye.

ABSTRACT

One of the most important parameters in the dimensioning stages of communication satellites is the calculation of the areas where the heat to be released into space is located. The satellite thermal control system calculates these areas. Thermal analyses are performed for the north and south panels where the payload equipment is located in three-axis geostationary satellites. It is important to calculate these areas where the heat to be released into space is located correctly. In this study, thermal analysis calculations were performed for a three-axis geostationary satellite with an area of 1 to 10 m^2. In the calculations, the absorptance of external surfaces at the end of the satellite's life was calculated by considering 0.27. The radiator area temperature was taken as 30 °C in the calculations.

Keywords: Geostationary orbit, satellite, thermal analysis.

ÖZ

Haberleşme uydularının boyutlandırılması aşamalarında en önemli parametrelerinden bir tanesi uzaya atılacak olan ısının yer aldığı alanları hesaplanmasıdır. Uydu ısıl kontrol sistemi bu alanları hesaplamaktadır. Üç eksenli yeredurağan uydularda faydalı yük ekipmanların yer aldığı kuzey ve güney panelleri için ısıl analizler yapılmaktadır. Uzay ortamına atılacak ısının yer aldığı bu alanları doğru bir şekilde hesaplanması önem arz etmektedir. Bu çalışmada, 1 ile 10 m^2'lik bir alana sahip üç eksenli yere durağan bir uydu için ısıl analiz hesabı yapılmıştır. Hesaplamalarda uydunun ömrü sonundaki yüzey soğurulma katsayısı 0.27 göz önüne alınarak hesaplanmıştır. Hesaplamalarda radyatör alan sıcaklığı 30 °C olarak alınmıştır.

Anahtar Kelimeler: Yeredurağan yörünge, uydu, ısıl analiz.

Introduction

Radiator areas for heat dissipation have existed since the first satellite mission. With the increasing heat generated by electronic equipment with the development of technology, the optimization of radiator areas has become an important subject of study in space technology in recent years. Especially in various planetary missions, the design of radiator areas where heat rejection occurs is carried out by thermal control workers as high efficiency, low mass and deployable as possible.

The importance of radiator areas has been realized due to the increase in radiator areas together with the increase in heat loads produced by electronic equipment in satellite. Consequently, pioneering studies were initiated in 1968 to investigate the role of radiator areas on the structural

subsystem in spacecraft applications (Cockfield, 1968). In the study, studies were conducted on the optimization of mass, which is one of the most important criteria of the structural subsystem, together with the increase in the radiator area. Important studies have been conducted on the optimization of radiator areas as a thermal subsystem in recent years (Curran & Lam, 1996; Krikkis & Razelos, 2002; Hull et al. 2006; Kim et al. 2015). Chiranjeevi et. al (2023) conducted a comprehensive study that incorporated numerical simulations, experimental investigations, and optimization of hybrid space thermal radiators, resulting in a substantial reduction in mass from 6.8 kg to 4.3 kg.   Liu et al. (2016) investigated the degradation characteristics of two thermal control coatings, employing a winner process to model the degradation of absorptivity. The degradation modeling method is accurate, and the results provide insight into the life prediction and thermal design optimization of LEO satellites. Shen et al. (2024) conducted thermal analysis throughout the satellite development process based on modeling and simulations. Bulut and Sözbir (2015) investigated the temperature for different solar panel combinations in a 1U CubeSat. Bulut et al. (2010) modeled CubeSat and the thermal analysis was performed by using ThermXL spreadsheet-based thermal analysis tool. Sözbir and Bulut (2009) ensure that the electronics in the payload panel remain at appropriate temperatures by calculating the radiator area. Arslantas et al. (2017) conducted a study in which they analyzed the surface temperatures for communication satellites based on thermal uncertainty values. The necessity of thermal analysis for geostationary and nanosatellites has been widely recognized, and significant research efforts have been dedicated to developing methods for maintaining internal satellite temperatures within acceptable limits (Sözbir et al. 2008; Bulut et al. 2008; Bulut et al. 2017; Bulut & Sözbir, 2021).

Geostationary satellites in geostationary orbit are approximately 36,000 km away from the Earth. Mostly, they are designed by satellite manufacturing companies with three axes. Heat rejection to space in three-axis geostationary satellites is done using radiator areas located on the north and south panels. Figure 1 shows a three-axis geostationary satellite (Coşkun et al. 2016). The north and south panels where the heat is released are covered with optical solar reflectors (OSR). OSR's are materials with high surface emission coefficients and low surface absorption coefficients.

In this study, thermal analysis of the heat rejection capacity to space from the radiator areas in the panels where the payload is located in three-axis geostationary satellites was performed analytically.
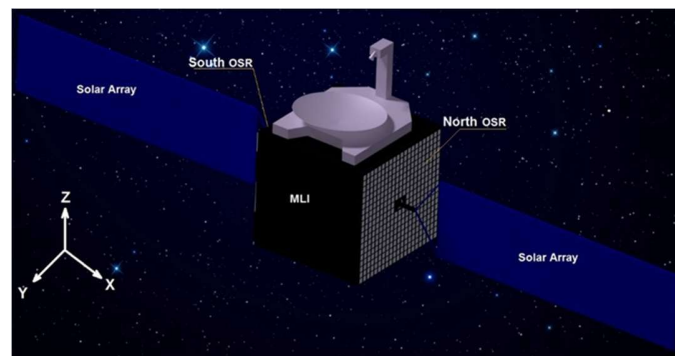
Figure 1.
Three-axis geostationary satellite (Coşkun, Bulut & Sözbir, 2016).

Material and Methods

Thermal Analysis Model
In the thermal analysis model of the satellite, OSR's and thermo-optic values are important. Radiator areas and OSR's attached to external surface of the satellite provide heat to be released into space. In the calculation of radiator areas, the worst cases such as maximum heat transfer, maximum solar radiation end-of-life (EOL) thermo-optic properties are taken into consideration (Bulut et al. 2008; Sözbir et al. 2008; Sözbir & Bulut, 2009; Sözbir et al. 2010). In the thermal analysis model of satellites, the heat absorbed by the satellite with radiation and the heat emitted by the satellite must be balanced (energy balance). The energy balance is shown in Figure 2.
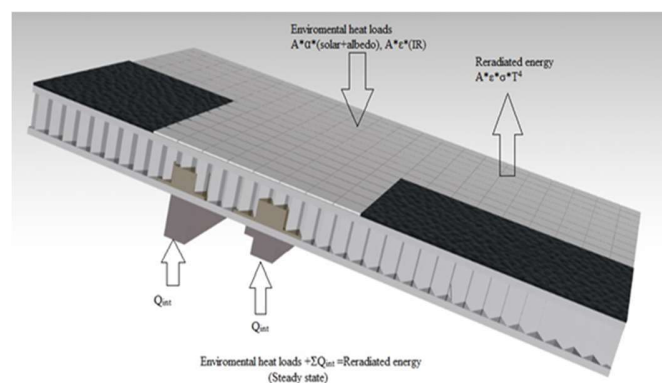
Figure 2.
Energy balance in a three-axis geostationary satellite (Bulut & Sözbir, 2023).

The energy balance in three-axis geostationary satellites is obtained by the following equation.

$$Q_S + Q_A + Q_E + Q_{int} = Q_{Surface} \tag{1}$$

The internally dissipated power is Q_{int}, and the environmental heat loads associated with solar, albedo, and Earth are Q_S, Q_A,

and Q_E. The amount of heat rejected from the satellite's radiator surface is $Q_{Surface}$.

$$(A_S q_S + A_A q_A)\alpha + A_E q_E \varepsilon + Q_{int} = A_{surface}\sigma(T_r^4 - T_s^4)\varepsilon \quad (2)$$

The left side of the equation shows the absorbed heat, the right side shows the heat emitted by the satellite. The first and second terms on the left side of the equation show the net absorbed heat, and the third term shows the operating heat load (heat produced by the elements in the satellite). A_S, A_A, and A_E are the surface areas related to direct solar, reflected (albedo) and directly emitted infrared radiation from the earth. q_S, q_A, and q_E are the heat fluxes from direct solar, reflected (albedo) and directly emitted infrared radiation from the earth. the absorptance of external surfaces is shown as α and the emittance of external surfaces as ε in equation (1). In three-axis geostationary satellites, the absorptance of external surfaces values range between 0.24 and 0.27 at EOL of the satellite. In this study, the absorptance of external surfaces (α) is taken as 0.27 in the calculations. The changes in the absorptance of external surfaces values depend on the time the satellite is in space, the location of the OSR's on the satellite, and pollution from external environments (Karam, 1998; Gilmore, 2002). Satellite manufacturers calculate the surface absorption coefficient values at the end of the satellite's life by taking into account the satellites they have previously sent into space. The emittance of external surfaces ε was calculated by taking 3 different values as 0.80, 0.85 and 0.90. In order calculate the radiative areas, 30 °C were chosen because the most of the electronic equipment in the spacecraft considered the qualification temperature of 65 °C.

Results

Table 1 shows the heat values rejected to space. For a radiator area of 1 m², a radiator temperature of 30 °C and a surface emission coefficient of 0.9, the amount of heat to be rejected is calculated as 431 W. For a radiator area of 10 m², a radiator temperature of 30 °C and the emittance of external surfaces of 0.9, the amount of heat to be rejected is calculated as 4310 W. The heat absorbed by the north and south payload panels are given in Tables 2, and 3.

Table 2 shows the total heat absorbed by the north payload panels (solar and electronic equipment) in the case that the radiator temperature is 30ºC and the absorptance of external surfaces is 0.27. For the north panel radiator area of 1 m² and the emittance of external surfaces of 0.9, the total absorbed heat is calculated as 348 W. For the north panel radiator area of

10 m² and the emittance of external surfaces of 0.9, the total absorbed heat is calculated as 3480 W.

Table 1.
Heat released into space (30 ºC)

Total Area (m²)	Q (W)		
	ε=0.8	ε=0.85	ε=0.9
1	383	407	431
2	766	814	862
3	1149	1221	1293
4	1532	1628	1724
5	1915	2035	2155
6	2299	2442	2586
7	2682	2849	3017
8	3065	3256	3448
9	3448	3663	3879
10	3831	4070	4310

Table 2.
North payload panel absorbed heat value (radiator area temperature 30 ºC)

North Panel Area (m²)	North Panel @ 30 ºC, α=0.27			
	QS (W)	Qint (W) @ε=0.8	Qint (W) @ε=0.85	Qint (W) @ε=0.9
1	143	293	321	348
2	286	587	641	696
3	428	880	962	1044
4	571	1174	1283	1392
5	714	1467	1603	1740
6	857	1761	1924	2088
7	999	2054	2245	2436
8	1142	2347	2566	2784
9	1285	2641	2886	3132
10	1428	2934	3207	3480

Table 3 shows the total heat absorbed by the south payload panels (solar and electronic equipment) in the case that the radiator temperature is 30ºC and the absorptance of external surfaces is 0.27. For the south panel radiator area of 1 m² and the emittance of external surfaces of 0.9, the total absorbed heat is calculated as 338 W. For the north panel radiator area of 10 m² and the surface emission coefficient of 0.9, the total absorbed heat is calculated as 3381 W.

Table 3.
South payload panel absorbed heat value (radiator area temperature 30 °C)

South Panel Area (m^2)	South Panel @ 30 °C, α=0.27			
	Q_S (W)	Q_{int} (W) @ε=0.8	Q_{int} (W) @ε=0.85	Q_{int} (W) @ε=0.9
1	153	284	311	338
2	305	567	622	676
3	458	851	932	1014
4	611	1134	1243	1352
5	763	1418	1554	1690
6	916	1701	1865	2028
7	1069	1985	2176	2366
8	1221	2268	2486	2704
9	1374	2552	2797	3043
10	1527	2835	3108	3381

Conclusions

In this study, the focus was on the calculation of heat rejection capacity in three-axis geostationary satellites, with specific attention given to the consideration of radiator areas. The lowest recorded heat rejection was determined to be 293 W, a figure achieved under conditions where the radiator temperature was set at 30°C, the radiator panel area was measured at 1 m², and the emittance of external surfaces was set at 0.8. Conversely, the maximum heat rejection was determined to be 3480 W under conditions of a radiator temperature of 30°C, a radiator panel area of 10 m², and an external surface emittance of 0.9.

The analytical calculation revealed a positive correlation between the emittance of external surfaces and the increase in heat rejection. Therefore, in order to achieve effective heat rejection in satellites, it is recommended that the optical solar reflector material be selected with a high emittance of external surfaces as a priority.

References

Arslantas, E., Bulut, M., & Sözbir, N. (2017). *The Effect of Uncertainty Values of Thermal Control System on GEO Satellites*. 8th International Conference on Recent Advances in Space Technologies-RAST 2017, Turkish Airforce Academy, Istanbul, Türkiye, 19-22 June.

Bulut, M., Sozbir, N., & Gulgonul, S. (2008). Thermal Control Design of TUSAT. 6th International Energy Conversion Engineering Conference (IECEC), Cleveland, OH, USA, July.

Bulut, M., Demirel, S., Sozbir, N., & Gulgonul, S. (2008). *Battery Thermal Design Conception of Turkish Satellite*. 6th International Energy Conversion Engineering Conference (IECEC), Cleveland, OH, USA, July.

Bulut, M., Kahriman, A., & Sozbir, N. (2010). *Design and Analysis for the Thermal Control System of Nanosatellite*, ASME 2010 International Mechanical Congress and Exposition, Vancouver, British Columbia, Canada, 12-18 November.

Bulut, M., Kahriman, A., & Sözbir, N. (2010). Uydularda Isıl Kontrol. *Termodinamik, (209), 72-78, January.*

Bulut, M., & Sözbir, N. (2015). Analytical Investigation of a Nanosatellite Panel Surface Temperatures for Different Altitudes and Panel Combinations. *Applied Thermal Engineering*, 75, 1076-1083.

Bulut, M., Sözbir, Ö.R., & Sözbir, N. (2017). *Thermal Control of Turksat 3U Nanosatellite*. 5th International Symposium on Innovative Technologies in Engineering and Science (ISITES2017) ,Bakü, Azerbaijan, 29-30 September.

Bulut, M., & Sozbir, N. (2021). Thermal Design, Analysis and Test Validation of TURKSAT-3USAT. *Journal of Thermal Engineering, 7 (3), 468-482.*

Bulut, M., & Sözbir, N. (2023). A novel approach to estimating dimensions of three-axis stabilized communication satellites with optimal heat transfer. *Journal of Thermal Analysis and Calorimetry, 148 (15), 3575-3584 August 2023*

Chiranjeevi, P.B., Krishnaraj, K., Vinod, K.G., Srinivasan, K., & Sundararajan, T. (2023). Numerical Simulations, Experimental Investigation and Optimization of Hybrid Space Thermal Radiators, *Applied Thermal Engineering, 234.*

Cockfield, R.D. (1968). Structural Optimization of a Space Radiator, *Journal Spacecraft Rockets, 5 (10), 1240–1241.*

Coşkun, H., Bulut, M., & Sözbir, N. (2016). *Uydularda optik güneş reflektörü ile ısıl kontrol ve uygulama yöntemi*, VI. Ulusal Havacılık ve Uzay Konferansı, Kocaeli Üniversitesi, Kocaeli, Türkiye, 28-30 September.

Curran D.G.T., & Lam, T.T. (1996). Weight Optimization for Honeycomb Radiators with Embedded Heat Pipes. *Journal of Spacecraft and Rockets, 33 (6), 822-828.*

Gilmore D.G. (2002). Spacecraft Thermal Control Handbook Vol. 1, 2nd edition. The Aerospace Corporation, CA, USA.

Hull, P.V., Tinker, M., SanSoucie, M., & Kittredge, K. (2006). *Thermal analysis and shape optimization for an in-space radiator using genetic algorithm.* SpaceTechnol. Int. Forum CP813, 81-90.

Karam D.R. (1998). Satellite Thermal Control for System Engineers, AIAA, Inc.,VA.

Kim, H., Choi, S., Park, S., & Lee, K.Ho. (2015). Node-based Spacecraft Radiator Design Optimization. *Advances in Space Research, (55), 1445-1469.*

Krikkis, R.N., & Razelos, P. (2002). Optimum Design of Spacecraft Radiators with Longitudinal Rectangular and Triangular Fins. *Journal of Heat Transfer, (124), 805-811.*

Liu, T., Sun, Q., Meng, J., Pan, Z., & Tang, Y. (2016). Degradation Modeling of Satellite Thermal Control Coatings in a Low Earth Orbit Environment, *Solar Energy*, 139, 467-474.

Shen, M., Zhang, L., Sun, Z., Kong, L., Liu, Y., & Xue, Z. (2024). Models, Simulations, and Applications of Small Satellite Thermal Analysis, *Advances in Space Research*, 74 (2), 836-860.

Sözbir, N., Bulut, M., Öktem, M.F., & Kahriman, A. (2008). *TUSAT haberleşme uydusunun ısıl tasarımı*, II. Ulusal Havacılık ve Uzay Konferansı, Istanbul, Türkiye, 15-17 October.

Sözbir, N., & Bulut, M. (2009). *Türksat haberleşme uydusunun ısıl kontrolü,* 17. Ulusal Isı Bilimi ve Tekniği Kongresi, Sivas, Türkiye, 24-27 June.

Sozbir, N., & Bulut, M. (2009). *Thermal Control of CM and SM Panels for Turkish Satellite*, SAE 39th International Conference on Environmental Systems, Savannah, Georgia, USA, 12-16 July.

Sozbir, N., Bulut, M., Oktem, M. F., Kahriman, A., & Chaix, A. (2008). *Design of Thermal Control Subsystem for TUSAT Telecommunication Satellite. World Academy of Science, Engineering and Technology International Journal of Computer and Systems Engineering, 2(7), 1370-1373.*

Şükran EFE

Atatürk University, Faculty of Engineering, Mechanical Engineering Erzurum, Türkiye.

Industrial Tea Waste and Energy Potential

Endüstriyel Çay Atığı ve Enerji Potansiyeli

ABSTRACT

Türkiye is ranked seventh in the world in tea cultivation and tea cultivation is carried out only in the cities of Rize, Trabzon, Artvin, Giresun and Ordu. The annual production amount of tea is 1.357 million tons and the highest cultivation rate is 67% in Rize City and the lowest is 2% in the Giresun-Ordu region. The tea plant harvested from the field is processed in state or private tea factories. The product obtained as a result of this process is defined as tea, and the remaining parts consisting of fiber, garbage and dust are defined as industrial tea waste (ITW). It is a big problem for both growers and tea operators due to the same harvest time of the tea plant in all cities, the high potential of tea cultivation in the region and the lack of suitable land structure for the disposal of ITW. Removing ITW from the factory environment during the production period and adding to the country's economy as an energy source is important in terms of sustainable energy.

In the study prepared with 2023 statistical data, the energy potential that can be obtained by directly burning ITW formed after tea production in factories was examined. As a result, it was found that 1.06e9 MJ of electrical energy and 1.06e9 MJ of thermal energy would be obtained annually if ITW in Türkiye were burned directly in the cogeneration system.

Keywords: Biomass energy, direct burning, energy potential, industrial tea waste.

ÖZ

Türkiye Çay yetiştiriciliği sıralamasında Dünyada yedinci sıradadır ve çay yetiştiriciliği sadece Rize, Trabzon, Artvin, Giresun ve Ordu şehirlerinde yapılmaktadır. Yıllık üretim miktarı 1.357 milyon ton olan çayın en yüksek yetiştiricilik %67 oranla Rize ilinde, en az da %2 ile Giresun-Ordu bölgesinde yapılmaktadır. Tarladan hasat edilen çay bitkisi devlet veya özel çay fabrikalarında işlenir. Bu proses sonucunda elde edilen ürün çay, geride kalan lif, çöp ve tozdan oluşan kısımlar da endüstriyel çay atığı (EÇA) olarak tanımlanmaktadır. Çay bitkisinin tüm illerde aynı hasat zamanına sahip olması, bölgede çay tarımı potansiyelinin yüksek olması ve EÇA'nın imha edilmesi için uygun arazi yapısının olmaması hem üreticiler hem de çay işletmecileri için büyük bir sorundur. Üretim döneminde EÇA'nin fabrika ortamından uzaklaştırılması ve enerji kaynağı olarak ülke ekonomisine kazandırılması sürdürülebilir enerji açısından önemlidir.

2023 istatistik verileri ile hazırlanan çalışmada, fabrikalarda çay üretimi sonrası oluşan EÇA'nın doğrudan yakılmasıyla elde edilebilecek enerji potansiyeli incelendi. Sonuç olarak, Türkiye'deki EÇA'nın doğrudan kojenerasyon sisteminde yakılması durumunda yılda 1,06e9 MJ elektrik enerjisi ve 1,06e9 MJ termal enerji elde edildiği bulundu.

Anahtar kelimeler: Biyokütle enerjisi, direk yakma, enerji potansiyeli, endüstriyel çay atığı.

Introduction

The most important effect of developing technology is undoubtedly the increasing living standards. The most obvious result of the growing population and rising living standards is the increasing energy consumption. The increase in energy consumption threatens the existence of societies due to environmental effects such as greenhouse gases and the decreasing amount of reserves. As a result, the condition of society's continuity is possible with the use of energy sources that do not harm the environment and do not have a reserve problem.

Today, instead of fossil-based non-renewable energy sources that have been actively used from the past to the present due to their high energy potential, the use of environmentally friendly and highly renewable energy sources is rapidly becoming widespread. The use of renewable energy sources varies according to the accessibility of countries to resources. While hydraulic, and solar energy are at the forefront among its renewable resources due to Türkiye's geographical structure, geothermal energy and biomass use are also available regionally.

The term biomass is most commonly defined as a substance obtained or produced from living beings and their waste. All plant and animal substances in nature are biomass. Domestic organic waste, agricultural waste, animal waste, city sewage waste, and industrial organic waste (beet pulp, tea waste, sunflower waste, etc.) are examples of biomass. It is possible to convert biomass resources into energy with three different main processes (Eryaşar, 2007)

1. Thermochemical processes: direct burning, gasification, pyrolysis and liquefaction,
2. Biochemical processes: anaerobic fermentation, alcohol fermentation,
3. Physicochemical: transesterification

It is possible to obtain energy from biomass resources by burning them directly or by converting them into a different form such as biofuel (biogas, biodiesel, bio-alcohols, etc.). Its waste resulting from agricultural and animal activities must be disposed of. Otherwise, it creates both visual and environmental problems. Biomass energy contributes to the environmental appearance and prevents harmful formations such as harmful insects, odors, and flies, as it allows waste to be used without waiting (Eryaşar, 2007).

Biomass energy, which has significant potential among renewable energy sources, is a continuous energy source, unlike the sun and wind. The advantages of biomass energy are that it is renewable, its energy and raw materials can be stored, waste harmful to the environment is converted into energy for the economy, it prevents external dependency on energy, and it creates employment in the regions where it is established. While organic wastes are converted into energy via biochemical and phytochemical processes that require high technology and professional system installations, biomass with weak or no microorganisms, such as tea waste, is converted into energy via thermochemical processes.

First cultivated in China and India, tea is a traditional beverage consumed by people of all ages, hot and cold, around the world. The fact that tea is dried allows it to be consumed in any season and at any time, making it a widespread beverage. Most of the production is carried out on the Asian continent, and 64% of the total area and 49% of the total production are in China (Erkal, 2023).

The harvested tea plant is exposed to the production phase. The product obtained as a result of the production process is tea, and the remaining is tea waste (Tiftik, 2016). Waste consists of discarded leaves, buds, and pruned stems (Debnath & Purkait, 2023). According to 2023 data, approximately 1,357 million tons of fresh tea are processed in Türkiye, and approximately 200 tons of this are released into the environment as industrial tea waste (ITW) (Ministry of Agriculture and Forestry, 2020). Due to the high potential of ITW, many studies have been conducted in the literature to prevent environmental pollution caused by ITW and to bring it into the economy.

Aşik and Kütük (2012) studied the effect of tea waste compost on germination and compared the results with farmyard manure and peat. They found that tea waste is more effective.

Boyraz et al. (2023) investigated whether tea wastes could be used in the production of activated carbon. The study showed that it could be produced by the hydrothermal method from tea facility wastes provided by Rize-ÇAYKUR facilities.

Müftüoğlu et al. (2009) searched the effect of tea waste on compost production time. The study found that using tea waste in composting shortened the compost production time.

Turumtay (2020) mixed tea waste with lignite coal in different proportions to use the energy of tea waste and examined the thermal capacities of the obtained mixtures.

This study aims to convert ITW generated after the production of tea grown in Türkiye into energy while disposing of it. The energy potential to be obtained from ITW was examined using 2023 tea statistics.

Tea Plant

The tea plant, known by its Latin name Camellia sinensis or Thea sinensis, belongs to the Theaceae family. This plant, which is a short shrub, grows in humid climates. China, India, Indonesia, Japan, and Taiwan have the highest production, and it is produced in 40 countries worldwide (Üstün & Demirci, 2013; Mammadow, 2024). It can be produced in regions where rainfall is more than 2000 mm and regular. While tea cultivation is carried out for 12 months in tropical and equatorial regions, it is only carried out for 6 months of the year in high-latitude countries such as Türkiye and Iran (Ministry of Agriculture and Forestry, 2020). According to the fermentation status of the tea plant, it is classified as green tea (unfermented), black tea (fermented) and oolong tea (semi-fermented) (Elmas & Gezer, 2019).

Tea leaves are harvested by using specific machinery or by hand. Black tea's quality highly relies on the physicochemical processes involved in its production, the timing of the harvest and the skills of the picker in selecting the most suitable leaves. Soon after tea leaves are plucked, they undergo various processing steps, including withering, rolling, fermentation, drying, classification, packaging and storage. Figure 1 shows steps in the manufacturing of tea leaves (Tiftik, 2016; Aaqil et al., 2023).
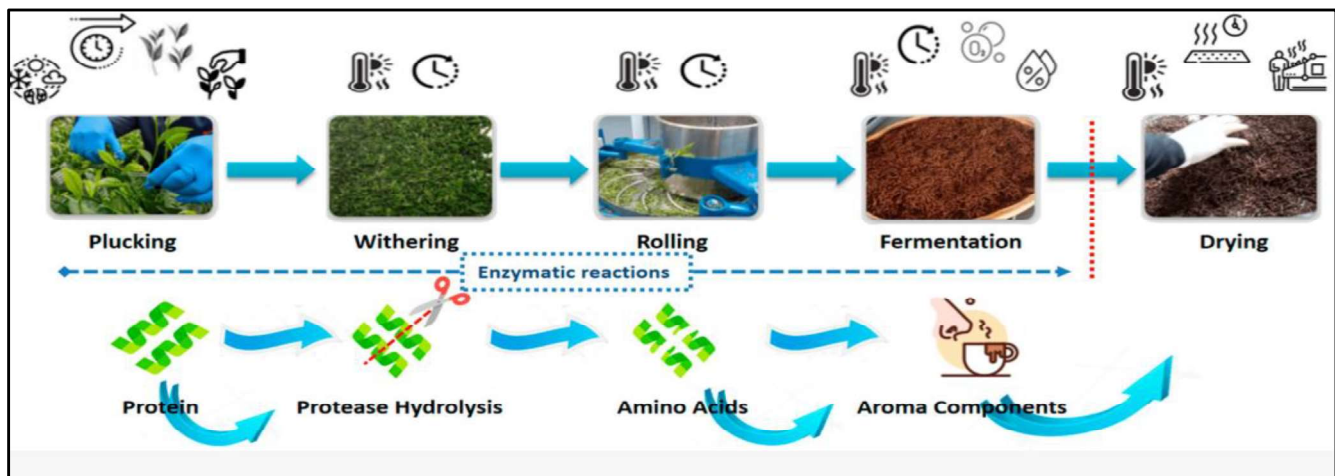
Figure 1.
Steps in the manufacturing of tea leaves.

Tea and Türkiye Potential

The first studies on tea cultivation in Türkiye were initiated in 1888 with the planting of seeds brought from China in the Bursa area. However, the Bursa studies did not yield positive results. In 1924, tea production studies were started in Rize and its surroundings, and when successful results were obtained, 20 tons of tea seeds were purchased and distributed to producers in 1937. In 1940, fresh tea leaves were processed to obtain dry tea, and in 1942, the import and domestic sale of tea were monopolized by the state. Due to the increasing tea production, the first tea factory with a capacity of 60 tons/day was opened in the Fener neighborhood of Rize in 1947. Tea enterprises, which were affiliated with the General Directorate of Tekel until 1971, were transferred to the General Directorate of Tea Institution and the title of the enterprise was changed to General Directorate of Tea Enterprises (ÇAYKUR) in 1984. In the same year, tea cultivation, production, processing and sale were freed in the markets. Today, tea production is carried out in more than 300 private enterprises other than ÇAYKUR (Üstün & Demirci, 2013).

Tea production in Türkiye is carried out in the Eastern Black Sea Region in the cities of Rize, Trabzon, Artvin, Giresun and Ordu. The teas grown are processed by ÇAYKUR Enterprises or private enterprises located in the same regions and added to the economy. According to 2023 data, approximately 1.357 million tons of fresh tea have been processed and this value is increasing day by day. The amount of fresh tea produced in Türkiye between 2000 and 2023 is presented in Table 1 and Figure 2 (TUİK, 2023).

In 2023, tea production was carried out on 791 decares, 67% of which was in Rize, 19% in Trabzon, 12% in Artvin and 2% in the Giresun-Ordu Region. Tea plantation areas and the number of tea producers are in Table 2. Distribution by province of the area reserved for tea plantations and of the number of tea producers is presented in Figure 3 and Figure 4, respectively (ÇAYKUR, 2023). Table 3 shows the amounts of fresh tea leaves between 2019 and 2023, and Figure 5 shows graphically the distribution according to province (Erkal, 2024).

According to the 2024 Tea Product Report published by the Turkish Ministry of Agriculture and Forestry, Türkiye has the highest efficiency value for the amount of tea produced per unit area, with 1,563 kgda^{-1}. Zimbabwe is in second place with 1,448 kgda^{-1}, and Malawi is in third place with 1,222 kgda^{-1}. In 2022, the efficient distribution of tea produced by the province is presented in Table 4 and Figure 6 (Erkal, 2024).

Table 1.
Tea production, 2000-2023

Year	Number of tea growers	Area reserved for tea plantation (Decare)	Production of green tea leaves (Tonnes)
2000	204491	767500	758038
2001	204112	766530	824946
2002	203028	766450	791700
2003	203318	766400	869000
2004	202431	766320	1105000
2005	202699	766250	1192004
2006	203431	766136	1121206
2007	203901	765808	1145321
2008	199231	758257	1100257
2009	200798	758513	1103340
2010	202494	758641	1305566
2011	205312	758895	1231141
2012	-	758566	1250000
2013	-	764255	1180000
2014	-	760494	1266311
2015	-	762073	1327934
2016	-	763609	1350000
2017	-	821079	1300000
2018	-	781334	1480534
2019	-	785693	1407448
2020	-	786813	1450556
2021	-	789001	1453964
2022	-	791285	1269546
2023	-	791984	1356556

Table 2.
Tea cultivation areas and the number of tea producers for 2023.

City	Area reserved for tea plantation (Decare)	Number of tea growers
Rize	530803	130399
Trabzon	152540	49322
Artvin	91929	19903
Giresun-Ordu	16712	7522
Total	791984	207146
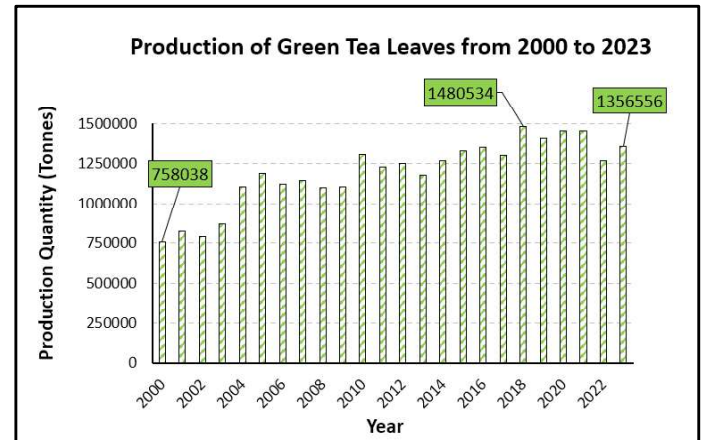
Figure 2.
Production of green tea leaves, 2000-2023
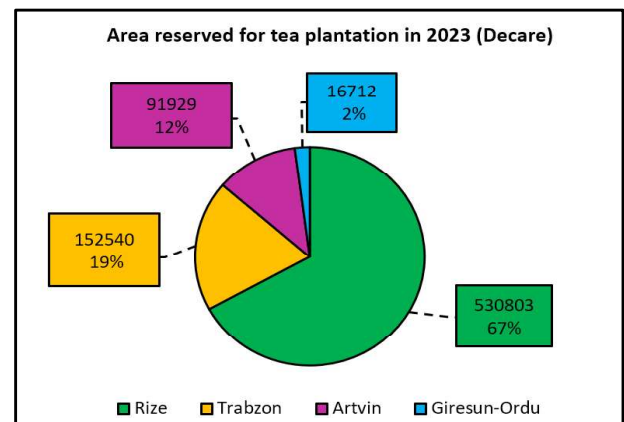
Figure 3.
Area reserved for tea plantation in 2023
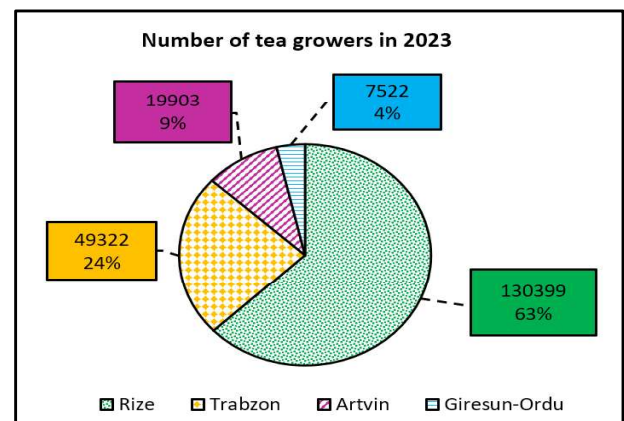
Figure 4.
Number of tea producers in 2023.

Table 3.
The amount of fresh tea leaves by province (Kilo Tonnes)

City	2019	2020	2021	2022	2023
Rize	906	934	935	821	872
Trabzon	325	333	328	287	306
Artvin	146	154	160	135	147
Giresun-Ordu	31	30	31	27	32
Total	**1408**	**1451**	**1454**	**1280**	**1357**
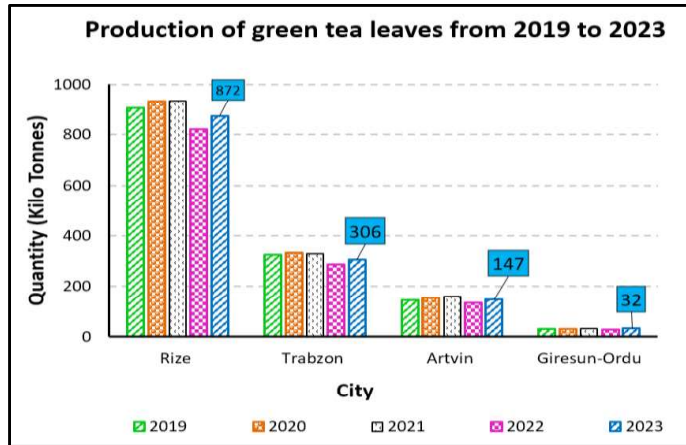
Figure 5.
The amount of fresh tea leaves by province from 2019 to 2023

Table 4.
Efficiency of tea produced from 2019 to 2023

City	2019	2020	2021	2022	2023
Trabzon	2.163	2.206	2.167	1.884	2.006
Giresun	1.880	1.825	1.861	1.634	1.899
Rize	1.716	1.769	1.767	1.547	1.643
Artvin	1.599	1.683	1.743	1.470	1.594
Ordu	0.621	0.552	0.567	0.478	0.478
Türkiye	1.791	1.844	1.843	1.604	1.713
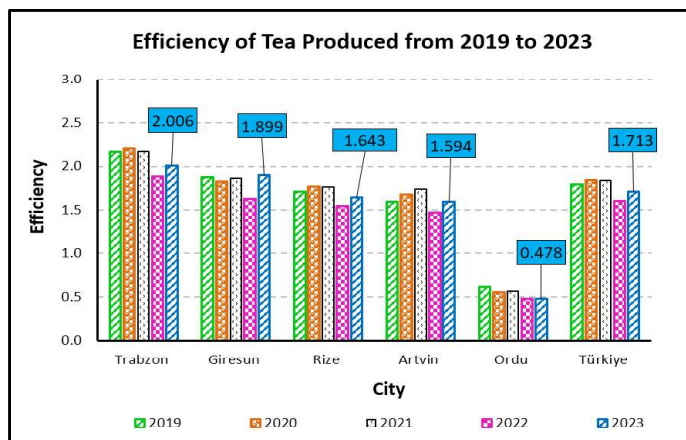
Figure 6.
Efficiency of tea produced from 2019 to 2023

Tea Losses
During the tea production phase, losses are caused during both production and consumption. Production losses in this study are named as ITW. Table 5 presents the losses of tea.

Table 5.
Tea losses

Year	Harvest (Tonnes)	Losses (Tonnes)			
		ITW	Cons.	Total	%
2019	1407448	211117	37577	248694	17.6699
2020	1450556	217583	39311	256894	17.7100
2021	1453964	218095	37880	255975	17.6053
2022	1269546	190432	33072	223504	17.6051
2023	1356556	203483*	35338*	238821*	17.6050*

* Approximately values accepted

Loss values are determined annually from June to May of the following year. Since the loss data for 2023 had not yet been created when the study was prepared, the 2023 loss values were estimated based on the loss values for 2022 and 2021.

Energy Production from Industrial Tea Wastes
The energy released as a result of the burning of organic compounds is called by different names as thermal energy and calorific value. The amount of energy is calculated with Equ. 1.

$$Q = m.H \qquad (1)$$

here Q, m and H show thermal energy, the mass of ITWs and heat value of ITW, respectively. In the study, the heat value of ITW was accepted as 17.45 MJkg^{-1} using Table 6.

Table 6.
The heat/calorific value of ITW in some studies in the literature

References	Heat Value
(Haque et al., 2024)	19.48 MJkg^{-1}
(Nagaraja et al., 2013)	16.19 MJkg^{-1}
(Pua et al., 2020)	17.393 MJkg^{-1}
(Turumtay, 2020)	4000 kcalkg^{-1} (16.747 MJkg-1)
Mean (accepted)	17.45 MJkg^{-1}

Today, combined heat and power (CHP) systems, also known as cogeneration, are used for the production of electrical energy from thermal energy because they increase the unit efficiency by using the residual heat. The efficiency schema of the CHP system is in Figure 7 (Fuentes-Cortés et al., 2015).
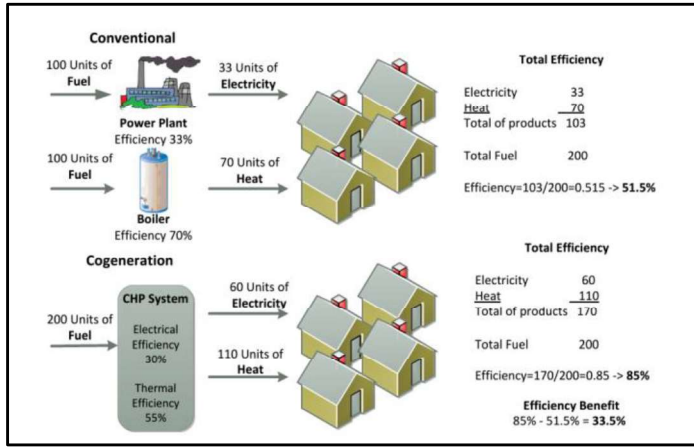
Figure 7.
Conventional systems and CHP systems

According to 2023 statistics, if 203483 tons of ITWs from the originated 1356556 tea plants are directly burned, 3550811664 MJ of thermal energy is produced. Suppose the thermal energy is converted via the CHP to electricity and thermal energy, 1065243499 MJ of electricity energy and 1952946415 MJ of thermal energy form. Production and transformation values of energy are shown in Table 7.

Table 7.
Production and transformation values of energy

Annually obtained from harvest	Tea (Tonnes)	1356556
	Waste (Tonnes)	203483
	Thermal energy (MJ)	3550811664
Annually required energy for residences	Electricity (kWh)	5500
	Heating system (MJ)	38058
	Hot water (MJ)	6280
CHF efficiency	Electricity (%)	30
	Thermal (%)	55
Produced energy from CHP	Electricity (MJ)	1065243499
	Thermal (MJ)	1952946415

Using the electricity and thermal energy produced in CHP is possible in residences. So, it is necessary to transport the ITW to a CHP system, where it must be converted into electricity and thermal energy and then distributed to residences. Considering the annual energy consumption of a 100 m^2 house and family of 4, it is possible to provide the electricity needs of approximately 40 thousand residences and the thermal needs of roughly 20 thousand residences.

Conclusion

Türkiye ranks seventh in the world's tea producers ranking, with more than 1 million tons of tea plants grown annually. After harvesting, the tea plant is processed in factories for tea production, and as a result of this process, a large amount of industrial tea waste is generated. The removal and disposal of İTW from the factory environment creates additional costs for factories.

The study prepared using 2023 Türkiye statistical data examined the disposal of ITW without harming the environment and the generation of energy by burning ITWs. When 203483 tons of ITW formed after tea production is directly burned, 3550811664 MJ of thermal energy is produced. It is possible to convert this energy into 1065243499 MJ of electrical energy and 1952946415 MJ of thermal energy via CHP.

Production electricity and thermal energy can be used in residences. if the energy is used in residences, it will reduce the unit efficiency of the obtained energy from ITW due to transportation costs and distribution losses. While losses in electrical energy are expected to be around 15%, thermal losses are expected to be around 50%. Therefore, processing the ITW by the factories where it is produced will increase the efficiency of the energy to be obtained from

There are two important results of doing the energy conversion process in the factories where the ITW is obtained.

1. It eliminates the negative environmental effects, as it will allow the ITW to be disposed of immediately.
2. It prevents additional losses, such as the transportation of the ITW to a different location and the transfer of the produced energy.

The advantages of converting ITW into energy in factories are listed below.

1. The electrical energy produced can be used for the electricity needs of the factory.
2. The thermal energy produced can be used in the drying process of the tea plant.
3. Since the ITW produced will be processed in the same factory, there is no need for a waste collection area.
4. Since the ITW will not be transferred to another location, the use of fossil fuels due to transportation is prevented.

References

Aaqil, M., Peng, C., Kamal, A., Nawaz, T., Zhang, F., & Gong, J. (2023). Tea Harvesting and Processing Techniques and Its Effect on Phytochemical Profile and Final Quality of Black Tea: A

Review. *Foods*, *12*(24), 1–28. https://doi.org/10.3390/foods12244467

ÇAYKUR. (2023). *Çaykur Activity Report* (Issue I). https://www.caykur.gov.tr/Pages/Yayinlar/YayinDetay.aspx?ItemType=2&ItemId=1001

Debnath, B., & Purkait, M. K. (2023). *Sustainable Utilization of Tea Waste*. https://doi.org/10.1007/978-981-19-8774-8_11

Elmas, C., & Gezer, C. (2019). Composition and Health Effect of Tea Plant (Camellia sinensis) Tea. *Akademik Gıda*, *17*(3), 417–428. https://doi.org/10.24323/AKADEMIK-GIDA.647733

Erkal, H. (2023). Tea Product Report 2023. In *T.C. Tarım ve Orman Bakanlığı Tarım Reformu Genel Müdürlüğü Tarımsal Ekonomi ve Politika Geliştirme Enstitüsü*. chrome-extension://efaidnbmnnnibpcajpcglclefindmkaj/https://arastirma.tarimorman.gov.tr/tepge/Belgeler/PDF Ürün Raporları/2023 Ürün Raporları/Çay Ürün Raporu 2023-383 TEPGE.pdf

Erkal, H. (2024). Tea Product Report 2024. In *T.C. Tarım ve Orman Bakanlığı Tarım Reformu Genel Müdürlüğü Tarımsal Ekonomi ve Politika Geliştirme Enstitüsü*. chrome-extension://efaidnbmnnnibpcajpcglclefindmkaj/https://arastirma.tarimorman.gov.tr/tepge/Belgeler/PDF Ürün Raporları/2024 Ürün Raporları/Çay Ürün Raporu 2024-397 TEPGE.pdf

Eryaşar, A. (2007). *Design, Manufacture, Trial Run and Investigation of Parameters Impacting Its Performance of A Biogas System for Rural Use*. Ege Üniversitesi.

Fuentes-Cortés, L. F., Ávila-Hernández, A., Serna-González, M., & Ponce-Ortega, J. M. (2015). Optimal design of CHP systems for housing complexes involving weather and electric market variations. *Applied Thermal Engineering*, *90*, 895–906. https://doi.org/10.1016/j.applthermaleng.2015.07.074

Haque, M., Bora, P., Phukan, M. M., & Borah, T. (2024). Bioenergy generation and value addition from processing plant-generated industrial tea waste: a thermochemical approach. *Biomass Conversion and Biorefinery*, *14*(18), 22779–22790. https://doi.org/10.1007/s13399-023-04345-z

Mammadow, T. (2024). *Importance And Role of Tea Plant (Camellia Sinensis L.) In Agriculture of Azerbaijan And Türkiye*. Bursa Uludağ Üniversitesi Fen Bilimleri Enstitüsü.

Ministry of Agriculture and Forestry. (2020). Tea Evaluation Report. In *Tarım ve Orman Bakanlığı*. https://www.tarimorman.gov.tr/BUGEM/Belgeler/MİLLİ TARIM/Ürün Masaları Ürün Değerlendirme Raporları yayımlandı/Çay Değerlendirme Raporu.pdf

Nagaraja, M., Sundaresan, R., Natarajan, R., & Srinivas, T. (2013). Energy and Byproducts Recovery from Tea Waste. *International Journal of Electrical Energy*, *1*(1), 49–54. https://doi.org/10.12720/ijoee.1.1.49-54

Pua, F. L., Subari, M. S., Ean, L. W., & Krishnan, S. G. (2020). Characterization of biomass fuel pellets made from Malaysia tea waste and oil palm empty fruit bunch. *Materials Today: Proceedings*, *31*, 187–190. https://doi.org/10.1016/j.matpr.2020.02.218

Tiftik, B. E. (2016). *Pyrolysis of Tea Factory Wastes and Investigation Of Pyrolysis Products*. Ankara Üniversitesi.

TUİK. (2023). *Tea Production, 1988-2023*. Türkiye İstatistik Kurumu. https://data.tuik.gov.tr/Bulten/DownloadIstatistikselTablo?p=xXzRPL3HAjQJsLDQq9gQtYAgMlktgR/50H1xAjJ/eRg0H1HrYZGHBfyBINynlDbG

Turumtay, H. (2020). Investigation of combustion potential of tea pruning waste biomass mixed with lignite coal. *Artvin Çoruh Üniversitesi Orman Fakültesi Dergisi*, *21*(2), 135–142. https://doi.org/10.17474/artvinofd.655079

Üstün, Ç., & Demirci, N. (2013). Composition and Health Effect of Tea Plant (Camellia sinensis) Tea. *Mersin Üniversitesi Tıp Fakültesi Lokman Hekim Tıp Tarihi ve Folklorik Tıp Dergisi*, *3*(3), 5–12. https://dergipark.org.tr/mutftd/issue/43194/523880

ATATÜRK
ÜNİVERSİTESİ
YAYINLARI
ATATURK
UNIVERSITY
PUBLICATIONS

Mansur MUSTAFAOĞLU (iD)
Muhammet Kaan YEŞİLYURT (iD)
Muhammed Taha TOPCU (iD)
İlhan Volkan ÖNER (iD)
Kadir BİLEN (iD)

Atatürk University, Faculty of
Engineering, Mechanical Engineering
Erzurum, Türkiye .

Research on Heat Transfer of Nanofluid in Porous Media: A Mini Review

Gözenekli Ortamda Nanoakışkanın Isı Transferinin Araştırılması: Mini
Derleme

ABSTRACT

In this article, the recent developments in the literature on the application of heat transfer of nanofluids used in porous materials are examined. By analysing the articles published between 1998-2024, it is aimed to facilitate the researchers working in this field in their studies in this field. In this context, different analytical methods are used to describe flow and heat transfer in different porous media. In addition, various methods used in the modelling of nanofluids are described in detail. Here, analytical methods and forced convection heat transfer in porous media are discussed. In various studies in the literature, it is stated that a change in the height of the solid and porous media causes a change in the flow regime inside the pore cell. However, the effect of Darcy number (permeability value) as a dimensionless number in heat transfer varies. In this context, the statistical results obtained from the investigations examined in relation to the representation of various parameters such as the type of nanofluid and the geometry of the flow region are compared and it is thought to give an idea for future studies.

Keywords: Nanofluid, porous media, forced heat transfer, migration of nanoparticles, volume fraction.

ÖZ

 Bu makalede gözenekli malzemelerde kullanılan nanoakışkanların ısı transferi uygulanmasındaki literatürde yer alan son gelişmeleri incelenmiştir. 1998-2024 yılları arasında yayınlanan makaleler incelenerek bu alanda çalışan araştırmacılara bu alana yönelik çalışmalarında kolaylık sağlaması hedeflenmiştir. Bu kapsamda farklı gözenekli ortamlarda akışı ve ısı transferini tanımlamak için farklı analitik yöntemler kullanılmaktadır. Bununla beraber nanoakışkanların modellenmesinde kullanılan çeşitli metodlar ayrıntılı olarak anlatılmıştır. Burada gözenekli ortamda analitik yöntemler ve zorlanmış taşınımla ısı transferi konusu ele alınmıştır. Literatürdeki çeşitli çalışmalarda, katı ve gözenekli ortamın yüksekliğindeki bir değişiklik, gözenek hücresi içindeki akış rejiminde bir değişikliğe sebep olduğu ifade edilmektedir. Bununla beraber ısı transferinde boyutsuz bir sayı olarak Darcy sayısının (geçirgenlik değeri) etkisi değişiklik göstermektedir. Bu bağlamda nanoakışkanın türü ve akış bölgesinin geometrisi gibi çeşitli parametrelerin gösterimi ile ilgili olarak incelenen araştırmalardan elde edilen istatistiksel sonuçlar karşılaştırılarak ileriye dönük çalışmalara fikir vermesi düşünülmüştür.

Anahtar Kelimeler: Nanoakışkan, gözenekli ortam, zorlanmış ısı transferi, nanopartiküllerin göçü, hacim kesri.

Introduction

Nanofluids are the type of fluid used in heat transfer processes in many fields and where different particles are preferred. Here, various particles of different nanosize (Al_2O_3, CuO, SiC, etc.) are

used. The thermal conductivity of nano fluids varies according to the amount of concentration.

This situation has been evaluated by many researchers in the literature through various media and particles. In the researches, the heat conducting capacities and concentration values of different nano particles in the solution they formed with water were compared. This study investigated the experimental data of studies conducted by many researchers in recent years. In addition, the thermal conductivity enhancement coefficient was gathered from data found in the literature. The thermal conductivity improvement ratio is defined as the ratio of the thermal conductivity of the nanofluid to the thermal conductivity of the base fluid. According to the researchers' findings, eight parameters are effective in improving the thermal conductivity of nanofluids, and the laboratory results include the following: volume percent or particle concentration (Choi, 2002) particle material type (Keblinski et al. 2005) particle size (Putra et al. 2003) particle shape (Eastman et al. 2001) base fluid material type (Das et al. 2003) temperature (Pak & Cho, 1998), additives (Yu et al. 2008), acid strength (Wang et al. 1999). Each of these parameters is examined individually for data behavior, size, and stabilization through multiple tests. Heat exchangers, thermal storage, geothermal systems, and drying methods are just a few of the industrial and engineering domains where the study of heat transfer qualities in porous media is of great interest. One passive way to enhance heat transfer in a mechanical system is to incorporate a porous substance into it. In actuality, the inclusion of a porous material modifies the flow pattern and raises the system's overall thermal conductivity (Whitaker, 1986; Murshed et al. 2008; Meng & Yang, 2019; Boccardo, 2020; Ling et al. 2021; Gundogdu, 2023; Mustafaoğlu, 2023; Zhang et al. 2024). Nanofluids and porous materials are of great importance in enhancing heat transfer, and considerable research has been conducted to study the thermal properties of nanofluid flow in porous media. This paper provides a comprehensive summary of the latest research on this topic. The authors have surveyed their work from 1998 to 2024, given the large number of papers published since the last review article and their analytical complexity. The work is organized by fluid flow, heat transfer models, and applications of nanofluids in porous media.

Materials and Methods

The most important parameter in nanofluid models is the calculation of the volume occupied by the nanoparticles in the whole mixture and the thermal conductivity value. The efficiency of the mixture can be evaluated by calculating the particle volume percentage. The effect of particle volume percentage is clear. Figure 1 shows the effect of volume

percentage or particle concentration on increasing the thermal conductivity of the nanofluid. The figure shows the experimental work of a group of researchers for Al_2O_3 in water. The particle size and temperature of the nanofluid varied between the groups in Figure 1, however, the results were consistently close. Thermal conductivity increases as the particle volume ratio increases. There are usually 4-5% oxide particles in the nanofluid. The amount of nano particles in the fluid is considered the most optimum value in terms of viscosity and heat transfer (Figure 1)
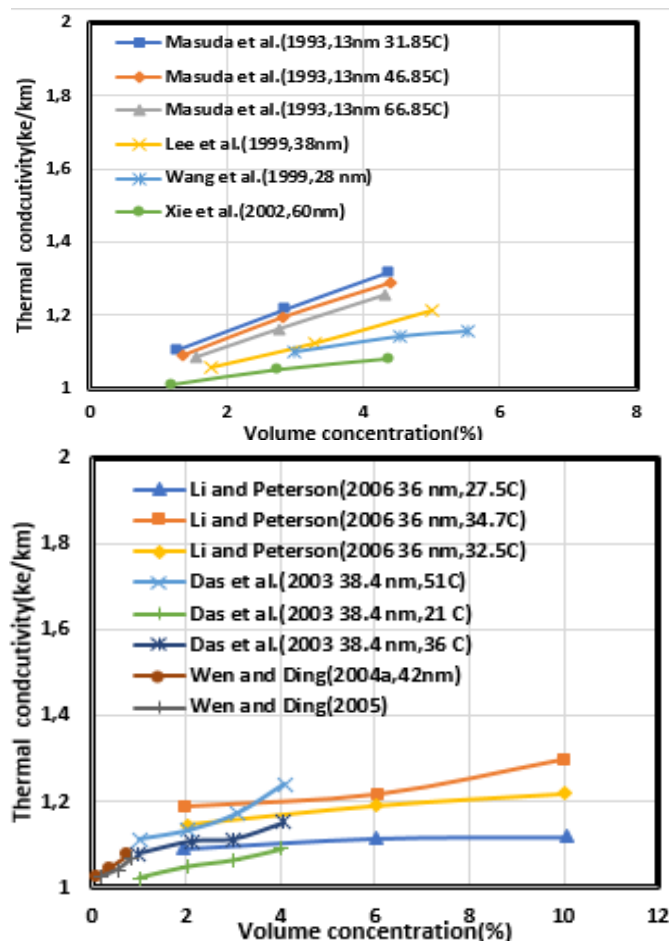
Figure 1.
Increasing the thermal conductivity of Al_2O_3 in water (Yu et al. 2008)

Particle volume percentage's effect on thermal conductivity is distinctly shown in Figure 1. The results of two groups using the same nominal particle sizes are presented for comparison. Figure 2 shows that the results are almost identical for the two groups using the same parameters. The increase in Figure 2 is relatively small due to the relatively small diameter of the particle. Figure 3 shows the results of other tests to increase the thermal conductivity of CuO in water. Figure 3 shows the particle size and fluid temperature ranges relative to Figure 1. Figure 4 shows a separate concentration parameter, using the particle size and fluid temperature. The overall behavior is identical to

Figures 1 to 4, and the values in Figures 3 and 4 were validated with two sets of experiments.
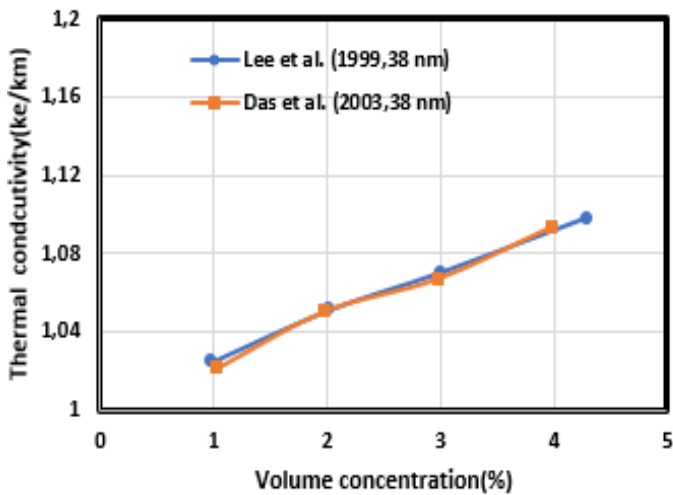
Figure 2.
Effect of particle concentration for Al₂O₃ in water (Yu et al. 2008)
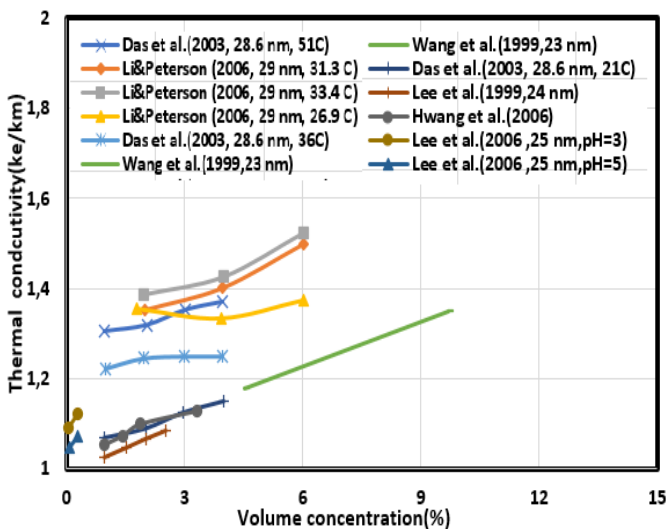
Figure 3.
Increasing the thermal conductivity of CuO in water (Yu et al. 2008)

properties. As shown, particle type has no significant effect on thermal conductivity in the low volume fraction.
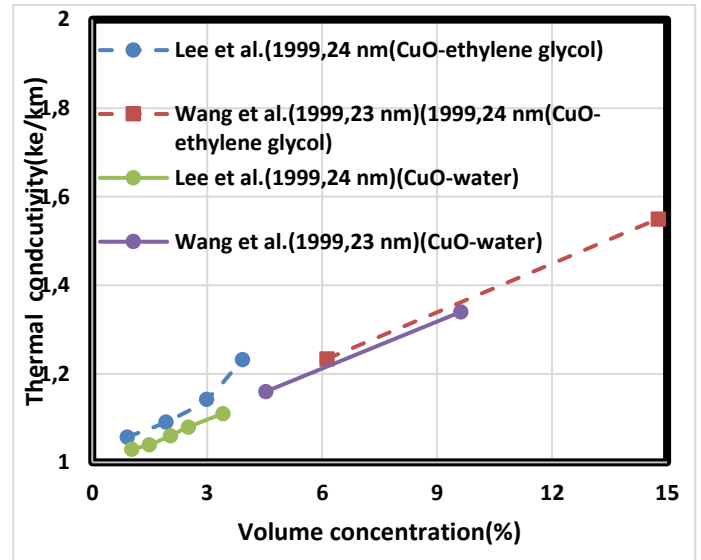
Figure 4.
Effect of particle concentration for thermal conductivity of CuO in water and CuO in ethylene glycol (Yu et al. 2008)
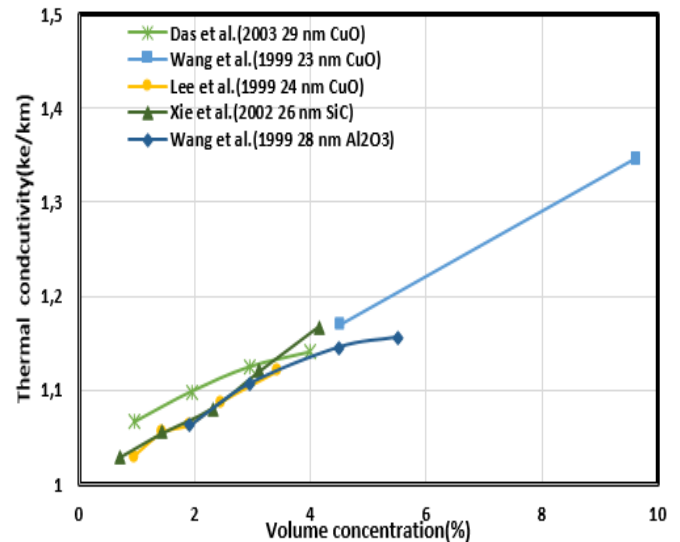
Figure 5.
Effect of particle type for particles in water (Yu et al. 2008)

Figure 4 clearly demonstrates the effect of the volume fraction of copper oxide nanofluid in ethylene glycol, which exhibits the same behavior as Figures 1 to 4. Additionally, the values obtained from the data of the two groups in Figure 5 are in excellent agreement. Figures 1 to 4 clearly demonstrate that the thermal conductivity increases with an increasing volume fraction. The influence of particle type on increasing silicon carbide oxide particle thermal conductivity in water is obviously shown in Figure 5. The remaining parameters, which are nearly constant in Figure 5, clearly demonstrate the impact of material

Figure 6.
Effect of particle type for particles in ethylene glycol (Yu et al. 2008)
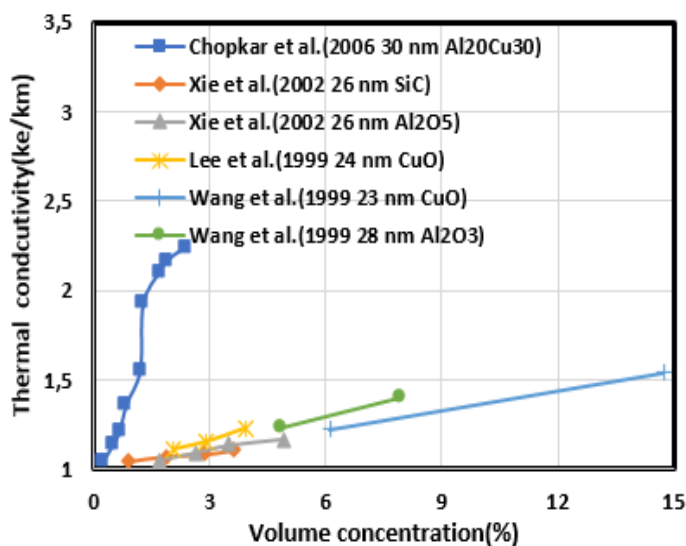
Figure 7.
Effect of particle type for particles in ethylene glycol (Yu et al. 2008)

The results of increasing the thermal conductivity are shown in Figure 6, which includes iron and copper oxide metal particles for comparison. As can be seen, the metal particles provided the same increase as the oxide particles at a much lower volume fraction. Figure 6 shows that the thermal conductivity coefficient of metal is higher than that of oxide particles. Therefore, the particle concentration for the highest level is included in the execution of the experiments. This can also be seen in Figure 7. The results of oxide particles, silicon carbides and metal particles at the same time. The size of the particles in Figure 7 is larger than the particles in Figure 6. However, the most significant effect seen is a large increase in the thermal

conductivity of the metal particle nanofluid when the volume percentage of metal particles increases to 2.5% compared to 0.7% in Figure 7.

At 2.5% volume percent of metal particles, the thermal conductivity of the nanofluid shown in Figure 7 is up to 115% higher than that of ethylene glycol. This result is significantly higher than the results for non-metallic particles in Figure 7 and points to the research and production areas of nanofluids. However, as mentioned before, the main disadvantage of nanofluids with metal particles is the oxidation process during production and use. The influence of the size of the spherical particles on the increase of thermal conductivity will be discussed later. Here the size parameter is the nominal diameter. The results for aluminum nanofluid with particle diameters from 28 to 60 nm are shown in Figure 8. For 38 nm particles, there is a similarity between the data from the two groups. The results indicate an improvement in heat conductivity for larger particles (60 nm, for example). According to these results, smaller particles are expected to show the least increase. However, the results for 28 nm particles are in between the two larger particles. The results in Figure 8 show similar results to those obtained for ethylene glycol. The case in Figures 8, apart from the results of Wang et al. (1999) results in larger diameter particles producing a greater increase in thermal conductivity. This result contradicts some theories that assume a uniform distribution of small particles even with the best manufacturing method.
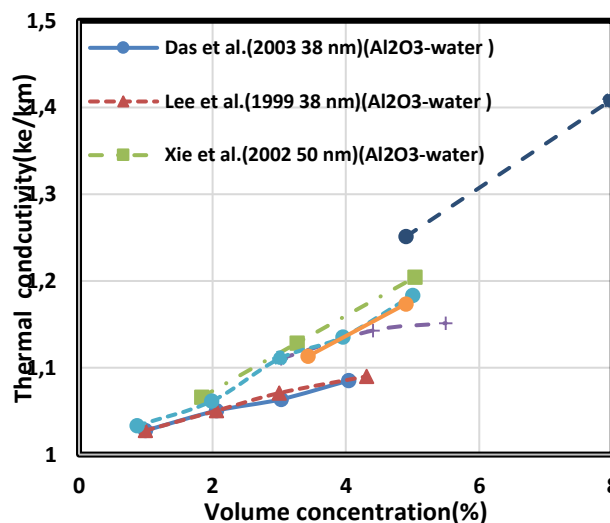
Figure 8.
Effect of particle size for Al_2O_3 in water and particle size for Al_2O_3 in ethylene glycol (Yu et al. 2008)
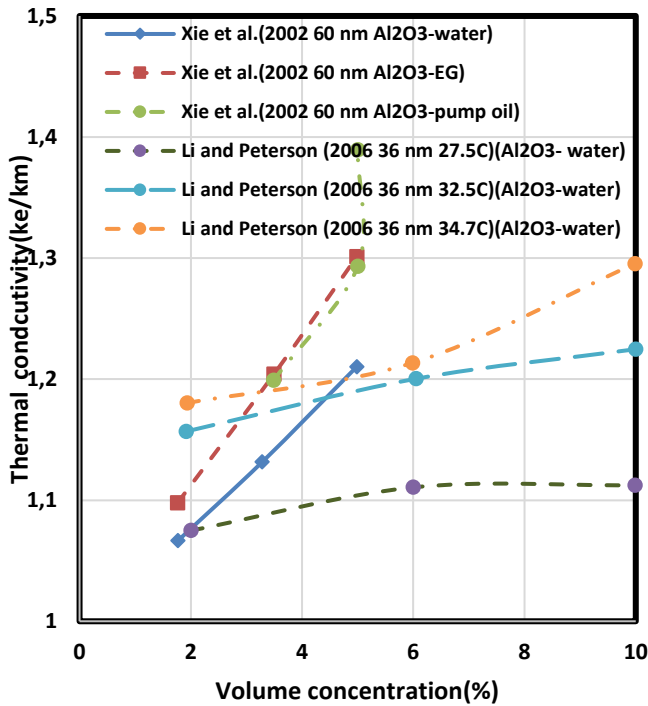
Figure 9.
Effect of particle size for CuO in water, SiC in water and particle shape for SiC in ethylene glycol (Yu et al. 2008)

The third comparison of the effect of particle size on the increase in thermal conductivity is shown in Figure 9 for CuO in water. The results of Figures 9 show that the increase in thermal conductivity does indeed increase with the diameter of the spherical nanometer particles. Figure 9 compares the effect of particle shape (spherical and cylindrical). Cylindrical particles show an increase in thermal conductivity; this result appears to be due to the network of elongated particles conducting heat from the fluid. All of the results in Figures 9 through 10 show that elongated particles are better than spherical particles at increasing thermal conductivity. This result points to other areas for nanofluid research and production, although spherical particles are generally available at more reasonable prices.
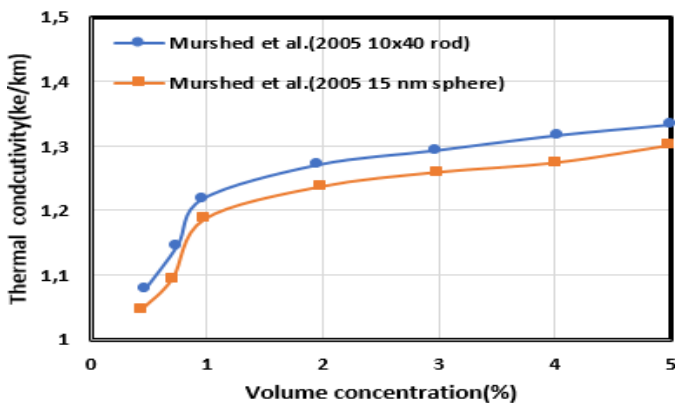
Figure 10.
Effect of particle shape for TiO$_2$ in water

The effect of the base fluid (such as water, ethylene glycol, and pump oil) on increasing the thermal conductivity of the nanofluids is shown in Figure 11. The results show that the thermal conductivity increases in fluids that are poor in heat transfer. Water is the best heat transfer fluid with the maximum thermal conductivity when compared to other fluids, and the results in Figure 11 demonstrate the least rise in water.
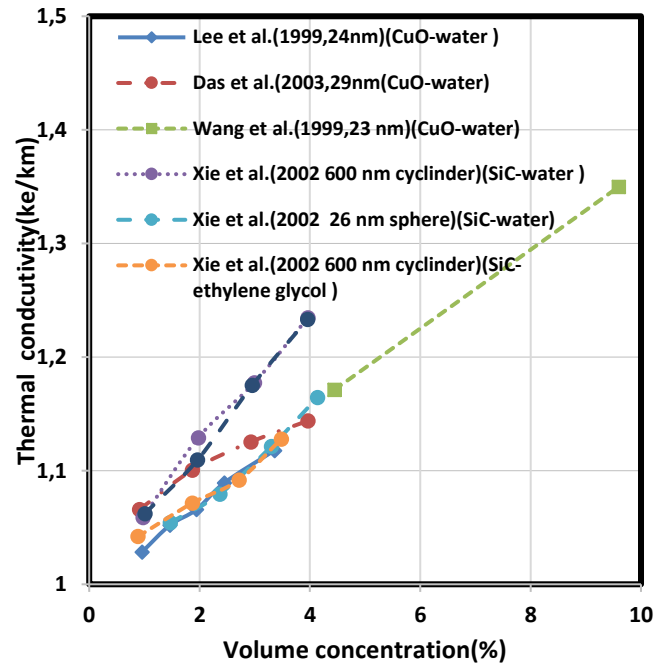
Figure 11.
Effect of base fluid type and for Al$_2$O$_3$ in water (Yu et al. 2008)

The thermal conductivity is usually more sensitive to temperature than the bulk liquid. Wang et al. (2003) presented nanofluid data for Al$_2$O$_3$ in water and CuO in water over a small temperature range. The authors proposed that the motion of the nanoparticles is responsible for the considerable temperature dependency of the thermal conductivity of the nanofluid. Figures 11 through 12 display the Al$_2$O$_3$ in water results for each of the three groups. While the fluid temperatures and particle sizes vary throughout the figures, the temperature and particle size remain consistent across all figures. Only the results of Masuda et al. (1993) deviate from the general behavior. The increase in thermal conductivity of CuO in water is shown in Figures 13 two groups of researchers. The data show that the thermal conductivity increases with increasing temperature. Similar results were obtained from the two laboratory values for multi-walled carbon nanotubes in water, as shown in Figures 14. Although the behavior of some data is not consistent with the general temperature behavior, it should be noted that this does not mean that the self-test is completely inaccurate. The inconsistent temperature behavior was reported by Masuda et al. (1993) for SiO$_2$. However, the results

for TiO2 in water were not the same with respect to temperature. Anyway, considering all the results, we see that the general proof of the general temperature behavior has been made. This behavior is essential for heat transfer applications in the transportation industry, where fluids operate at high temperatures.
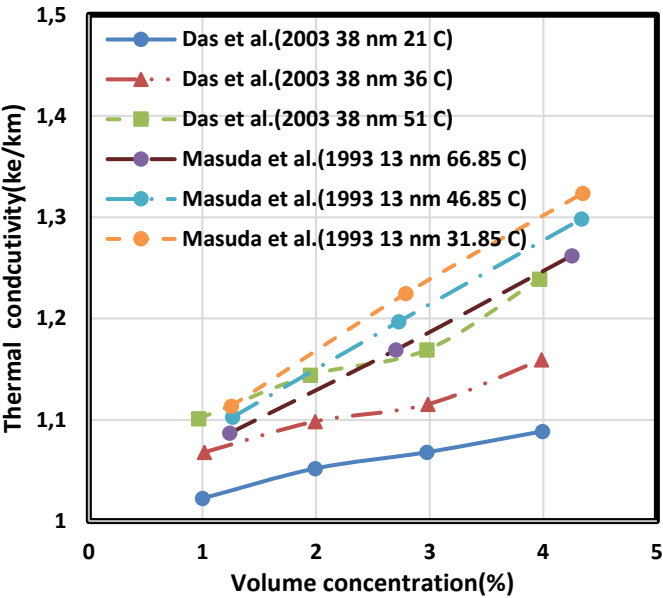
Figure 12.
Effect of temperature for Al₂O₃ in water (Yu et al. 2008)
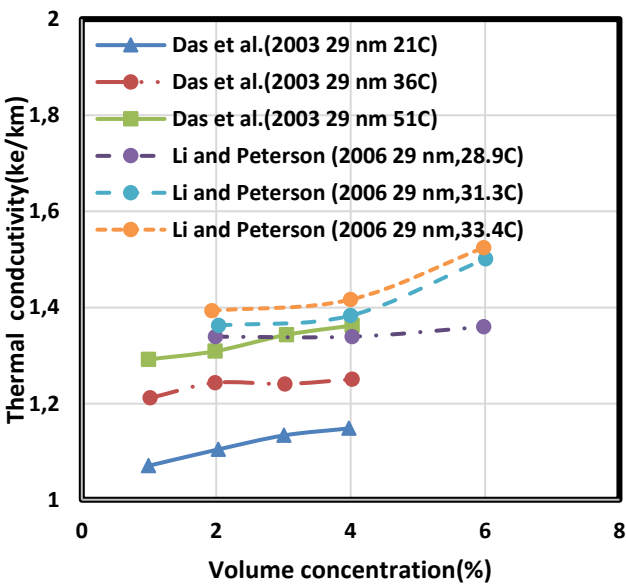
Figure 13.
Effect of temperature on CuO water (Yu et al. 2008)
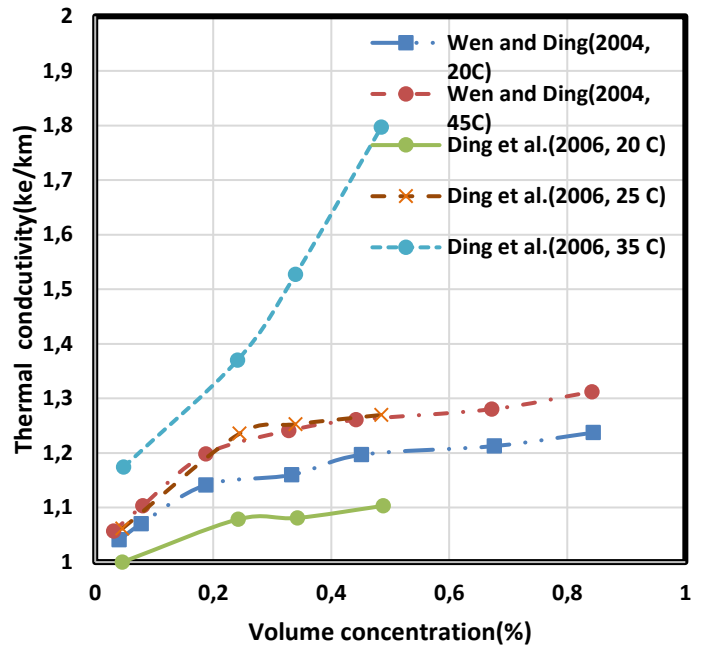
Figure 14.
Effect of temperature for multi-walled carbon nanotubes in water (Yu et al. 2008)
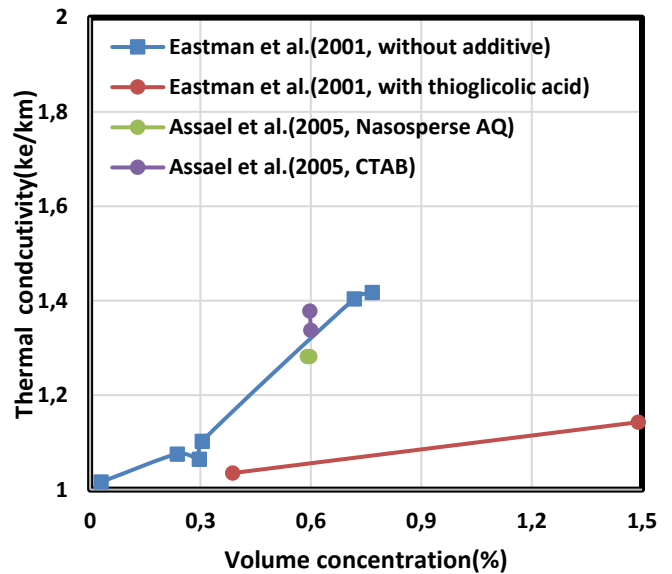
Figure 15.
Addition effect of copper in ethylene glycol and multi-walled carbon nanotubes in water (Yu et al. 2008)

Researchers use additives to keep nanoparticles in solution and prevent them from agglomerating. A review of previous studies shows that there has been a wide range of results depending on the type of additive, concentration and other factors. However, most studies involving additives show an increase in thermal conductivity. Data from two sets of studies for nanofluids with different additives are shown in Figures 15, in both cases the

improvement in thermal conductivity increases with the use of additives. In addition, very few studies have been published on the effect of the acid strength of the fluid on improving the thermal conductivity of nanofluids, and the results of the two groups are presented separately below. The results of Figure 16 show the same behavior for different particles in water.
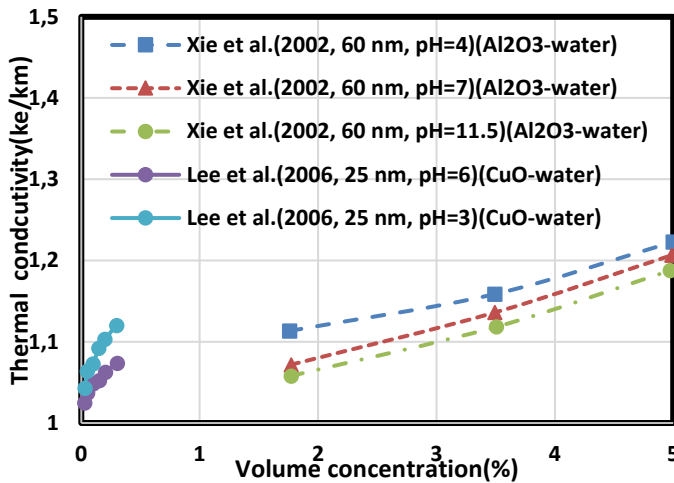
Figure 16.
Effect of acid strength for Al_2O_3 in water and CuO in water (Yu et al. 2008)

Convection Heat Transfer of Nanofluids in Porous Media

As for experimental research, Eastman (1999) conducted an experiment for copper oxide in water. He tested the turbulent flow regime in a nanofluid tube with a volume fraction of 0.9%. The test result shows a 15% increase in heat transfer for nanofluids compared to the base fluid. Wen and Ding (2004) conducted several experiments with aluminum oxide-water nanofluid flowing in a slow-flowing copper tube. In this context, the penetration of nanoparticles into the base fluid shows an increase in the displacement heat transfer coefficient. As the concentration of nanoparticles increases, the heat transfer coefficient also increases. Heris et al. (2006) conducted their experiments with alumina nanofluid in copper water in water in a tube with slow flow and constant wall temperature. In another experiment conducted by Heris et al. (2007) the heat transfer of alumina in water with volume fraction from 0.2% to 2.5% and Reynolds number from 2050 to 7000 was tested in a constant temperature tube. It shows that the Nusselt number increases with increasing volume fraction and Reynolds number. Lai et al. (2006) investigated alumina nanofluid in water in a stainless steel tube (the tube was made in mm) with a constant heat flow of Reynolds number less than 270. The results showed that for a volume fraction of 1%, the heat transfer increased by 8%. Jung et al. (2006) investigated alumina nanofluid in water in a rectangular microchannel with laminar flow and presented a

new relationship for the heat transfer of nanofluids in microchannels. Rea et al. (2008) investigated the displacement heat transfer in fully developed turbulent flow with alumina in water and zirconia in water and found good agreement with the presented single-phase relations. Xuan and Li (2003) performed an experiment with copper nanofluid in water flowing in a tube in a turbulent regime with a Reynolds number between 10,000 and 25,000 and a volume fraction of 0.3 to 2% and reported a significant increase in heat transfer. In another study, Li and Xuan (2004) reported a 39% increase in Nusselt number for 2% by volume of copper nanoparticles in water. Zhou (2004) studied copper-acetone heat transfer for 80 to 100 nm particles and 0 to 4 gL^{-1} concentration. Li et al. (2005) studied copper-water heat transfer for 26 nm nanoparticles at 0.5 to 2% by volume and reported the heat transfer ratio of nanofluid to base fluid to be 1.6 to 1.39. Faulkner et al. (2004) investigated the heat transfer of carbon nanotubes in water and microchannels with a hydraulic diameter of 335 micrometers and volume fractions of 1.1, 2.2, and 4.4%. The results showed that increasing the volume fraction increased the heat transfer coefficient. Yang et al. (2005) also performed an experiment with graphite nanoparticles fully dispersed in water. The test was performed inside the tube and showed a 22% increase in heat transfer. Ding et al. (2006) have found a 350% increase for multi-walled carbon nanotubes at Reynolds 800. Duangthongsuk and Wongwises (2008) reported an increase in heat transfer for 0.2% titanium oxide and noted that the heat transfer coefficient is highly dependent on the measurement and calibration system. Jang and Choi (2004) reported an 8% increase in heat transfer for 0.3% alumina in water. Duangthongsuk and Wongwises (2009) estimated an 11.6% increase in displacement heat transfer for 2% titanium oxide volume fraction in water and concentric tube heat exchangers.

Theoretical Investigations of Nanoflows in Porous Media

Nanofluids in porous media can be analyzed theoretically by creating different models in the computer environment. In this context, nanofluidscan be modeled in two ways as single-phase and two-phase. In the single-phase method, nanofluids are assumed to be continuous and continuity equations are solved accordingly. In this method, the particles are assumed to be uniformly distributed throughout the fluid and the fluid does not disturb the uniform distribution of the nanoparticles. In this method, continuity equations, momentum, and energy are solved for the base fluid to model the heat transfer of the nanofluids, but the viscosity and conductive heat transfer coefficient of the nanofluids replace the physical properties of the base fluid. One of the advantages of the single-phase method is that it is much simpler and more computationally efficient than the two-phase method. The two-phase method

solves three continuity, momentum and energy equations for the base fluid and one continuity equation for the nanoparticles and gives a much more accurate answer. Here Eastman et al. (2001) first used the single-phase method for modeling nanofluid heat transfer. In another study, Xuan and Roetzel (2000) found that the enhancement of heat transfer in nanofluids is influenced by two factors: high conductivity coefficient and thermal dispersion of nanoparticles. Khanafer et al. (2003) studied the performance of nanofluid in heat transfer compared to the base fluid in vacuum. In this research, the conductivity coefficient is a combination of conductivity coefficients, displacement and scattering effects. Buongiorno (2006) discussed seven motion mechanisms for nanofluids in his study and revealed two mechanisms as the dominant mechanisms for improving heat transfer through their investigations and dimensional analysis:

Brownian motion (random motion of nanoparticles caused by the continuous collision of nanoparticles with each other and with the base fluid molecules) and the effects of thermophoresis (motion of particles due to temperature gradient). The addition of these two mechanisms to the classical energy equation and the volume fraction equation is called the Bongiorno model. The Bongiorno model has become the basis for modeling nanofluid heat transfer by many researchers. Behzadmehr et al. (2007) modeled the heat transfer of copper-iron nanofluid for turbulent flow in a constant flow tube using a two-phase method. They obtained a 51% increase in heat transfer for a volume fraction of 1%. Maïga et al. (2004) used the single-phase approach to study the thermal and hydrodynamic characteristics of nanofluids moving in a tube under laminar and turbulent flow conditions. The results showed an increase in heat transfer when nanoparticles were injected into the base fluid. The researchers also found that alumina in ethylene glycol had better heat transfer than aluminum oxide in water. A study carried out by Roy et al. (2004) was comparable to the aforementioned research and yielded results that were analogous to those reported by Maïga et al. (2004). Sheikholeslami and Rokni (2017) employed two single-phase and two-phase methods to model nanofluids and investigated the movement of particles' effects on heat transfer. Their findings indicated that the Peclet number increases markedly with increasing nanoparticle size, and the influence of Brownian motion is particularly pronounced when the Peclet number is less than 10. Furthermore, they proposed an optimal nanoparticle size at which the enhancement in heat transfer is not accompanied by an equivalent increase in pressure drop. Kim et al. (2007) investigated the thermal transfer and stability of a double nanofluid comprising silver and copper nanoparticles. The findings indicated that the silver nanofluid exhibited a more pronounced enhancement in heat transfer

compared to the copper nanofluid. In examining the physical properties of nanofluids, Mansour et al. (2007) employed the modified Hamilton-Cruiser and Maxwell model for thermal and hydraulic coefficients in completely formed turbulent and laminar flow in a tube with continuous heat flux. Prakash and Giannelis (2007) conducted a study on copper nanofluid in ethylene glycol and reported that cylindrical nanoparticles exhibited superior heat transfer properties compared to their spherical counterparts. Heyhat and Kowsary (2010) conducted a numerical investigation into the effects of nanoparticle migration in a pipe with slow flow and constant heat flux, with a particular focus on the influence of Brownian motion and thermophoresis. In this research, the Bongiorno model was employed to model nanofluids and the migration effects of nanofluids. The findings indicate that the impact of nanoparticle migration on heat transfer is significant, with a notable enhancement in heat transfer observed compared to the single-phase method. The potential applications of microchannels include the cooling of electronic devices. Based on the properties of nanofluids, their use in liquid-based cooling systems has been proposed by researchers. Moreover, numerous researchers have recently employed the porous media approach and associated relationships to model the flow of nanofluids in microchannels. The modeling of the motion of nanofluids in microchannels is therefore of great importance in order to gain a deeper understanding of the concepts of nanofluid motion in porous media. This is evidenced by several researchers (Kim et al. 2001; Kim & Kuznetsov, 2003; Abbassi & Aghanajafi, 2006; Tsai & Chein, 2007; Ghazvini et al. 2009; Ghazvini & Shokouhmand, 2009).

Nanofluids are of significant value in numerous domains, with particular preference for use in the field of heat transfer across a range of scenarios. In this context, it is employed in the treatment of damaged tumors with temperatures above 43°C, with living tissues serving as an illustrative example of a fluid and porous environment. It is therefore imperative to gain a deeper understanding of the concepts of heat transfer and the movement of nanofluids in porous media.

In the field of research, publications by (Salloum et al. 2008; Salloum et al. 2009) have been made available. Kuznetsov and Nield (2010b) investigated the initial conditions of double penetration of nanofluid transfer and free heat transfer in the flow between two plates, utilizing the Bongiorno equations. The Darcy equation was employed to model the flow of nanofluids, with consideration given to the temperature equilibrium condition. The dimensionless equations were further analyzed to extract a set of dimensionless parameters, which were found to be identical to the dimensionless coefficients presented by Buongiorno (2006). However, in these coefficients, the

parameters associated with the porous medium were discernible. In a pioneering contribution, Kuznetsov and Nield (2011) articulated the three-temperature equation methodology for thermal instability in the context of the base fluid, nanoparticles and the solid phase of the porous medium. Research has been conducted into the temperature instability and free heat transfer of nanofluids in porous media. In this context, Kuznetsov and Nield (2010a) Kuznetsov and Nield (2010c) have published several research articles on this challenging topic. They undertook an investigation into the factors that contribute to the stability of nanofluids in porous media. In their seminal work, Nield and Kuznetsov (2009) first addressed the topic of heat transfer of nanofluids in porous media. The authors emphasized two key reasons for this investigation: firstly, to ascertain the stability of nanofluids in porous media and in contact with solids, and secondly, to ensure the accuracy of the governing equations.

1. Nanoparticles are defined as extremely small particles that remain suspended in nanofluids alongside the base fluid in porous media.
2. Nanoparticles dispersed in the base fluid together with surfactants demonstrate sufficient resistance to aggregation and precipitation in porous media. Furthermore, the low volume fraction of the nanofluid mitigates concerns about the deposition of nanoparticles.

In recent years, numerous researchers have employed the use of EI in order to model the phenomenon of heat transfer. However, in comparison to the utilization of two-phase methods (including Brownian terms and thermophoresis) from the single-phase model to the current reports, the employment of two-phase methods in the context of nanofluids in porous media (Tham & Nazar, 2012; Rosca et al. 2012; Mahdi et al. 2015; Sheikholeslami & Ganji, 2016) and two-phase (Sun & Pop, 2011; Rashad et al. 2013; Kasaeian, 2017; Xu et al. 2019) is more prevalent. The paper presented by Nield and Kuznetsov (2014) offers a logical and more realistic approach to the physics of the problem, particularly in the context of forced displacement heat transfer of nanofluids in porous media.

1. An enhanced flow that is slow and incompressible
2. No chemical reaction
3. Absence of external force
4. Dilute solution ($\varphi \ll 1$)
5. No radiation heat transfer

A porous medium is a network or solid matrix with interconnected holes; under normal conditions the matrix is assumed to be solid or rigid or undergo very small deformations.

The connection and interconnectedness of the holes allows the fluid to flow.

Porous Media Analysis Methods

The microscopic method is employed in order to gain insight into the distribution of holes according to shape and size, as well as the flow quantities, in porous media such as sandstone, limestone, sand, wood, bread, human skin, and so forth. In porous media such as sandstone, limestone, sand, wood, bread, human skin, and so forth, the distribution of holes according to shape and size is irregular, and the flow quantities are analogous to velocity, pressure, and so on. At the scale of the cavity, the irregularity is evident, and the investigation of the behavior of the flow and temperature fields at this scale is inherently complex.

The macroscopic method is as follows: In this method, the desired quantities of the flow field and temperature field are measured over an area containing a large number of holes. These quantities are then averaged over the volume, resulting in regular variations with time and space. These variations require theoretical analysis.

1. Statistical method: This methodology entails the aggregation of macroscopically identical holes and the subsequent averaging of resultant data. The principal challenge associated with this approach is that the statistical data pertaining to hole groups is typically derived from a single model, which is only feasible if statistical homogeneity is assumed.
2. Spatial method: In this method, macroscopic variables are defined as an appropriate mean value over a standard volume. This method is frequently employed in homogeneous porous media where the standard volume is periodically repeated. The fundamental principle of this method is the integration of variables into the standard volume.

The Darcy-Brinkman-Forchheimer equation is utilized to solve the flow in the developed mode:

$$\frac{\mu_{nf}}{\varepsilon} \nabla^2 u - \frac{\mu_{nf}}{K} u - \rho_{nf} F \frac{\varepsilon}{\sqrt{K}} u^2 \frac{dp}{dx} = 0 \qquad (1)$$

porosity rate ($\varepsilon = \frac{V_{nf}}{V_{tot}}$), where V_{nf} is the nanofluid volume and V_{tot} is the total volume. Eq. 1 F is the Forchimer coefficient and K is the permeability coefficient of the porous medium. μnf and ρnf viscosity and density of the nanofluid, respectively. The Bongiorno model for energy and volume fraction equations is used as follows. When the base fluid, nanoparticles and solid body are in temperature and thermal equilibrium, the

temperature distributions will be the same and an energy equation will be solved for them.

$$(\rho c)_m \frac{\partial T}{\partial t} + (\rho c)_m u.\nabla T = k_m \nabla^2 T + \varepsilon(\rho c)_p \left(D_B \nabla \varphi + \frac{D_T}{T_c} \nabla T.\nabla T \right) \quad (2)$$

$$\frac{1}{\sigma}\frac{\partial \varphi}{\partial t} + \frac{1}{\varepsilon}u.\nabla \varphi = D_B \nabla^2 \varphi + \frac{D_T}{T_c}\nabla^2 T \quad (3)$$

Eq 2-4 here ρ represents the density, c represents the specific heat capacity, u represents the speed, and φ represents the solution ratio. In this study, the Darcy-Brinkman-Forchheimer equation developed to study nanofluid flow in porous media is used. The central difference method was used to discretize the equation developed by Darcy-Brinkman-Forchheimer. The discrete form of the Darcy-Brinkman-Forchheimer equation in its extended form is as follows:

$$\frac{u^*(j+1)-2u^*(j)+(j-1)}{\Delta y^2} \frac{u^*(j)}{Da} \frac{\Delta}{\sqrt{Da}}(u^*(j))^2 \frac{1}{Da}\frac{dP^*}{dx^*}=0 \quad (4)$$

Here Da represents the Darcy factor and dP represents the pressure value. The Forchimer term in the Darcy-Brinkman-Forchimer equation is the nonlinear term of the above equation and the Newton method is used to solve this equation. In Newton's method, the derivative of the equation is calculated with respect to the velocity of the nodes at the initial velocity and the product of this matrix, which is a tridiagonal matrix, in the velocity matrix is equal to The velocity at the initial velocity of the Darcy-Brinkman-Furchimer equation, i.e. the velocity at the next step, is obtained from the product of the inverse matrix in the matrix of values and the steps continue until the final velocity is calculated (Epperson, 2021). Brownian motion and thermophoresis are located on the right hand side of equation (2-2).

In the work of Nield et al. (2003), the viscosity loss was expressed by the Brinkman number defined as μU2 / kΔTK, where k, ΔT and K are the order of the thermal conductivity coefficient, temperature difference and permeability of the porous medium. By comparing the order of magnitude, the other terms, including the viscosity loss, can be neglected, i.e., the temperature difference of the porous medium increases as the wall and nanofluid increase, while the viscosity loss This assumption is acceptable for heat transfer problems where heat flux or wall temperature is the dominant source of energy transfer. A uniform mesh is used for the computational domain and the construction of the mesh is done by an algebraic method. Figure 17 shows the grid of size 300x300 is considered for the computational domain and the equations are solved on this grid. The numerical solution flowchart is as follows:

The boundary conditions (for constant wall flux) are as follows(Eq 5-13):

$$y^*=0 \qquad \frac{\partial T^*}{\partial y^*}=-1, \quad \varphi^*=0, \ u^*=0 \quad (5)$$

$$y^*=2 \qquad \frac{\partial T^*}{\partial y^*}=1, \quad \varphi^*=0, u^*=0 \quad (6)$$

$$x^*=0 \qquad T^*=0, \quad \varphi^*=1 \quad (7)$$

For the outflow boundary condition, we consider the longitudinal slope to be zero, which is a very small value due to the length of the channel:

$$x^*=20 \qquad \frac{\partial T^*}{\partial x^*}=0 \ , \ \frac{\partial \varphi^*}{\partial x^*}=0 \quad (8)$$

The basic conditions are as follows:

$$T^*(t^*=0)=0, \ \varphi^*(t^*=0)=1 \quad (9)$$

For the boundary condition of constant temperature, a dimensionless temperature equal to one is placed on the walls.

For porous media in thermal instability, the boundary conditions of constant temperature and constant boundary flux are considered. The constant flux boundary condition and the flux contribution of each phase (fluid, nanoparticle and solid body) are introduced and discussed in the following chapters as part of the innovations and achievements in this thesis. The boundary conditions for the thermal instability case with constant wall temperature are as follows:

$$y^*=0 \quad and \quad 2 \quad T_f^*=1, T_p^*=1, \quad T_s^*=1 \varphi^*=0 \ , u^*= \ 0 \quad (10)$$

$$x^*=0 \quad T_f^*=1, T_p^*=1, T_s^*=1 \ , \ \varphi^*=1 \quad (11)$$

$$x^*=20 \ \frac{\partial T_f^*}{\partial x^*}=0 \ , \frac{\partial T_p^*}{\partial x^*}=0, \ \frac{\partial T_s^*}{\partial x^*}=0, \ \frac{\partial \varphi^*}{\partial x^*}=0 \quad (12)$$

The basic conditions are as follows:

$$T_f^*(t^*=0)=T_p^*(t^*=0)=T_s^*(t^*=0)=0$$

$$\varphi^*(t^*=0)=1 \quad (13)$$

It should be noted that the energy balance relation is included in each iteration of the numerical solution and hence the temperature gradient relation equal to zero can also be applied for constant flux.

Start

Solve (u^*) the Darcy Brinkman equation to obtain the

Use the obtained velocity and solve the liquid temperature equation to recover for T^*f

Solve the particle temperature equation to recover for T^*p

Solve the solid temperature equation to recover T^*s

Obtain new φ^*

$|T_f^{*n+1} - T_f^{*n}| < 10^{-15}$ & $|T_r^{*n+1} - T_r^{*n}| < 10^{-15}$

& $|T_p^{*n+1} - T_p^{*n}| < 10^{-15}$ & $|\varphi^{*n+1} - \varphi^{*n}| < 10^{-15}$

No

Yes

End
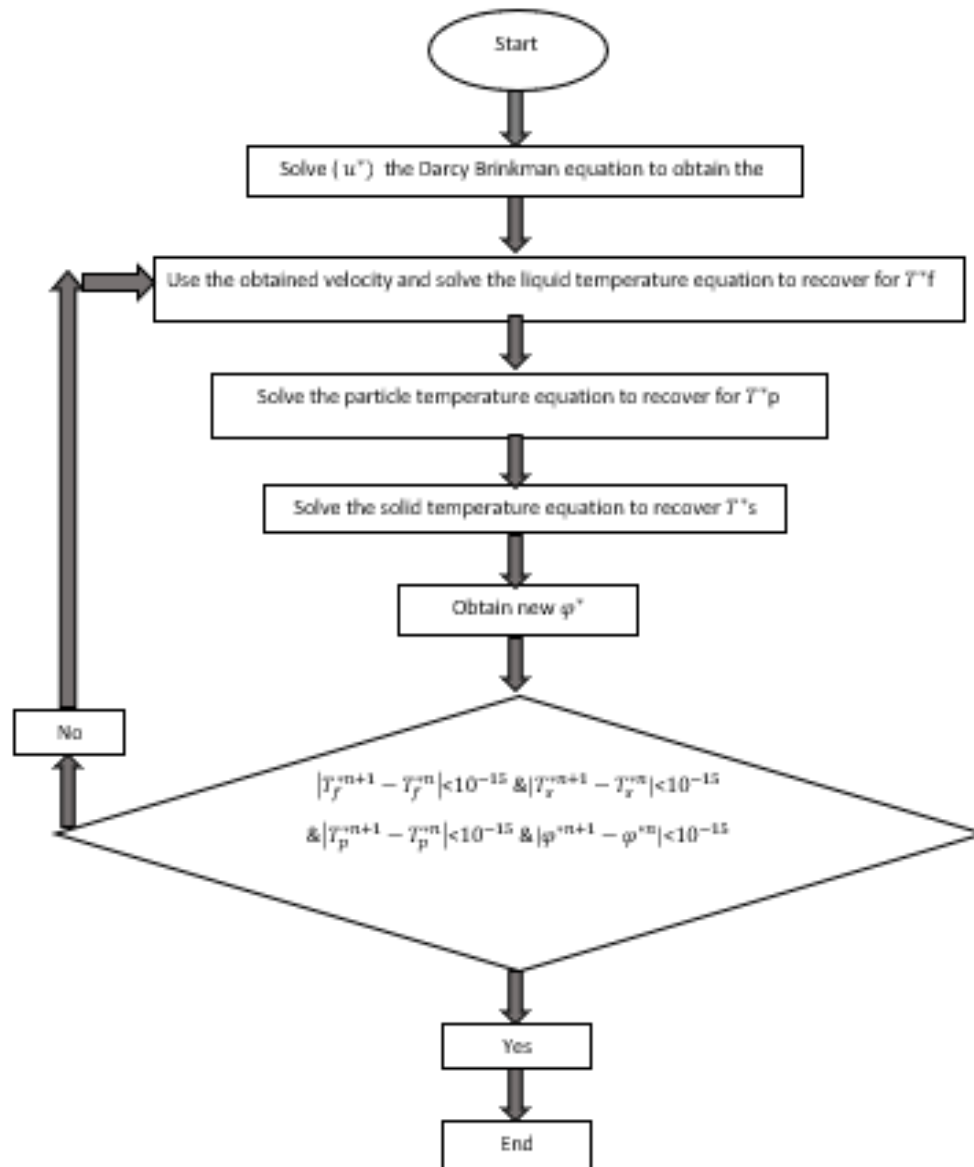
Figure 17.
Solution algorithm

Results and Discussion

In all analytical methods and most numerical methods, a constant porosity ratio and a homogeneous porous material are used to model fluid flow in a channel containing porous material. In other words, the porosity ratio is assumed to be constant in the equations. However, in experimental work it is difficult to create a homogeneous porous medium and it is difficult to keep the local porosity constant. Therefore, the fluid flow and heat transfer in the constructed (experimental) model are different from the equations and solved models. It is difficult to compare numerical models with experimental studies according to the situations briefly mentioned. Therefore, the validation was done with the help of classical equations with exact solutions.

The flow developed by Darcy Brinkman Forchheimer: Checking the accuracy of the numerical program written to solve the flow equation developed by Darcy Brinkman Forchheimer is as follows: Comparison with the analytical solution of the flow equation developed by Darcy Brinkman: The Darcy-Brinkman-Forchheimer equation in the limit state, i.e. at 0, is identical to the Darcy-Brinkman equation and its analytical solution, the second order ordinary differential equation.

Comparison with the analytical solution of the developed Darcy Brinkman Forchheimer flow equation: The channel up to the wall of the porous medium is considered.
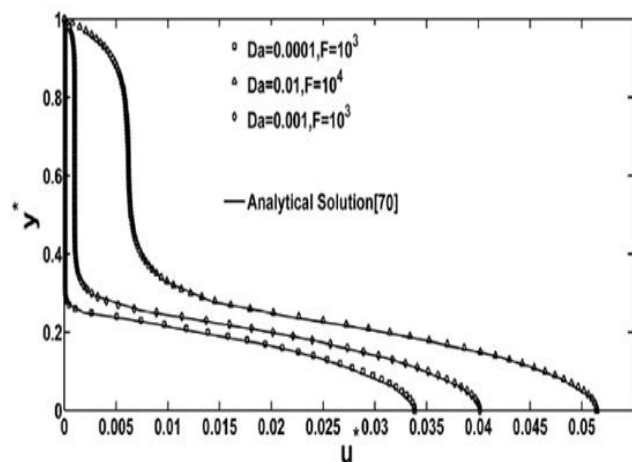
Figure 18.
Comparison of the numerical solution with Kuznetsov's analytical solution (Nield et al. 2003)

Figure 18 shows a very good agreement between the numerical and analytical results. The hot source temperature and the surrounding fluid temperature differences results in a change in the fluid density, which is a consequence of the influence of temperature-related buoyancy forces. Consequently, in accordance with the temperature differential, the fluid commences to flow over the solid surface. In such instances, naturally occurring heat transfer that takes place without any external stimulus is known as free or natural convective heat transfer. Given the importance of heat transfer, it is essential to take into account all factors and options in order to maximize the rate of heat transfer. The phenomenon of natural heat transfer is dependent on the random movements of molecules and the mass movement of the fluid. Consequently, it is advantageous to utilize compounds that exhibit a high thermal conductivity ratio in comparison to the fluid. In this context, the employment of fine particles with high thermal conductivity is a viable option. Subsequent studies have demonstrated that the reduction in particle size and dimensions has a significant impact on the heat transfer rate (Takabi & Shokouhmand, 2015; Babar & Ali, 2019; Said, 2022)s. In a semi-annular chamber with inclined pores, Motlagh et al. (2019) studied the free transport of a two-phase nanofluid. They applied the Darcy and Bongiorno models utilized Fe3O4 water as a magnetic nanofluid. They came to the conclusion that as the volume proportion of nanoparticles grows, so does the Nusselt number. Table 1 and Table 2 provides an overview of the features and findings of research articles on free convection heat transfer.

Conclusion

In this article, studies published between 1998 and 2024 on nanofluid heat transfer in porous media are reviewed. For this purpose, a general numerical evaluation of the published papers has been made. The results obtained from the Bongiorno model are also compared with the single-phase modeling of nanofluids and the results show that the migration of nanoparticles plays an important role in enhancing the heat transfer compared to the single-phase model. According to the findings, adding nanoparticles to the base fluid enhances temperature transfer. Nevertheless, the viscosity effect reduces thermal conductivity and obstructs heat transfer as nanoparticle volume concentration rises. Heat transfer increases with an increase in Darcy number and porosity coefficient and decreases with an increase in nanoscale conductivity when compared to a porous matrix. In this context, nanofluid heat transfer in porous media can be summarized as follows.

1. The relationship between porous matrix and nanoscale conductivity: As nanoscale conductivity increases, heat transfer within the porous matrix generally decreases. This is related to the fact that nanoscale structures, which conduct heat more efficiently due to better conductivity, reduce heat transfer by increasing thermal resistance.
2. Effect of Darcy number and porosity coefficient: When the Darcy number and porosity coefficient increase, heat transfer generally increases. The Darcy number is a measure of fluid motion in a porous medium through which a fluid passes, and when this magnitude increases, there is usually more flow and more efficient heat transfer. The porosity coefficient is a measure of the pore structure of a porous medium. Increasing the porosity coefficient usually results in more surface area and therefore more heat transfer.
3. The solid and porous medium height can be changed causes the flow regime in the room to change and has the effect of increasing or decreasing heat transfer.
4. Heat transfer is increased when the Rayleigh number rises.

These results explain the effects of factors such as nanoscale conductivity, Darcy number and porosity coefficient on heat transfer and show that heat transfer in general is determined by the interaction of these factors in a complex way. The main disadvantage of utilizing nanofluids in porous media is the increased pressure drop, which can be attributed to a number of factors. The movement of nanofluids through a porous medium can result in a greater pressure drop. In narrow passages between porous structures, nanofluids may encounter greater resistance, necessitating a higher pressure differential for flow. This can result in increased energy losses within the

system, which may subsequently lead to elevated processing costs. Secondly, concerns may be raised regarding the durability of nanofluids, especially when it comes to long-term uses. The tendency of nanosized particles to agglomerate or form precipitates can have a detrimental impact on the homogeneity and performance of the fluid. Such stability issues may restrict the utilization of nanofluids or necessitate the implementation of appropriate stabilization techniques. These shortcomings may restrict the utilization of nanofluids in porous media or impact their applicability. Nevertheless, the implementation of appropriately designed systems and effective stabilization techniques can facilitate the resolution of these issues.

Table 1.

Experimental results of the investigation of nanofluid displacement heat transfer

Author	Base Fluid	Nano Particle	Size of Nanoparticles (nm)	Volume Ratio in Percentageı	Geometry	Flow Regime and reynols number	Outcomes
Pak and Cho (1998)	Water	Al_2O_3 and TiO_2	13 27	3-1 3-1	Pipe	Turbulence 105-104	φ=0,1 Nusselt increases as Re increases
Wen and Ding (2004)	Water	Al_2O_3	56-25	1,6-0,6	Pipe	Laminar 2500-500	φ=0,1 heat transfer coefficient increased by 41%.
Heris et al. (2006)	Water	Al_2O_3CuO	20 60-50	3-2	Pipe	Laminar 2010-650	Heat transfer coefficient increased with increasing φ
Lai et al. (2006)	Water	Al_2O_3	20	1-0	Pipe	Laminar 270	The Nusselt number increased by 8% for every 1% φ.
Jung et al. (2006)	Water	Al_2O_3	10	1,8-0,5	Micro channel	Laminar 300-5	The Nusselt number increased by 32% for φ 1.8%.
Rea et al. (2008)	Water	ZrO2	46 60	3,6-0,9 0,9-0,2	Pipe	Turbulence 63000-9000	Slightly increased heat transfer
Zhou (2004)	Acetone	Cu	100-80	4	Pipe	-	Increase in heat transfer coefficient with increase in Cu
Li et al. (2005)	Water	Cu	26	2-0,5	Pipe	Turbulence Laminar	The Nusselt number ratio of the nanofluid to the base fluid varies between 1.6-1.39.
Faulkner et al. (2004)	Water	CNT	100	4,4-1,1	-	Laminar	Increasing the heat transfer coefficient by increasing the concentration of nanofluids.
Yang et al. (2005)	Oil	MWCNT	100	1-0,1	Pipe	Laminar	35% increase in heat transfer

Table 2.

Overview of some other studies

Author	Theoretical review	Modeling method	Outcomes
Xuan and Roetzel (2000)	Heat transfer coefficient in copper with oil and water	Single phase	Increasing the heat transfer coefficient by reducing the particle size.
Buongiorno (2006)	Displacement of nanofluids	Two-phase model with non-uniform phase for the particle	Brownian effects and thermophoresis are the dominant effects.
Behzadmehr et al. (2007)	Forced convection heat transfer in turbulent regime	Dual phase	Increasing the displacement heat transfer coefficient with increasing φ and Re
Maïga et al. (2004)	Forced heat transfer in a tube containing aluminum and ethylene glycol in water	Single phase	60% increase in heat transfer
Mansour et al. (2007)	Thermal and hydraulic behavior in laminar and turbulent flow in a pipe with constant flux	Single phase	Heat transfer coefficient increase in both regimes

References

Abbassi, H., & Aghanajafi, C. (2006). Evaluation of heat transfer augmentation in a nanofluid-cooled microchannel heat sink. *Journal of Fusion Energy, 25, 187–196.*

Babar, H., & Ali, H. M. (2019). Towards hybrid nanofluids: Preparation, thermophysical properties, applications, and challenges. *Journal of Molecular Liquids, 281, 598–633.*

Behzadmehr, A., Saffar-Avval, M., & Galanis, N. (2007). Prediction of turbulent forced convection of a nanofluid in a tube with uniform heat flux using a two phase approach. *International Journal of Heat and Fluid Flow, 28(2), 211–219.*

Boccardo, G. (2020). A review of transport of nanoparticles in porous media: From pore-to macroscale using computational methods. *Nanomaterials for the Detection and Removal of Wastewater Pollutants, 351–381.*

Buongiorno, J. (2006). Convective heat transfer enhancement in nanofluids. In Paper US11, 18th National & 7th ISHMT-ASME Heat and Mass Transfer Conference.

Choi, S. (2002). Two metals are better than one. Argonne National Laboratory.https://www.anl.gov/article/two-metals-are-better-than-one

Das, S. K., Putra, N., Thiesen, P., & Roetzel, W. (2003). Temperature dependence of thermal conductivity enhancement for nanofluids. *J. Heat Transfer, 125(4), 567–574.*

Ding, Y., Alias, H., Wen, D., & Williams, R. A. (2006). Heat transfer of aqueous suspensions of carbon nanotubes (CNT nanofluids. *International Journal of Heat and Mass Transfer, 49(1–2), 240–250.*

Duangthongsuk, W., & Wongwises, S. (2008). Effect of thermophysical properties models on the predicting of the convective heat transfer coefficient for low concentration nanofluid. *International Communications in Heat and Mass Transfer, 35(10), 1320–1326.*

Duangthongsuk, W., & Wongwises, S. (2009). Heat transfer enhancement and pressure drop characteristics of TiO2–water nanofluid in a double-tube counter flow heat exchanger. *International Journal of Heat and Mass Transfer, 52(7–8), 2059–2067.*

Eastman, J. (1999). Novel thermal properties of nanostructured materials. Argonne National Lab, IL(US).

Eastman, J. A., Choi, S., Li, S., Yu, W., & Thompson, L. (2001). Anomalously increased effective thermal conductivities of ethylene glycol-based nanofluids containing copper nanoparticles. *Applied Physics Letters, 78(6), 718–720.*

Epperson, J. F. (2021). An introduction to numerical methods and analysis. John Wiley & Sons.

Faulkner, D. J., Rector, D. R., Davidson, J. J., & Shekarriz, R. (2004). Enhanced heat transfer through the use of nanofluids in forced convection. In ASME International Mechanical Engineering Congress and Exposition (pp. 219–224).

Ghazvini, M., Akhavan-Behabadi, M., & Esmaeili, M. (2009). The effect of viscous dissipation on laminar nanofluid flow in a microchannel heat sink. Proceedings of the Institution of Mechanical Engineers, Part C: *Journal of Mechanical Engineering Science, 223(11), 2697–2706.*

Ghazvini, M., & Shokouhmand, H. (2009). Investigation of a nanofluid-cooled microchannel heat sink using Fin and porous media approaches. *Energy Conversion and Management, 50(9), 2373–2380.*

Gundogdu, S. (2023). Micro and nano plastics in groundwater systems: A review of current knowledge and future perspectives. TrAC Trends in Analytical Chemistry, 117119.

Heris, S. Z., Esfahany, M. N., & Etemad, S. G. (2007). Experimental investigation of convective heat transfer of Al_2O_3/water nanofluid in circular tube. *International Journal of Heat and Fluid Flow, 28(2), 203–210.*

Heris, S. Z., Etemad, S. G., & Esfahany, M. N. (2006). Experimental investigation of oxide nanofluids laminar flow convective heat transfer. *International Communications in Heat and Mass Transfer, 33(4), 529–535.*

Heyhat, M., & Kowsary, F. (2010). Effect of particle migration on flow and convective heat transfer of nanofluids flowing through a circular pipe.

Jang, S. P., & Choi, S. U. (2004). Role of Brownian motion in the enhanced thermal conductivity of nanofluids. *Applied Physics Letters, 84(21), 4316–4318.*

Jung, J.-Y., Oh, H.-S., & Kwak, H.-Y. (2006). Forced convective heat transfer of nanofluids in microchannels. In ASME International Mechanical Engineering Congress and Exposition (pp. 327–332).

Kasaeian, A. (2017). Nanofluid flow and heat transfer in porous media: A review of the latest developments. *International Journal of Heat and Mass Transfer, 107, 778–791.*

Keblinski, P., Eastman, J. A., & Cahill, D. G. (2005). Nanofluids for thermal transport. *Materials Today, 8(6), 36–44.*

Khanafer, K., Vafai, K., & Lightstone, M. (2003). Buoyancy-driven heat transfer enhancement in a two-dimensional enclosure utilizing nanofluids. International Journal of Heat and Mass Transfer, 46(19), 3639–3653.

Kim, J., Kang, Y. T., & Choi, C. K. (2007). Soret and Dufour effects on convective instabilities in binary nanofluids for absorption application. International Journal of Refrigeration, 30(2), 323–328.

Kim, S. Y., Koo, J.-M., & Kuznetsov, A. V. (2001). Effect of anisotropy in permeability and effective thermal conductivity on thermal performance of an aluminum foam heat sink. Numerical Heat Transfer: Part a: Applications, 40(1), 21–36.

Kim, S. Y., & Kuznetsov, A. V. (2003). Optimization of pin-fin heat sinks using anisotropic local thermal nonequilibrium porous model in a jet impinging channel. Numerical Heat Transfer: Part a: Applications, 44(8), 771–787.

Kuznetsov, A., & Nield, D. (2010a). Effect of local thermal non-equilibrium on the onset of convection in a porous medium layer saturated by a nanofluid. Transport in Porous Media, 83, 425–436.

Kuznetsov, A., & Nield, D. (2010b). The onset of double-diffusive nanofluid convection in a layer of a saturated porous medium. Transport in Porous Media, 85, 941–951.

Kuznetsov, A., & Nield, D. (2010c). Thermal instability in a porous medium layer saturated by a nanofluid: Brinkman model. Transport in Porous Media, 81, 409–422.

Kuznetsov, A. V., & Nield, D. A. (2011). The effect of local thermalnonequilibrium on the onset of convection in a porous medium layer saturated by a nanofluid: Brinkman model. Journal of Porous Media, 14(4).

Lai, W., Duculescu, B., Phelan, P., & Prasher, R. (2006). Convective heat transfer with nanofluids in a single 1.02-mm tube. In ASME International Mechanical Engineering Congress and Exposition (pp. 337–342).

Li, Q., & Xuan, Y.-M. (2004). Flow and Heant Transfer Performances of Nanofluids Inside Small Hydraulic Diameter Flat Tube. Journal of Engineering Thermophysics, 25(2), 305–307.

Li, Q., Xuan, Y., & Jiang, J. (2005). Experimental investigation on flow and convective heat transfer feature of a nanofluid for aerospace thermal management.

Ling, X., Yan, Z., Liu, Y., & Lu, G. (2021). Transport of nanoparticles in porous media and its effects on the co-existing pollutants. Environmental Pollution, 283, 117098.

Mahdi, R. A., Mohammed, H., Munisamy, K., & Saeid, N. (2015). Review of convection heat transfer and fluid flow in porous media with nanofluid. Renewable and Sustainable Energy Reviews, 41, 715–734.

Maïga, S., Nguyen, C. T., Galanis, N., & Roy, G. (2004). Heat transfer behaviours of nanofluids in a uniformly heated tube. Superlattices and Microstructures, 35(3–6), 543–557.

Mansour, R. B., Galanis, N., & Nguyen, C. T. (2007). Effect of uncertainties in physical properties on forced convection heat transfer with nanofluids. Applied Thermal Engineering, 27(1), 240–249.

Masuda, H., Ebata, A., Teramae, K., & Hishinuma, N. (1993). Alteration of Thermal Conductivity and Viscosity of Liquid by Dispersing Ultra-Fine Particles. Dispersion of Al_2O_3, SiO2 and TiO_2 Ultra-Fine Particles. Netsu Bussei, 7(4), 227–233.

Meng, X., & Yang, D. (2019). Critical review of stabilized nanoparticle transport in porous media. Journal of Energy Resources Technology, 141(7), 70801.

Motlagh, S. Y., Golab, E., & Sadr, A. N. (2019). Two-phase modeling of the free convection of nanofluid inside the inclined porous semi-annulus enclosure. International Journal of Mechanical Sciences, 164, 105183.

Murshed, S., Leong, K., & Yang, C. (2008). Thermophysical and electrokinetic properties of nanofluids–a critical review. Applied Thermal Engineering, 28(17–18), 2109–2125.

Mustafaoğlu, M. (2023). Numerical Analysis of Heat Transfer of Polyethylene Nanocomposites with Carbon Nanotubes. NanoEra, 3(2), 28–33.

Nield, D., & Kuznetsov, A. V. (2009). Thermal instability in a porous medium layer saturated by a nanofluid. International Journal of Heat and Mass Transfer, 52(25–26), 5796–5801.

Nield, D., & Kuznetsov, A. (2014). Forced convection in a parallel-plate channel occupied by a nanofluid or a porous medium saturated by a nanofluid. International Journal of Heat and Mass Transfer, 70, 430–433.

Nield, D., Kuznetsov, A., & Xiong, M. (2003). Thermally developing forced convection in a porous medium: Parallel plate channel with walls at uniform temperature, with axial conduction and viscous dissipation effects. International Journal of Heat and Mass Transfer, 46(4), 643–651.

Pak, B. C., & Cho, Y. I. (1998). Hydrodynamic and heat transfer study of dispersed fluids with submicron metallic oxide particles. Experimental Heat Transfer an International Journal, 11(2), 151–170.

Prakash, M., & Giannelis, E. (2007). Mechanism of heat transport in nanofluids. Journal of computer-aided materials design, 14, 109–117.

Putra, N., Roetzel, W., & Das, S. K. (2003). Natural convection of nano-fluids. Heat and Mass Transfer, 39(8), 775–784.

Rashad, A., Chamkha, A. J., & Abdou, M. (2013). Mixed convection flow of non-Newtonian fluid from vertical surface saturated in a porous medium filled with a nanofluid.

Rea, U., McKrell, T., Hu, L.-W., & Buongiorno, J. (2008). Experimental study of laminar convective heat transfer and viscous pressure loss of alumina-water nanofluid. In International Conference on Micro/Nanoscale Heat Transfer.

Rosca, A., Rosca, N., Grosan, T., & Pop, I. (2012). Non-Darcy mixed convection from a horizontal plate embedded in a

nanofluid saturated porous media. *International Communications in Heat and Mass Transfer, 39(8), 1080–1085.*

Roy, G., Nguyen, C. T., & Lajoie, P.-R. (2004). Numerical investigation of laminar flow and heat transfer in a radial flow cooling system with the use of nanofluids. *Superlattices and Microstructures, 35(3–6), 497–511.*

Said, Z. (2022). Recent advances on the fundamental physical phenomena behind stability, dynamic motion, thermophysical properties, heat transport, applications, and challenges of nanofluids. *Physics Reports, 946, 1–94.*

Salloum, M., Ma, R., Weeks, D., & Zhu, L. (2008). Controlling nanoparticle delivery in magnetic nanoparticle hyperthermia for cancer treatment: Experimental study in agarose gel. International Journal of Hyperthermia, 24(4), 337–345.

Salloum, M., Ma, R., & Zhu, L. (2009). Enhancement in treatment planning for magnetic nanoparticle hyperthermia: Optimization of the heat absorption pattern. *International Journal of Hyperthermia, 25(4), 309–321.*

Sheikholeslami, M., & Ganji, D. (2016). Nanofluid convective heat transfer using semi analytical and numerical approaches: A review. *Journal of the Taiwan Institute of Chemical Engineers, 65, 43–77.*

Sheikholeslami, M., & Rokni, H. B. (2017). Simulation of nanofluid heat transfer in presence of magnetic field: A review. *International Journal of Heat and Mass Transfer, 115, 1203–1233.*

Sun, Q., & Pop, I. (2011). Free convection in a triangle cavity filled with a porous medium saturated with nanofluids with flush mounted heater on the wall. *International Journal of Thermal Sciences, 50(11), 2141–2153.*

Takabi, B., & Shokouhmand, H. (2015). Effects of Al 2 O 3–Cu/water hybrid nanofluid on heat transfer and flow characteristics in turbulent regime. *International Journal of Modern Physics C, 26(04), 1550047.*

Tham, L., & Nazar, R. (2012). Mixed convection flow about a solid sphere embedded in a porous medium filled with a nanofluid.

Tsai, T.-H., & Chein, R. (2007). Performance analysis of nanofluid-cooled microchannel heat sinks. *International Journal of Heat and Fluid Flow, 28(5), 1013–1026.*

Wang, B.-X., Zhou, L.-P., & Peng, X.-F. (2003). A fractal model for predicting the effective thermal conductivity of liquid with suspension of nanoparticles. *International Journal of Heat and Mass Transfer, 46(14), 2665–2672.*

Wang, X., Xu, X., & Choi, S. U. (1999). Thermal conductivity of nanoparticle-fluid mixture. *Journal of Thermophysics and Heat Transfer, 13(4), 474–480.*

Wen, D., & Ding, Y. (2004). Experimental investigation into convective heat transfer of nanofluids at the entrance region under laminar flow conditions. *International Journal of Heat and Mass Transfer, 47(24), 5181–5188.*

Whitaker, S. (1986). Flow in porous media I: A theoretical derivation of Darcy's law. *Transport in Porous Media, 1, 3–25.*

Xu, H. J., Xing, Z. B., Wang, F., & Cheng, Z. (2019). Review on heat conduction, heat convection, thermal radiation and phase change heat transfer of nanofluids in porous media: Fundamentals and applications. *Chemical Engineering Science, 195, 462–483.*

Xuan, Y., & Li, Q. (2003). Investigation on convective heat transfer and flow features of nanofluids. *J. Heat Transfer, 125(1), 151–155.*

Xuan, Y., & Roetzel, W. (2000). Conceptions for heat transfer correlation of nanofluids. *International Journal of Heat and Mass Transfer, 43(19), 3701–3707.*

Yang, Y., Zhang, Z. G., Grulke, E. A., Anderson, W. B., & Wu, G. (2005). Heat transfer properties of nanoparticle-in-fluid dispersions (nanofluids) in laminar flow. *International Journal of Heat and Mass Transfer, 48(6), 1107–1116.*

Yu, W., France, D. M., Routbort, J. L., & Choi, S. U. (2008). Review and comparison of nanofluid thermal conductivity and heat transfer enhancements. *Heat Transfer Engineering, 29(5), 432–460.*

Zhang, M., Hou, J., Xia, J., Wu, J., You, G., & Miao, L. (2024). Statuses, shortcomings, and outlooks in studying the fate of nanoplastics and engineered nanoparticles in porous media respectively and borrowable sections from engineered nanoparticles for nanoplastics. *Science of the Total Environment*, 169638.

Zhou, D. (2004). Heat transfer enhancement of copper nanofluid with acoustic cavitation. *International Journal of Heat and Mass Transfer, 47(14–16), 3109–3117.*